

國立中央大學

大氣科學系
碩士論文

統計分析 2008 年西南氣流實驗期間對流系統的
雙偏極化雷達拉格朗日特徵

Statistical Analysis of Dual-Polarization Parameter
Lagrangian Features of Convective Storms During
SoWMEX / TiMREX

研究生：葉玉婕

指導教授：張偉裕 教授

中華民國一零九年六月

國立中央大學圖書館學位論文授權書

填單日期：110 / 07 / 13

授權人姓名	葉玉婕	學號	108621019
系所名稱	大氣物理所	學位類別	<input checked="" type="checkbox"/> 碩士 <input type="checkbox"/> 博士
論文名稱	Statistical Analysis of Dual-Polarization Parameter Lagrangian Features of Convective Storms During SoWMEX / TiMREX	指導教授	張偉裕

學位論文網路公開授權
<p>授權本人撰寫之學位論文全文電子檔：</p> <ul style="list-style-type: none"> • 在「國立中央大學圖書館博碩士論文系統」 <ul style="list-style-type: none"> (V) 同意立即網路公開 () 同意 於西元_____年_____月_____日網路公開 () 不同意網路公開，原因是：_____ • 在國家圖書館「臺灣博碩士論文知識加值系統」 <ul style="list-style-type: none"> (V) 同意立即網路公開 () 同意 於西元_____年_____月_____日網路公開 () 不同意網路公開，原因是：_____ <p>依著作權法規定，非專屬、無償授權國立中央大學、台灣聯合大學系統與國家圖書館，不限地域、時間與次數，以文件、錄影帶、錄音帶、光碟、微縮、數位化或其他方式將上列授權標的基於非營利目的進行重製。</p>

學位論文紙本延後公開申請 (紙本學位論文立即公開者此欄免填)
<p>本人撰寫之學位論文紙本因以下原因將延後公開</p> <ul style="list-style-type: none"> • 延後原因 <ul style="list-style-type: none"> () 已申請專利並檢附證明，專利申請案號：_____ () 準備以上列論文投稿期刊 () 涉國家機密 () 依法不得提供，請說明：_____ • 公開日期：西元_____年_____月_____日 <p>※繳交教務處註冊組之紙本論文(送繳國家圖書館)若不立即公開，請加填「國家圖書館學位論文延後公開申請書」</p>

研究生簽名： 葉玉婕

指導教授簽名： 張偉裕

國立中央大學碩士班研究生
論文指導教授推薦書

大氣科學學系大氣物理碩士班學系/研究所 葉玉婕 研究生
所提之論文 Statistical Analysis of Dual-Polarization Parameter
Lagrangian Features of Convective Storms During SoWMEX /
TIMREX
係由本人指導撰述，同意提付審查。

指導教授 張偉銘 (簽章)

110 年 7 月 13 日

1100713

國立中央大學碩士班研究生
論文口試委員審定書

大氣科學學系大氣物理碩士班 學系/研究所 葉玉婕 研究生
所提之論文 Statistical Analysis of Dual-Polarization Parameter
Lagrangian Features of Convective Storms During SoWMEX /
TiMREX

經由委員會審議，認定符合碩士資格標準。

學位考試委員會召集人

黃 楷 吉

委

員

中 華 民 國 110 年 7 月 27 日

1100713

國立中央大學碩士班研究生
論文口試委員審定書

大氣科學學系大氣物理碩士班 學系/研究所 葉玉婕 研究生
所提之論文 Statistical Analysis of Dual-Polarization Parameter
Lagrangian Features of Convective Storms During SoWMEX /
TIMREX

經由委員會審議，認定符合碩士資格標準。

學位考試委員會召集人 _____

委 員 _____

張保亮

中 華 民 國 110 年 9 月 27 日

國立中央大學碩士班研究生
論文口試委員審定書

大氣科學學系大氣物理碩士班 學系/研究所 葉玉婕 研究生
所提之論文 Statistical Analysis of Dual-Polarization Parameter
Lagrangian Features of Convective Storms During SoWMEX /
TIMREX

經由委員會審議，認定符合碩士資格標準。

學位考試委員會召集人 _____

委 員 _____

廖宇慶

鍾高陞

張蔚銘

中 華 民 國 110 年 7 月 27 日

1100713

摘要

西南氣流伴隨梅雨鋒面不僅能為台灣帶來豐沛的降水量，過多的雨水也會帶來致災的風險。本篇研究希望透過了解對流在結構上的變化、動力場的特徵及微物理過程的演化，診斷出對流胞當時的發展特徵，進一步分析這些過程隨時間上的表現。而要做到上述事情，必須仰賴對流胞辨識與追蹤技術，「SMART」(Storm Motion Analysis by Radar Tracking) 就此誕生。本篇研究收集了 2008 年西南氣流聯合觀測實驗中，NCAR SPOL 所提供的雷達雙偏參數資料，透過給定回波門檻與面積門檻來進行對流胞的辨識。研究中利用兩個不同的回波門檻，針對相同的降水事件，定義出兩種對流胞範圍。低回波門檻辨識出的對流胞稱為「parent-cell」，用以選取整個系統的降水範圍；高回波門檻辨識出的對流胞稱為「child-cell」，用來找出對流胞的核心區域。針對兩種辨識結果，皆能計算出如下的對流胞特徵：幾何中心(X, Y)、回波權重中心(X_z, Y_z)、面積(A)、長軸與短軸(r_1 與 r_2)、方向性(θ)以及該對流胞範圍內的雙偏參數(DPM)。因此，隨著對流胞的移動，這些特性將得到進一步的檢驗。

本研究透過 38 個個案統計與 5 個個案分析的結果，定量上的探討雙偏參數在水平及垂直上的分離現象與特徵。其結果指出，當對流胞發展至成熟階段，雙偏參數在水平方向會有顯著的 Z_{DR} 與 K_{DP} 分離現象。而從垂直分離趨勢可知，當對流胞從發展至成熟階段，雙偏參數會出現正轉負的分離趨勢；反之，當對流胞從成熟至消散階段，則會出現負轉正的分離趨勢。透過趨勢上的轉換，更能幫助我們了解其雙偏參數隨對流胞發展至不同階段的特徵。本研究分析結果顯示了利用雙偏極化參數診斷對流胞發展的潛力。

Abstract

The mesoscale convective systems (MCSs) associated with East Asia summer south-westerly monsoon and Mei-Yu front play essential role in contributing heavy precipitation in Taiwan. A storm identification and tracking technique (SMART: Storm Motion Analysis by Radar Tracking) using radar data was applied to investigate various characteristics of structural evolutions, dynamic, microphysics processes of these precipitation systems. The NCAR SPOL data during SoWMEX/TiMREX was analyzed to derived the storm characteristics. Storms were identified by considering two reflectivity threshold values. Lower reflectivity threshold value reveals entire precipitation system. On the other hand, the higher reflectivity threshold value locates the core of the convective system. The dual-reflectivity threshold technique distinguishes ‘child-cell’ (convective core zone) from ‘parent-cell’ (complete precipitation area). After identifying child-cell and parent-cell, the storm properties including geometric centroid (X, Y), reflectivity-weighted centroid (Xz, Yz), size (A), major and minor axes ($r1$ and $r2$), orientation of the major axes relative to the x axis (θ) and dual-polarimetric parameters within the storm area are analyzed. In addition, microphysical characteristics of convective system are investigated by the vertical slop and horizontal separation distance of various dual-polarimetric measurements (DPMs). These properties thus are examined with the evolution of the storm track.

There are 38 cases selected for statistical analysis and 5 cases selected for detailed case study. Both horizontal and vertical microphysics characteristics are analyzed quantitatively. The tendency of vertical slope of dual-polarimetric parameters vary from positive to negative values during the developing stage of the storm. Subsequently, the tendency varies from negative to positive during dissipating stage. The analysis has shown the potential of diagnosing the storm development by utilizing dual-polarimetric parameters. Furthermore, pronounced horizontal

separation distance between Z_{DR} and K_{DP} centers can be noticed during mature state of the storm. As the result shows, the separation distance has high correlation to the mid-level wind condition (6 km).

Acknowledgment

回首碩班生活，既充實又快樂。當初憑藉著一股衝動進入了雷達實驗室；靠著一句「Fake it until you become it.」撐過了無數次的低潮。還記得大學剛畢業，程式能力遠不如人，面對眼前一行的程式語言，有如閱讀天書一般，久久未能消化。即便如此，我現在的指導教授 張偉裕老師 依然願意收我為指導學生，一路鼓勵著我、引導我，從觀念上的釐清至實際上的操作、從研究工具的學習至改良、論文題目的方向至訂定，乃至研究技巧的傳承與指導，一步步引領著我完成碩班學業。藉此我謹向偉裕老師致以深深地謝意。這六年來，我從老師身上學到的不只是學者對研究的執著、老師對教書的熱忱，更是指導教授對於學生的關心、愛護與諄諄教導。

感謝實驗室所有老師 陳台琪老師 廖宇慶老師 鍾高陞老師，對於我的研究提出了寶貴的建議與提問，幫助我從不同的角度思考與解決問題，也學習了如何在理解他人問題後，表達清楚並且釐清他人疑惑。雖然受到疫情影響，出觀測的次數屈指可數，卻可以從每次的實驗中感受到老師們嚴謹的態度與對學生們的照顧，既專業又溫暖。感謝口試委員 黃椿喜博士 及 張保亮博士 在口試時給我寶貴的建議及鼓勵，幫助我將此份論文寫得更加完整。

謝謝實驗室學長姊平時的幫忙與照顧。謝謝信廷學長對雷達們的照顧。謝謝小那與凱蒂分擔了所有行政公務。謝謝 Haidy、Nghì、大柯、晨語、小那、凱蒂、玉霜、可昕、羽廷 學姊們，除了在我研究遇到困難時幫助我，大方地分享妳們的經歷外，時不時地噓寒問暖、笑臉迎人，讓原本死氣沉沉的研究氛圍頓時充滿色彩，有妳們在的地方格外放鬆。謝謝許修維、吳冠伯、楊柏謙、鄧詠霖、游承融、陳立昕、陳鈞澤、鄒益豪、邱顯榮、蔡博安 學長們，除了在專業知識上的請教、實驗室需要壯丁時義不容辭的幫忙外，更是在出觀測時擔任司機的角色，讓我們能夠放心出門、平安歸來。

謝謝一路陪伴我度過兩年碩班生活的實驗室同儕們。秉學、子睿、采蓉、詠筌、佩安。這兩年來我們一起出差、一起觀測、一起助教、一起修課、一起吃飯、一起熬夜。雖然過程很辛苦，但在你們的陪伴與幫助下，解決了迎面而來的所有問題。在求學的最後生涯裡，很幸運的能夠認識你們。謝謝宴伶與旻恩，雖然我們隸屬於不同實驗室，卻是生活中的好夥伴。透過逛街與運動抒發內心的壓力、透過回宿舍路上的小聊鼓勵彼此，感謝你們一路的陪伴。謝謝所有無論在課堂或課後給予我幫助的學長姐、同儕及學弟妹。

感謝家人朋友一路上的支持與鼓勵。從大學到碩班，父母不僅未曾質疑我所選擇的科系，還很願意放手讓我嘗試新的事物，讓我無後顧之憂的出去闖蕩。感謝朋友們在我無聊壓力大時，聽我抱怨陪我聊天，陪我度過許多的低潮期。即使你們不在我身邊，卻能從電話這端感受到你們的陪伴，備感溫暖。你們的鼓勵是我成長的動力，我會帶著大家的期望，面對未來的挑戰。

在此，我再次為所有幫助過我的師長、家人及朋友，表達由衷的感謝。

葉玉婕 謹致

中央大學大氣物理研究所

中華民國一百一十年七月

Outline

摘要	vii
Abstract.....	viii
Acknowledgment.....	x
Outline	xii
List of Table.....	xiv
List of Figures.....	xv
Chapter 1 Introduction.....	1
1.1 Motivation	1
1.2 Literature Review	2
1.3 Research Purposes	6
1.4 Paper Structure	6
Chapter 2 Data and Methodology.....	7
2.1 International Field Campaign	7
2.2 Reanalysis dataset.....	8
2.3 Storm Identification and Tracking System	8
2.3.1 Radar Data Processing	9
2.3.2 2-Dimensional and 3-Dimensional Storm Identification	10
2.3.3 Storm Properties	12
2.3.4 2-Dimensional Moment Invariants.....	13

2.3.5	2-Dimensional Storm Tracking Methodology.....	15
2.4	Dual-Polarimetric Parameters	17
Chapter 3 Results and Discussions		21
3.1	Overview of SoWMEX SPOL Observations	21
3.2	Case analysis	22
3.2.1	Statistical Characteristics of 38 Cases.....	24
3.2.2	Horizontal Separation Discussion – 5 Cases.....	31
3.2.2.1	Weak Case 1 (case number 22).....	33
3.2.2.2	Weak Case 2 (case number 20).....	34
3.2.2.3	Moderate Case (case number 34)	35
3.2.2.4	Strong Case 1 (case number 29).....	36
3.2.2.5	Strong Case 2 (case number 30).....	38
3.3	Statistical Performance of Motion Vectors	39
Chapter 4 Conclusions and Future Works		41
4.1	Conclusions	41
4.2	Future Works	43
References		44
Tables.....		48
Figures		51
Appendix		90

List of Table

Table 1.1	List of 47 cases.....	48
Table 3.1	Integration table of storm motions of 5 cases.	50

List of Figures

Figure 1. 1 The time-height properties of cell 590 are shown here. **Figure 1. 1** a-h show the time-height evolution of Z , ZDR , KDP , ρ_{hv} , Dm , NW , LMA_CC and $DHCA$. For **Figure 1. 1** a-f, each grid box represents the magnitude of the variables at the same location of maximum Z of each time-height dimension for this cell. **Figure 1. 1** g shows the integrated VHF lightning sources for this cell at each time-height dimension. **Figure 1. 1** h shows hydrometeor classifications. Each panel title includes the specific UTC time of the cell shown in the figure when the cell is first detected. For instance, 201,606,111,854 means 18:54, June 11, 2016 and 093 km/181° 32.82°N -101.83°W means this cell is first detected 93 km away from the KLBB radar with an azimuth angle of 181° located at 32.82°N -101.83°W.(Adopted from Hu et al. 2019)51

Figure 2. 1 Location of NCAR S-POL radar. The distance between concentric circle is 50-kilometers. 52

Figure 2. 2 A schematic flow diagram of SMART. (a) A side view of radar volume scan. (b) Sketch map of data interpolated into Cartesian coordinate in different level. (c) Composite maximum reflectivity from CAPPIs into MOSAIC. (d) Simplified diagram of storm identification..... 52

Figure 2. 3 A sensitivity test of both reflectivity thresholds and area thresholds in May 21th, 2014 from CWB QPESUMES data. Color shaded represent each storm area. ‘x’ is the reflectivity weighted centroid of each storm. 53

Figure 2. 4 Schematic diagram of cell number and area in different reflectivity threshold. Color shaded represent different reflectivity area. 54

Figure 2. 5 Based on Dixon and Wiener (1993) . A schematic diagram of 2-Dimensional storm identify with dual-reflectivity threshold is shown. Colored grids are the successful identification area. Numbers in colored grids represent the area identified by different reflectivity thresholds. ‘1’ for 30 dBZ and ‘2’ for 35 dBZ. 54

Figure 3. 1	Time chart of IOPs and the corresponding weather conditions during SoWMEX.	55
Figure 3. 2	Daily cell number during SoWMEX in different storm types. (a) parent-cell (b) child-cell (c) cell-embed.....	56
Figure 3. 3	Daily multiple cell distribution, numbers in log10 scale.	57
Figure 3. 4	Parent-cell area relative to cell max reflectivity.....	58
Figure 3. 5	Parent-cell area relative to child-cell number embed.	58
Figure 3. 6	Distribution of daily storm track life time.....	59
Figure 3. 7	Storm maximum area relative to storm life time.....	59
Figure 3. 8	2008 SoWMEX daily storm track distributions. (a) Daily number of storm track with 30 dBZ reflectivity threshold. (b) Daily number of storm track with 30 dBZ reflectivity threshold and duration threshold. (c) Daily number of storm track with 30 dBZ reflectivity threshold, duration threshold and area threshold.....	60
Figure 3. 9	Storm track path of 47 cases. Numbers by the storm path are the case number. Detail descriptions of each storm are mention in Table 1. 1	61
Figure 3. 10	Vertical section from the reflectivity weighted center along the x direction of case 30. From (a) to (k) are the different time period of the storm track.	62
Figure 3. 11	Time series of mean dual-polarimetric parameters with height. An example of developing storm. (a) <i>ZHH</i> (b) <i>ZDP</i> (c) <i>ZDR</i> (d) <i>KDP</i> , shading is the mean value respectively. Height below the black dots represent the blind zone below the lowest elevation and height above the blue dots represents the blind zone above the maximum elevation at each time step. Accumulative values are shown as the pink lines, pink squares are the maximum accumulative time; The calculated vertical slope are shown as the light blue line, with the maximum dual-polarimetric value marked as the hollow triangle.	63
Figure 3. 12	Same as Figure 3. 11 , but for an example of dissipation storm.....	64

Figure 3. 13 Same as Figure 3. 11 , but for an example of storm from developing stage to dissipation stage.....	65
Figure 3. 14 Maximum value of mean dual-polarimetric parameters, sort by maximum accumulative reflectivity. Number at the left-hand side in each figure is the value of maximum accumulative reflectivity of each case; x-axis for time, y-axis for cases. (a) Maximum value of mean ZHH (b) Maximum value of mean ZDP (c) Maximum value of mean ZDR (d) Maximum value of mean KDP.	66
Figure 3. 15 Vertical slope of mean dual-polarimetric parameters, sort by maximum accumulative reflectivity. Number at the left-hand side in each figure is the value of maximum accumulative reflectivity of each case; x-axis for time, y-axis for cases. (a) Vertical slope of mean ZHH (b) Vertical slope of mean ZDP (c) Vertical slope of mean ZDR (d) Vertical slope of mean KDP.....	67
Figure 3. 16 Number density distribution of dual-pol parameters vertical slope and maximum value with the time relative to the maximum accumulative reflectivity time. From the top panel to the bottom panel are ZHH, ZDP, ZDR and KDP. Left column for vertical slope and right column for maximum value.....	68
Figure 3. 17 Boxplot of maximum vertical value and tendency of maximum value relative to max. acc. Z_{HH} divided in 4 groups. Left column for maximum value and right column for maximum value tendency. Magenta lines are the connection of Q2. (a), (b) for ZHH. (c), (d) for ZDP. (e), (f) for ZDR. (g), (h) for KDP.....	69
Figure 3. 18 Boxplot of vertical slope and tendency of vertical slope relative to max. acc. Z_{HH} divided in 4 groups. Left column for vertical slope and right column for tendency of vertical slope. Magenta lines are the connection of Q2. (a), (b) for ZHH. (c), (d) for ZDP. (e), (f) for ZDR. (g), (h) for KDP.....	70
Figure 3. 19 Time distribution of maximum dual-polarimetric parameters relative to max. acc. Z_{HH} . Blue line for ZDR; Red line for KDP; Magenta line for ZDP. (a) All cases. (b) Strong cases only. (c) Weak cases only.	71

Figure 3. 20	A conceptual model of ZDR and KDP characteristics during storm evolution. X-axis shows the storm evolution; Left y-axis shows the approximately height and right y-axis shows the relative mean value of DPMs, black solid line for mean ZDR value and black dash line for mean KDP value. Orange (Blue) shading represent the percentage of time distribution of max. acc. KDP (max. acc. ZDR) relative to max. acc. ZHH time.	72
Figure 3. 21	Storm horizontal distribution of reflectivity during the storm track at 2-kilometer height of case 22. Shading represent reflectivity in dBZ. Blue dot line is the storm path. Green cross is the storm reflectivity weighted center. Blue and black contour lines are the enhance ZDR and KDP region, with the center of enhance region shown as blue and black square respectively.	73
Figure 3. 22	Enhance ZDR and KDP center path at different height of case 22. (a) 3-kilometer height. (b) 2.5-kilometer height. (c) 2-kilometer height.	74
Figure 3. 23	Hodograph and vectors of case 22. (a) Hodograph of 00 UTC sounding data. Meaning of different vectors in (b), (c), (d), (e) and (f) are as below: Black color for cell motion; Red color for system motion; Blue color for storm propagation; Magenta color for separation vector; Light green color for wind shear between 0 to 6 km height; Grass green color for storm relative wind shear. Numbers behind are the speed of each vector.	75
Figure 3. 24	Same as Figure 3. 20 , but for case 20.	76
Figure 3. 25	Enhance ZDR and KDP center path at different height of case 20. (a) 3-kilometer height. (b) 2-kilometer height. (c) 1-kilometer height.	77
Figure 3. 26	Same as Figure 3. 22 , but for case 20.	78
Figure 3. 27	Same as Figure 3. 20 , but for case 34.	79
Figure 3. 28	Enhance ZDR and KDP center path at different height of case 34. (a) 3-kilometer height. (b) 2-kilometer height. (c) 1.5-kilometer height.	80
Figure 3. 29	Same as Figure 3. 22 , but for case 34.	81
Figure 3. 30	Same as Figure 3. 20 , but for case 29.	82

Figure 3. 31	Enhance ZDR and KDP center path at different height of case 29. (a) 4-kilometer height. (b) 3.5-kilometer height. (c) 3-kilometer height.	83
Figure 3. 32	Same as Figure 3. 22 , but for case 29.....	84
Figure 3. 33	Same as Figure 3. 20 , but for case 30.....	85
Figure 3. 34	Enhance ZDR and KDP center path at different height of case 30. (a) 3-kilometer height. (b) 2-kilometer height. (c) 1-kilometer height.	86
Figure 3. 35	Same as Figure 3. 22 , but for case 30.....	87
Figure 3. 36	Distribution of storm propagation and maximum accumulative reflectivity of 38 cases.....	88
Figure 3. 37	Distribution of different vector, separated by storm strength. Parentheses in x-axis present the number of weak and strong cases. (a) Cell motion (b) System motion (c) Storm propagation.	89

Chapter 1 Introduction

1.1 Motivation

In terms of the intensity and the duration, the convective precipitation systems can be either strong intensity with short temporal duration or moderate intensity with long duration. Both of these two types of convective precipitation systems can cause severe disasters as the accumulated rainfall reach the limitation of the capacity. The evolution of microphysical process of the precipitation system plays crucial role in modulating the surface rainfall. Better understanding the evolution and development of these storms from various of observational data is key to improve their short predictability.

[Liu \(2018\)](#) investigate microphysical process of seven heavy rainfall events from SoWMEX/TiMREX. The collocated observations of NCAR SPOL radar (National Center for Atmospheric Research S-band Dual Polarization Doppler Radar) and 16 disdrometers were analyzed to understand the relation of surface DSD (drop size distribution) of rain and vertical structures of various DPMs (dual-polarimetric measurements). However, to gain more understanding about the microphysical process of cell storms within the rainfall events, combining radar observations and storm evolution is an essential step.

With the development of dual-polarimetric capability, DPMs from radar can be used to reveal cloud microphysical properties and physical process. Previous studies ([Loeffler et al. 2020](#); [Loeffler and Kumjian 2018](#)) had investigated the distance between center of enhance Z_{DR} (differential reflectivity) region and center of enhance K_{DP} (specific differential phase shift) region for studying size sorting. The high correlation between microphysical process and dynamical effect is applied to investigate the helicity of super cell.

Even though dual-polarimetric radar can only observed microphysical process indirectly, the microphysical characteristics can be retrieved by using the dual-polarimetric parameters from radar data. With high spatiotemporal resolution DPMs, the shape of droplet and their distribution information can be obtained. Tracking storms with DPMs, characteristics of structural evolutions and microphysics processes can be investigated comprehensively. Subsequently, utilizing the knowledge of the evolutions of the kinematic and microphysical fields can improve the short forecast of convective precipitation systems. ([Loeffler and Kumjian, 2018](#))

1.2 Literature Review

Over the past few decades, various of the techniques have been developed to identify convective and stratiform region by applying thresholds for both reflectivity and size or using the fuzzy logic algorithm. By classifying the precipitation systems, the cloud dynamics and microphysics processes in different rainfall types are investigated utilizing observational data. Thus, the simulations of microphysical process in numerical models are improved. Applying storm tracking technique is essential to efficiently analyze massive dataset from radar measurements. Two types of tracking algorithm were utilize, the cross-correlation method including TINT (TINT Is Not TITAN; [Fridlind et al. 2019](#)), TREC (Tracking of Radar Echo with Correlations; [Rinehart and Garvey 1978](#)) and COTREC (Continuity of TREC vectors; [Li et al. 1995](#)); The centroid method including TITAN (Thunderstorm Identification, Tracking, Analysis, and Nowcasting; [Dixon and Wiener 1993](#)), SCIT (Storm Cell Identification and Tracking; [Johnson et al. 1998](#)) and ForTraCC (Forecast and Tracking the Evolution of Cloud Clusters; [Vila et al. 2008](#)). In addition, [Hu et al. \(2019\)](#) suggest that the cross-correlation method is better identify and track isolated cells, and centroid tracking algorithms may not capture the entire storm evolution of cells due to the depending on threshold values to identify storm cells.

[Dixon and Wiener \(1993\)](#) have proposed a methodology of thunderstorm real-time identification and tracking technique based on volume-scan radar data by applying threshold values for reflectivity (T_Z), storm size (T_V) and storm speed (T_S). The sensitivity tests for reflectivity threshold from 30-dBZ to 40-dBZ for convective storms were performed, and value of T_Z was selected as 35-dBZ to identify convective storm. Yet, single threshold value may not properly identify convective storm. [Steiner et al. \(1995\)](#) proposed an algorithm to separate the radar echo into convection and stratiform area by applying three criteria, namely reflectivity intensity, peakness and surrounding grids. The influence radius for surrounding grids and the reflectivity threshold are the functions of area-averaged background reflectivity. [Yang et al. \(2013\)](#) developed a fuzzy logic (FL) algorithm to classify convective and stratiform rainfall based on radar reflectivity observations. By setting the membership function, the FL algorithm derived the classifications in a probabilistic manner.

Even though there are numerous algorithms of storm identification and tracking, detailed analysis in microphysical process through Lagrangian description had not appeared until the appearance of dual-polarization radar ([Yuter and Houze 1995](#), [Ryzhkov and Kumjian 2009](#), [Homeyer et al. 2020](#), [Loeffler et al. 2020](#), [Wapler 2021](#)). [Loeffler and Kumjian \(2018\)](#) utilized three-and-a-half-year dataset from July 2013 to December 2016 over the mid-Atlantic and southeastern United States, aim to reveal any characteristics in different stage of nonsupercell tornadic storms for which polarimetric radar data are available. It shows that the distance between the centroid of enhance Z_{DR} and K_{DP} will reach maximum value when the tornado occurs. In addition, the separation orientation will tend to be more orthogonal to storm motion around the tornado touch down report. [Loeffler and Kumjian \(2018\) intend](#) to utilize this feature to aid tornado forecast. Even though tornado is rare in Taiwan, the Z_{DR} and K_{DP} separation of convective storms in Taiwan is worthy further investigation to understand the correlation between the characteristics of dual-polarimetric parameters and the environmental

dynamical field.

[Hu et al. \(2019\)](#) investigate four different types of convective storms including shallow convection, isolated deep convection, multi-cell convective storm and supercell. Time height cross section of DPMs [Reflectivity (Z_{HH}), Differential Reflectivity (Z_{DR}), Specific Differential Phase Shift (K_{DP}) and Correlation Coefficient (ρ_{hv})] were examined. An example of isolated deep convective storm with mixed-phase processes are shown in **Figure 1. 1** (adopted from Hu et al. 2019). The cell continued to grow for 25 minutes until the echo top reach around 16 km height and subsequently dissipated after 30 minutes of initial identification (**Figure 1. 1** (a)). The convective process can be inferred from the time-height cross section. **Figure 1. 1** (a) shows a strong convective core at $t=30$ min and $H=8$ km, which descends and reaches the surface after 5 to 10 minutes along the black line. The green line in **Figure 1. 1** (b) marks a Z_{DR} column that represent the largest raindrops which form in the convective updraft, reach the surface at 5 to 10 minutes before the main precipitation shaft (the black line). Large K_{DP} value marked by the blue line in **Figure 1. 1** (c) reached the surface at around 5 minutes after the main precipitation shaft. **Figure 1. 1** (d) shows the correlation coefficient (ρ_{hv}) less than 0.9 at $t=30$ min and $h=6$ km, illustrate a strong signal of hail and graupel. **Figure 1. 1** (e) to **Figure 1. 1** (h) are the retrieved mean volume diameter (D_m), normalized raindrop concentration (N_w), integrated very high frequency (VHF) lighting sources and the hydrometeor classifications respectively. Similar investigation of DPMs time-height cross section is proposed in this study. An analytical method by calculating the vertical slope of DPMs at each storm track time is obtained to understand the microphysical processes of convections. The goal is intending to reveal transitional signal from storm development stage to dissipation stage.

Understanding the microphysical process not only facilitates the short-term forecast but also improve the microphysics scheme in numerical models. [Fridlind et al. \(2019\)](#) had compared the storm physics of isolated cell tracks from observations and simulations. Result

showing that although the Z_{DR} and K_{DP} patterns are similar, the strength in Z_{DR} (K_{DP}) column of simulations may be an order greater (weaker) than observations, illustrate that there is still room for improvement of the microphysics scheme.

Diverse environmental conditions and microphysics processes in Taiwan are different from other regions. The heavy precipitation events are mainly associated with Mei-Yu systems. Various studies investigate heavy precipitation systems using sophisticated NCAR SPOL data from SoWMEX/TiMREX. [童\(2009\)](#) has arranged the weather pattern during the entire experiment. [汪\(2009\)](#), [陳\(2009\)](#), [蔡\(2009\)](#), [盧\(2018\)](#) had studied the characteristics of drop size distribution (DSD) during the campaign. Furthermore, research related to simulation and data assimilation in different intensive observation period (IOP) and distinct microphysical scheme were well studied ([錢 2010](#), [邱 2010](#), [陳 2011](#), [廖 2014](#), [邵 2015](#), [陳 2017](#), [鄭 2017](#), [陳 2018](#), [梁 2019](#)). There are several studies of the precipitation structure through both observations and simulations. Yet, seldom study aims to investigate the microphysical process within the single convective core which were embedded in the precipitation system. Investigating the characteristics of microphysical process in different development stage of storm are expects to improve storm predictability.

1.3 Research Purposes

Previous studies had illustrated the relationship between storm development and microphysical process by studying dual-polarimetric parameters features. Both observational and numerical simulation studies focus on few cases study of convective cells. This research will focus on the statistical performance of convective storms by the high-quality NCAR SPOL radar data collected from the SoWMEX/TiMREX experiment. The objective of this research is to utilize the advantage of storm tracking technique and investigate statistical Lagrangian features of DPMs from storm development to dissipation stage.

1.4 Paper Structure

The structure of this study includes a methodology section and a results section. The Methodology section includes details about the SoWMEX/TiMREX international field campaign, storm identification and tracking algorithm, and the usage of reanalysis data, also the dual-polarimetric parameters presentation. The results section includes the overview of the SPOL observation from the international field campaign, consequences of both horizontal and vertical dual-polarimetric parameter separation, also the motion vectors combining both observations and reanalysis data.

Chapter 2 Data and Methodology

Before the analysis of convective storms evolution, a storm identification and tracking technique using radar data is proposed and applied to NCAR SPOL data. In this section, both radar data processing and synoptic reanalysis data will be introduced first. The storm tracking technique will be introduced as well. Finally, a brief introduction of dual-polarimetric parameters.

2.1 International Field Campaign

In 2008, from May 15th to June 30th, the Southwest Monsoon Experiment (SoWMEX, also called TiMREX, Terrain-Influenced Monsoon Rainfall Experiment) was held in Southern Taiwan. The goal of this experiment is to improve the capability of QPE and QPF (Quantitative Precipitation Estimation and Quantitative Precipitation Forecasting) during the Asian Summer Monsoon season. To investigate the characteristics of microphysical rainfall process, especially the duration of microphysical characteristics related to the heavy rain, various rainfall measurements were set at the northern Taiwan, including NCAR SPOL (S-band dual-polarimetric Doppler radar system), Team-R (X-band mobile polarimetric Doppler radar system), and MRR (Micro Rain Radar systems). Location of SPOL radar is shown in **Figure 2.**

1. During the experiment, 9 Intensive Observing Period (IOP) were implements. Date period are as follows:

IOP 1 : 0519 0600 Z – 0522 0000 Z ; IOP 2 : 0527 0600 Z – 0529 2100 Z

IOP 3 : 0529 2100 Z – 0531 2100 Z ; IOP 4 : 0601 2100 Z – 0603 1500 Z

IOP 5 : 0603 1800 Z – 0604 1200 Z ; IOP 6 : 0604 1800 Z – 0606 1200 Z

IOP 7 : 0612 0000 Z – 0613 1200 Z ; IOP 8 : 0614 0000 Z – 0617 1200 Z

IOP 9 : 0623 0600 Z – 0626 1200 Z

During the IOPs, soundings were launched every 3-hour. By collecting the sounding data, environmental wind can be obtained. The nearest station to the NCAR SPOL radar (longitude = 120.43 °E , latitude = 22.53 °N), Pingtung Airport (46750) sounding, were chosen to reveal the environmental condition in this study.

2.2 Reanalysis dataset

Owing to the fact that the sounding data is only available for IOP cases, the reanalysis datum is utilized for non-IOP cases. The reanalysis dataset is collected from the European Centre for Medium-Range Weather Forecasts (ECMWF). ECMWF Reanalysis – Interim (ERA-Interim) is the product chose for the further analysis. The spatial resolution is set as $0.125^{\circ} \times 0.125^{\circ}$ in longitude and latitude; The temporal resolution is about 6-hour (00 UTC, 06 UTC, 12 UTC, 18 UTC). With 37 vertical pressure levels (1000 hPa to 775 hPa by 25, 750 hPa to 300 hPa by 50, 250 hPa to 100 hPa by 25, 100, 70, 50, 30, 20, 10, 7, 5, 3, 2, 1). The parameters used in this study are the U and V component of wind.

2.3 Storm Identification and Tracking System

Based on the storm identification and tracking algorithms from [Dixon and Wiener \(1993\)](#), a storm identification and tracking system “SMART” (Storm Motion Analysis by Radar Tracking) was developed by Radar Metrology Laboratory in Department of Atmospheric Science, National Central University. SMART is first applied in the study of [吳\(2019\)](#). The SMART is utilized to investigate the characteristics of initiation, intensity and

duration of maritime and continental convections under weak synoptical scale forcing condition during warm season.

2.3.1 Radar Data Processing

SMART can process both 2-Dimensional and 3-Dimensional composite radar data and single radar data as long as the Radar coordinates data were transformed into Cartesian coordinates. This study focuses on the single radar datasets with 0.5-kilometer horizontal resolution and 0.5-kilometer vertical resolution within 150-kilometer radar radius and 20-kilometer height.

For data quality controls of NCAR S-POL radar, the entire process is similar to [盧 \(2018\)](#), but modify the thresholds for both ρ_{HV} and L_{DR} to maintain more complete precipitation area. The data with the value of ρ_{HV} less than 0.6 and the value of L_{DR} greater than 0.0 dB will be removed. The S-POL radar can transmit and receive S-band horizontal and vertical EM-wave alternatively, which wavelength is about 10-centimeters. With the long wave length, S-POL has less attenuation issue; therefore, the structure of the storm can be observed.

A schematic flow diagram before storm identification is shown in **Figure 2. 2**. After the data quality controls of radar data (**Figure 2. 2 (a)**), data were interpolated into Cartesian coordinates in different levels, namely CAPPI (Constant altitude plan position indicator) (**Figure 2. 2 (b)**). Data format for 2-Dimensional storm identification is the MOSAIC dataset (**Figure 2. 2 (c)**), which found the maximum reflectivity at each column above the grid point. After the well-prepared dataset, SMART can successfully provide cell properties which we are interested in.

2.3.2 2-Dimensional and 3-Dimensional Storm Identification

To analysis the complexity of the mesoscale convective system (MCS), storm identification by selecting single threshold for reflectivity can be problematic. Due to the composition structure of mesoscale convective systems, MCSs are commonly form by composition of numerous convective cores and a wide spread stratiform precipitation area. When applying storm identification with a single reflectivity threshold, part of the information of weak convection and dissipating convection can be missing. For instance, a strong reflectivity threshold can capture the convective core within the entire system, however, for the analysis of cell structure, only the mature stage during the storm evolution can be capture; On the other hand, a weak reflectivity threshold can capture the entire precipitation region. Precipitation cells without a convective core may also be missed identified, therefore, a cell which only contains the stratiform precipitation area will contaminate the analysis result of convective storm. Consequently, the idea of dual-reflectivity thresholds technique is proposed in this study. It is designed to capture the complete precipitation system only when the convective core existed.

According to [Dixon and Wiener \(1993\)](#), both 2-Dimensional and 3-Dimensional storm identification algorithm in SMART can identify thunderstorms by giving a threshold for both storm reflectivity intensity (T_Z) and storm size (T_V). The value T_Z was set as 35 dBZ and T_V was set as 10 km² for storm identification in [Dixon and Wiener \(1993\)](#). In this study, two reflectivity thresholds (T_Z) were applied to distinguish a storm region. To investigate the sensitivity of the precipitation area to the reflectivity threshold. T_Z was test from 15 to 35 dBZ with 5 dBZ interval, using the QPESUMS (Quantitative Precipitation Estimation and Segregation Using Multiple Sensor) data from CWB (Central Weather Bureau). An example of May 21, 2014 Mei-Yu case is shown in **Figure 2. 3**. The 15-dBZ captures the entire system including both convective and stratiform precipitation types. On the contrary, the 35-dBZ

captures smaller domain but the core of the convective system.

Based on the results of the various threshold values of T_Z and T_V , lower reflectivity threshold ($T_{Z,parent}$) and higher reflectivity threshold ($T_{Z,child}$) are determined as 30 and 35 dBZ objectively and theoretically for the final thresholds in this study. Three different storm identification results were derived. $T_{Z,parent}$ for identifying “parent cell”, $T_{Z,child}$ for identifying “child cell” and the storm content both convective core and precipitation area for “cell embed”.

A schematic diagram of cell number and area in different reflectivity threshold is shown in **Figure 2. 4**. There were four cells identified by 35 dBZ reflectivity threshold as shown in **Figure 2. 4 (a)**, which represent “child cell”. In **Figure 2. 4 (b)**, three cells were identified by 30 dBZ reflectivity threshold, which represent “parent cell”. From **Figure 2. 1 (a)** and **(b)**, parent-cell-1 only contains one child cell (child-cell-1); parent-cell-2 contains three child cells (child-cell-1, 2 and 3); However, parent-cell-3 contains none of the child cell. Therefore, while applying dual-reflectivity threshold (Dual_dBZ; **Figure 2. 1 (c)**), parent-cell-1 and 2 will be maintain as cell-embed-1 and 2, which maintain both convective core from child cell and precipitation area from parent cell. Due to lacking convective core at parent-cell-3, it will be excluded by the Dual_dBZ threshold method in this study. Thus only 2 cells remain (cell-embed-1 and 2) for further statistical analysis.

For the identified storms, the storms with storm size (T_V) less than 10 km^2 in 2-Dimensional radar data are also removed; or remove the storms which storm size (T_V) are less than 10 km^3 in 3-Dimensional radar data, same as the setting from [吳\(2019\)](#). A schematic diagram is drawn in **Figure 2. 5**. Numbers in colored grid points represent the area identified by different reflectivity thresholds, “1” for 30 dBZ and “2” for 35 dBZ. Where storm 1, 2 and 3 are the storms we are interested in. Storm 1 and 3 stands for storm embed with only one child cell in one parent cell; Storm 2 stand for simple parent cell; Storm 4 and 5 were ignored due to

the insufficient area.

2.3.3 Storm Properties

In order to analyze structure properties and cloud microphysical characteristics against convective storms, properties of storms need to be calculated after identifying cell storm. Due to the gridded data set, it is straightforward to calculate storm properties. Storm parameters which we had calculated are as follows:

- Area

$$A = n \, dx \, dy \quad (km^2) \quad (2-1)$$

where n is the number of grid points that the storm contains, dx and dy are the Cartesian grid spacing in x and y, respectively.

- Volume

$$V = \sum_{i=1}^h A_i \, dz \quad (km^3) \quad (2-2)$$

where h is number of layers which we conduct the interpolation calculation, dz is the Cartesian grid spacing in z.

- Geometric Centroid

$$\bar{x}_g = \left(\sum_{i=1}^n x_i \right) \times \frac{1}{n} \quad ; \quad \bar{y}_g = \left(\sum_{i=1}^n y_i \right) \times \frac{1}{n} \quad (2-3)$$

- Reflectivity Weighted Centroid

$$\bar{x}_e = \left(\sum_{i=1}^n x_i \times \left(\frac{Z_i}{n} \right) \right) \times \frac{1}{n} \quad ; \quad \bar{y}_e = \left(\sum_{i=1}^n y_i \times \left(\frac{Z_i}{n} \right) \right) \times \frac{1}{n} \quad (2-4)$$

where Z_i is the echo of each grid point.

- Orientation

$$\theta = \tan^{-1} \left(\frac{\nu}{\mu} \right) \quad (^\circ) \quad (2-5)$$

where μ and ν are the normalized eigenvector of the covariance matrix.

- Major and Minor axis

$$r_{major} = \sigma_{major} \left(\frac{A}{\pi \sigma_{major} \sigma_{minor}} \right)^{1/2}$$

$$r_{minor} = \sigma_{minor} \left(\frac{A}{\pi \sigma_{major} \sigma_{minor}} \right)^{1/2} \quad (\text{km}) \quad (2-6)$$

where σ_{major} and σ_{minor} are the standard deviation of the data in the u and v direction. More detail information were mentioned in [Dixon and Wiener \(1993\)](#).

2.3.4 2-Dimensional Moment Invariants

The translation, rotation and scaling of identified storms evolve drastically in a short period of time. To gain a better matching result of storm tracking, an algorithm solving pattern recognition problems were applied. Moment invariants theory is use to numerical the graphics geometric characteristics ([Hu 1962](#), [陳 et al. 2016](#)). There are four invariants that we often used in atmospheric science to describe storms feature and evolution. The two-dimensional 0^{th} order moments present physical quantity of storm area; 1^{th} order moments present the parameters related to storm shape; 2^{nd} order moments present the difference of storm area and shape; 3^{rd} order moments present degree of distortion of storm (describe the degree of image asymmetry). The concept are as follows:

Two-dimensional $(p + q)^{th}$ order moments of a continuous function for convective identification $f_{(x,y)}$ are assume. Where $(p + q)^{th}$ order moments are defined as below:

$$m_{pq} = \int_{-\infty}^{\infty} \int_{-\infty}^{\infty} x^p y^q f_{(x,y)} dx dy \quad , \quad p, q = 0, 1, 2, \dots \quad (2-7)$$

Where x and y are the coordinate position along the x and y direction.

The central can be written as:

$$\hat{x} = \frac{m_{10}}{m_{00}} \quad ; \quad \hat{y} = \frac{m_{01}}{m_{00}} \quad (2-8)$$

Center moment relative to the central are defined as follow:

$$\mu_{pq} = \int_{-\infty}^{\infty} \int_{-\infty}^{\infty} (x - \hat{x})^p (y - \hat{y})^q f_{(x,y)} dx dy \quad , \quad p, q = 0, 1, 2, \dots \quad (2-9)$$

After normalization by reference scale, center moments are defined as:

$$\eta_{pq} = \frac{\mu_{pq}}{\mu^{1+\frac{(p+q)}{2}}} \quad , \quad p + q = 2, 3, 4, \dots \quad (2-10)$$

With the basis of non-linear combination from η_{pq} , seven features ($\phi_1 \sim \phi_7$) with physical and geometric significance derived by 2nd and 3rd order moments were present after rotation coordinates.

$$\phi_1 = \eta_{20} + \eta_{02} \quad (2-11)$$

$$\phi_2 = (\eta_{20} - \eta_{02})^2 + 4\eta_{11}^2 \quad (2-12)$$

$$\phi_3 = (\eta_{30} - 3\eta_{12})^2 + (3\eta_{21} - \eta_{03})^2 \quad (2-13)$$

$$\phi_4 = (\eta_{30} + \eta_{12})^2 + (\eta_{21} + \eta_{03})^2 \quad (2-14)$$

$$\begin{aligned} \phi_5 = & (\eta_{30} - 3\eta_{12})(\eta_{30} + \eta_{12})[(\eta_{30} + \eta_{12})^2 - 3(\eta_{21} + \eta_{03})^2] \\ & + (3\eta_{21} - \eta_{03})(\eta_{21} + \eta_{03})[3(\eta_{30} + \eta_{12})^2 - (\eta_{21} + \eta_{03})^2] \end{aligned} \quad (2-15)$$

$$\begin{aligned} \phi_6 = & (\eta_{20} - \eta_{02})[(\eta_{30} + \eta_{12})^2 - (\eta_{21} + \eta_{03})^2] \\ & + 4\eta_{11}(\eta_{30} + \eta_{12})(\eta_{21} + \eta_{03}) \end{aligned} \quad (2-16)$$

$$\begin{aligned} \phi_7 = & (3\eta_{21} - \eta_{03})(\eta_{30} + \eta_{12})[(\eta_{30} + \eta_{12})^2 - 3(\eta_{21} + \eta_{03})^2] \\ & - (\eta_{30} - 3\eta_{12})(\eta_{21} + \eta_{03})[3(\eta_{30} + \eta_{12})^2 - (\eta_{21} + \eta_{03})^2] \end{aligned} \quad (2-17)$$

Notice that for the continuous function graphic, the changes of translation, scale and rotation of the above seven features will not be changed. Normalization are computes after calculating the seven features:

$$V_k = \frac{\phi_k - (\phi_k)_{min}}{(\phi_k)_{max} - (\phi_k)_{min}} \quad , \quad k = 1, 2, 3, \dots, 7 \quad (2-18)$$

The value of V_k will lies between 0 and 1, represent the similarity among all storms.

To quantify the similarity of storms, the portion of current time period (superscript =0) and the portion of the following time period (superscript =i) are expressed as a seven-dimensional vector:

$$\begin{aligned} P^0 &= [V_1^0, V_2^0, V_3^0, V_4^0, V_5^0, V_6^0, V_7^0] \\ P^i &= [V_1^i, V_2^i, V_3^i, V_4^i, V_5^i, V_6^i, V_7^i] \end{aligned} \quad (2-19)$$

After that, we can calculate the distance similarity (DS) and the angle similarity (AS) between two vectors:

$$DS_{(P^i, P^0)} = 1 - \frac{D_{(P^i, P^0)}}{\max[D_{(P^i, P^0)}]} \quad (2-20)$$

$$AS_{(P^i, P^0)} = 1 - \frac{\cos^{-1}\left(\frac{\langle P^i \cdot P^0 \rangle}{\|P^i\| \cdot \|P^0\|}\right)}{\pi} \quad (2-21)$$

Where $D_{(P^i, P^0)}$ is the Euclidean distance ($D_{(P^i, P^0)} = \sqrt{\sum_{k=1}^7 (V_k^i - V_k^0)^2}$);

$\langle P^i \cdot P^0 \rangle$ is the inner product ($\langle P^i \cdot P^0 \rangle = \sum_{k=1}^7 V_k^i \cdot V_k^0$);

$\|P^i\|$ and $\|P^0\|$ are the length ($\|P^i\| = \sqrt{\sum_{k=1}^7 (V_k^i)^2}$; $\|P^0\| = \sqrt{\sum_{k=1}^7 (V_k^0)^2}$).

According to the eq. (2-24) and eq. (2-25), once the value of DS and AS are closer to “1”, the closer vector length and smaller included angle they are. In our study, the final momentum invariant term (M) is set as equation (2-22). In the case of unknowing whether the DS or the AS is much more important, the weighting of DS and AS are set as equally.

$$M = 1 - (0.5 (DS + AS)) \quad (2-22)$$

2.3.5 2-Dimensional Storm Tracking Methodology

In this study, 2-D Tracking algorithm were used. According to [Dixon and Wiener \(1993\)](#), cell matching factors include the differences of distance (dD) and area (dA) between cells within two volume scans (t_1, t_2) are considered in the tracking algorithm. Furthermore, [吳 \(2019\)](#) had shown that considering the momentum invariant (M) factor can slightly improve the accuracy of storm track. Thus, the tracking algorithm is to obtain minimum difference of the distance, size and momentum invariant of final matching cells from two volume scans. The difference, here after is considered as “Cost Function”, and can be obtained as follow:

$$\begin{aligned} \text{Suppose the state of storm } i \text{ at } t_1 : S_{t_1 i} &= (x_{et_1 i}, y_{et_1 i}, A_{t_1 i}, M_{t_1 i, t_2 j}) \\ j \text{ at } t_2 : S_{t_2 j} &= (x_{et_2 j}, y_{et_2 j}, A_{t_2 j}, M_{t_2 j, t_3 k}) \end{aligned} \quad (2-23)$$

(assuming there are n_1 storms at t_1 and n_2 storms at t_2)

X and Y represent the location of the storms. The A represent the area of the storm.

It is defined that the ‘‘Cost’’ from state S_{t_1i} to state S_{t_2j} is obtained as follow:

$$\text{Cost} = dD + dA + dM \quad (2-24)$$

$$dD = \sqrt{(x_{et_1i} - x_{et_2j})^2 + (y_{et_1i} - y_{et_2j})^2} \quad (2-25)$$

$$dA = \left| \sqrt{A_{t_1i}} - \sqrt{A_{t_2j}} \right| \quad (2-26)$$

$$dM = \frac{dD + dA}{2} \times M \quad (2-27)$$

Additional assumptions are:

1. We consider that the shorter differences distance of storms, the more likely to be the same one.
2. Storms of which storm size were similar, the higher probability to be the same one.
3. If the value of ‘M’ is closer to ‘0’, it also indicates the high possibility to be the same storm.
4. We also assume that it is impossible for storms to move over 1.8-kilometer per minutes. So, the maximum storm speed is set to 30 m/s to do the further matching. According to [Dixon and Wiener \(1993\)](#), the maximum expected storm speed was revised from 1-kilometer per minutes to 1.8-kilometer per minutes, the liberalized of storm speed will ensure to capture storm in a faster motion

Through the entire process, a successful storm track will contain numerous cells. Information of cell parameters during the entire storm path will be recorded. Therefore, storm duration, storm movement direction, storm evolution including area and strength ... etc. can be obtained. The storm microphysical process through the evolution of dual-polarimetric parameters can be investigated as well. The selected storms will be introduced at chapter 3.

2.4 Dual-Polarimetric Parameters

Unlike the Doppler radar, dual-polarimetric radar transmits and receives both horizontal and vertical pulse of radio waves. By utilizing the DPMs, the information of hydrometeors including size, shape, phase composition and more can be obtained. The DPMs used in this study are listed as following:

- Reflectivity (Z_{HH}) [units: dBZ]

Z_{HH} is one of the products of co-polar scattering process. It transmits and receive the same polarization electromagnetic (EM) wave. From receiving the backscattered powers from precipitation particles, Z_{HH} is determined by the size and distribution of hydrometers. Assuming the particle shape is spherical and particle size is smaller than wavelength, the back-scattering cross section in Rayleigh region can be written as bellow:

$$Z_{HH} = \int_{D_{min}}^{D_{max}} D^6 N(D) dD \quad (2-28)$$

The stronger backscattered powers, the bigger drop size or more particles exist.

- Differential Reflectivity (Z_{DR}) [units: dB]

Z_{DR} is the logarithmic ratio of the backscattered powers from horizontal and vertical polarizations. According to [Seliga and Bringi \(1976\)](#), Z_{DR} can be written as equation (2-29).

$$Z_{DR} = 10 \log_{10} \left(\frac{Z_{HH}}{Z_{VV}} \right) \quad (2-29)$$

For those spherical hydrometers, the Z_{DR} equals to zero as the equivalent power at both horizontal and vertical polarization. As the increasing of the rain drop size, the suffer air resistance changes the drop shape to flatter during the descent. Therefore, larger Z_{DR} will be observed from big drops. Besides, the EM wave is much more sensitive to liquid-phase hydrometers compare with ice-phase

hydrometers. That is, for a given size of rain and hail, the Z_{DR} value of rain will be much larger than the Z_{DR} value of hail. The measurement of Z_{DR} is often used for the following research: (a) Particle size estimation (b) Quantitative precipitation estimation (QPE) of rain and ice (c) Radar quality control of system bias correction. To insure the hydrometers were in the warm rain process, showing a positive correlation between Z_{DR} value and drop size in this study. Only the Z_{DR} values below 4-kilometer height were analyzed. To investigate the spatial distribution of drop size quantitatively, vertical slope of Z_{DR} in vertical profile were calculated. The positive value of vertical slope represents the larger hydrometers locates at a higher level; On the contrast, negative vertical value of slope represents the larger hydrometers were at the low level.

- Difference Reflectivity (Z_{DP}) [units: dB]

Z_{DP} was defined as the difference between horizontal and vertical reflectivity, it can be express as equation (2-30). Which is only defined for rain medium ($Z_{HH} > Z_{VV}$).

$$Z_{DP} = 10 \log_{10}(Z_{HH} - Z_{VV}) \quad (2-30)$$

For ice particles, they tumble while falling, made the Z_{HH} nearly equal to Z_{VV} . However, rain particles are become more oblate in shape with increase with size, and made the Z_{HH} larger than Z_{VV} . For the reason mention above, this implies that Z_{DP} is insensitive to the ice particles ([Tong et al. 1998](#)).

- Differential Phase Shift (φ_{DP}) [units: °]

φ_{DP} is the difference phase shift between horizontal and vertical polarizations. Theoretically, φ_{DP} should be zero when radar emitting the EM wave. However, there's no perfect waveguide and will always exist a non-zero value of φ_0 . Therefore, φ_0 should be calculated at each radar bin and subtract φ_0 when calculating φ_{DP} . The observed φ_{DP} can be written as equation (2-31).

$$\varphi_{DP}^{ods} = \varphi_{DP} + \varphi_0 + \delta + Noise \quad (2-31)$$

Where $\varphi_{DP} = \varphi_H - \varphi_V$, δ is the backscatter differential phase shift. More detail descriptions were written in [Kumjian \(2013; see Part I\)](#). As we know, φ_{DP} is a phase measurement, it will not affect by attenuation of EM waves. For the above reason, we often use φ_{DP} for attenuation correction of radar data quality control.

- Specific Differential Phase Shift (K_{DP}) [units: $^{\circ}/km$]

By calculate the range derivative of φ_{DP} , a new dual-pol parameter named K_{DP} can be derive.

$$K_{DP} = \frac{1}{2} \left(\frac{d\varphi_{DP}}{dr} \right) \quad (2-32)$$

Compare with φ_{DP} , K_{DP} is much more straightforward to the region of liquid-phase hydrometers. Also, K_{DP} is related to emissive wavelength. For a given rain drop size, shorter wavelength will lead to higher value of K_{DP} . Unlike Z_{DR} is proportional to the mass-weighted mean diameter (D_m) of the system; K_{DP} is proportional to liquid water content (LWC). Hence, using Z_{DR} , K_{DP} and φ_{DP} for quantitative precipitation estimation (QPE) shows more accurate compare with using Z_{DR} and φ_{DP} only ([洪 2020](#)). To investigate the spatial distribution of LWC quantitatively, vertical slope of K_{DP} in vertical profile were calculated. The positive value of vertical slope represents the larger LWC locates at a higher level; On the contrast, negative vertical value of slope represent the larger LWC were at the low level, lead to a heavy precipitation.

- Correlation Coefficient (ρ_{HV}) [units: none]

The Correlation Coefficient is defined as the co-polar correlation between horizontal and vertical polarization EM waves. Under normal circumstances, the value of ρ_{HV} will lays between 0 to 1. For instance, in pure rain, ice or snow

region, ρ_{HV} will shows nearly 1; In the contrary, ρ_{HV} will attend to be lower than 0.8 in the mixing phase region. The lower ρ_{HV} is, the more likely to be the non-meteorology echo. The definition of ρ_{HV} can be written as equation (2-33). The application of ρ_{HV} in this study is for the radar data quality control.

$$\rho_{HV} = \frac{\langle S_{VV} S_{HH}^* \rangle}{\sqrt{\langle |S_{HH}|^2 \rangle \langle |S_{VV}|^2 \rangle}} \quad (2-33)$$

- Linear Depolarization Ratio (L_{DR}) [units: none]

L_{DR} is one of the products of cross-polar scattering process. Which means the radar will only transmit horizontal polarization waves but receive both horizontal and vertical channels.

$$L_{DR} = 10 \log \left(\frac{Z_{HV}}{Z_{HH}} \right) \quad (2-34)$$

For meteorological echo, L_{DR} will lays between -35 to 0. In rain region, L_{DR} shows more closer to -35 (mostly between -35 and -26). The application of L_{DR} in this study is for the radar data quality control.

Chapter 3 Results and Discussions

3.1 Overview of SoWMEX SPOL Observations

The weather conditions of each IOPs during SoWMEX/TiMREX are shown in **Figure 3. 1**. Blue boxes indicate the time period of IOPs; black boxes indicate the time period of non-IOPs. In general, IOP1 contains a widespread precipitation; IOP2 shows numerous of isolated convective cell; IOP3, IOP4 are the linear convective system moving toward the land; IOP5 contains a leading convective system with trailing stratiform precipitation; IOP6 contains linear convective system; IOP7 contains a frontal system associated with linear convective line came from the ocean; IOP8 contain convective line with widespread trailing stratiform propagated toward the land and a MCS (Mesoscale convective system) moving toward the land; IOP9 contains linear convective system organized by several isolated cells.

The entire NCAR SPOL radar data from SoWMEX/TiMREX were applied to SMART and the result of storm identification including the distributions of storm type (child-cell, parent-cell and cell-embed) will be introduced. From all of the daily numbers of child-cell (**Figure 3. 2 (a)**) and parent-cell (**Figure 3. 2 (b)**), three extremum storm number occurs at June 1st to 4th, June 14th to 16th and June 26th to 28th, which are IOP4, IOP5, IOP6, IOP8 and IOP9. Since the SoWMEX/TiMREX were from mid-May to the end of June, most of the precipitation systems are related to Mei-Yu front or East Asia southwesterly monsoon, which contains a wide stratiform region with several individual convective cell inside. The highest peak occurs in **Figure 3. 2 (a)** and **(b)** are corresponding to the period of IOP8. However, embed cells identified by dual-reflectivity threshold shown in **Figure 3. 2 (c)** does not appears the corresponding peak during IOP8, illustrate that most of the parent-cells contained more than one child-cell during IOP8. To understand the cell-embed distribution, a daily multiple cell distribution in logarithm

scale is shown is **Figure 3. 3**. The x-axis is the time, and y-axis is the number of child-cell within one parent-cell. In **Figure 3. 3**, it shows that most of the parent-cell contains one to three child-cell. However, a parent-cell can also contain up to dozens of child-cells. The result reveals the multicellularity of the East Asia southwesterly monsoon accompanies with Mei-Yu front.

To further investigate parent-cell area relative to other cell parameters. In **Figure 3. 4**, the distribution of parent-cell area corresponds to cell maximum reflectivity is shown. Even though the parent-cell area can spread widely over 25000 km², most of the maximum reflectivity are within 50 dBZ to 60 dBZ, with none of any cell reflectivity occurs over 70 dBZ during the entire experiment. In **Figure 3. 5**, the distribution of parent-cell area corresponding to number of child-cell embed is shown. No matter the area of parent-cell is from 20000 km² up to 25000 km², the greatest number of child-cell they can support will not exceed 52. From **Figure 3. 5**, a positive correlation was shown, with the increase of parent-cell area, number of child-cell embed also increase. **Figure 3. 6** shows the storm duration of each day from parent cells. Three peaks occur just at the time as **Figure 3. 2** shows, illustrate that although numerous cells were observed, most of them are in short life time (within 30 minutes). From **Figure 3. 7**, a vaguely negative correlation between storm maximum area and storm duration of parent cells is shown. It is postulated that splitting and merging of the storms causes the storm centroid shifted dramatically in a short period of time. Therefore, the tracking of storm ended due to splitting and merging. The storm split and merge had not been considered in SMART, which will be further improved in the future.

3.2 Case analysis

After reviewing all of the storm tracking results from NCAR SPOL observations, storm tracking with splitting and merging issues will be removed from further analysis. This study focuses on the isolated convections with sufficient tracking period. To select the interested cases,

three conditions were applied. First, single-cells are selected to avoid the complicated structure of multiple-cell. Second, storms of least 10 radar scans are selected to insure sufficient scans for analysis. Third, storm size should be adequately small to removed merging and splitting storms.

From **Figure 3. 8** (a), daily number of storm track from SMART with 30 dBZ reflectivity threshold, 10 km² area threshold and 30 m/s speed threshold is shown. In order to analyze complete life cycle of a storm, storm with short life time is filtered out. Therefore, a duration threshold of least 10 radar scans is applied. After filtering storms with insufficient radar scans, there were 780 storms left as shown in **Figure 3. 8** (b). Furthermore, an area threshold between 30 to 300 km² is further applied to avoid storms with multiple cells, and splitting and merging issues. Overall, there were 47 cases selected as shown in **Figure 3. 8** (c). Storm track paths are shown in **Figure 3. 9**. Line color represents different storm path with the case number nearby. Detail information of each case are present in **Table 1. 1**. Including storm start time (black dots), storm end time, the case number used in this study and the corresponding IOP experiment. Visual examine of each storm was implemented to ensure the tracking results of selected cases.

Considering the limitation of the scan strategy from single radar observation (e.g., blind zone), storms of which highest low-level blind zone (tL) must be lower than 2.5 kilometers height to insure the low-level structure of the storm was well observed. In addition, the lowest high-level blind zone (tC) must be higher than 3.5 kilometers height to assure the high-level structure of the storm was well observed. An example of the blind zone of storms in different time step is shown in **Figure 3. 10**. Black lines from the bottom to the top of each figure are the height of 3-, 5- and 10-kilometer, respectively. The gray area represents the effective observation area. Colored shaded is the storm area in the unit of dBZ. Dark purple shading shows the blind zone above the maximum elevation; Light purple shading shows the blind zone below the lowest elevation. From **Figure 3. 10** (a) to (k), storm moves away from the radar

through time, led to the height of both high-level blind zone (tC) and low-level blind zone (tL) of the storm increase with time. Finally, 38 cases are left (case 6, 9, 11, 14, 15, 24, 25, 31, 41 were removed).

The mean DPM profiles of each selected storm are thus obtained to investigate the Lagrangian microphysical characteristics. The DPMs including ZHH, ZDR, and KDP were averaged from each storm, thus the mean DPM profiles were obtained. Additional threshold of mean reflectivity lower than 20 dBZ was applied to removed low quality of DPMs due to low SNR (signal to noise ratio). For all the cases, time series of mean DPM profiles of each storm track are summarized in Appendix A and B. Appendix A for 17 weak cases; Appendix B for 21 strong cases. Three examples will be introduced in next section.

3.2.1 Statistical Characteristics of 38 Cases

Three different types of storm tracking result including developing stage (**Figure 3. 11**), dissipating stage (**Figure 3. 12**) and developing to dissipating stage (**Figure 3. 13**) are shown. The time before the storm reaches its mature stage are classify as the developing stage; On the contrary, the time after the storm reaches its mature stage are classify as the dissipating stage. The definition of mature stage of storms are mentioned below. The storm in development stage is chosen from June 14th, 2008. The storm case number is 30 and was tracked from 0000 UTC to 0115 UTC. **Figure 3. 11** (a) shows the vertical evolution profile of mean reflectivity in dBZ (where $DZ = Z_{HH}$). In this study, the maximum accumulative reflectivity (max. acc. Z_{HH}) is defined as the mature stage with most strong intensity of the storm track. The calculation of accumulative reflectivity (acc. Z_{HH}) is shown as below.

$$acc. Z_{HH} = \int_{max.tL+0.5}^{end} Z_{HH}(h) dh \quad (3-1)$$

In case 30, the maximum low-level blind zone (max. tL) appears at the 11th time step,

about 1-kilometer height (height of tL in each time step is marked as the black dot); the minimum high-level blind zone (min. tC) appears at the 1st time step, about 7-kilometer height (height of tC in each time step is marked as the blue dot). By calculating the accumulative reflectivity from the height of max.tL + 0.5 (1.5-kilometer for case 30) to the highest effective altitude at each time step (*acc. Z_{HH}* values were show as the pink line), maximum accumulative reflectivity (max. acc. *Z_{HH}*) was thus obtained (marked by the pink square). As shown in **Figure 3. 11** (a). The value of *acc. Z_{HH}* remain increasing from the initial track time to the end of the storm track, with the max. acc. *Z_{HH}* appears at the last time step (the 11th time step), indicating that the storm continues to growth within the entire storm track.

Figure 3. 11 (b) shows the vertical profile of mean *Z_{DP}* (where DP = *Z_{DP}*). The calculation of accumulative *Z_{DP}* is shown in equation (3-2). Different to *acc. Z_{HH}*, accumulation of DPMs (acc. DPM) calculates only the value from the height of max.tL + 0.5 to 4 kilometers height to insure only including warm rain processes. Due to the high correlation between *Z_{HH}* and *Z_{DP}*, pattern of **Figure 3. 11** (b) is similar to **Figure 3. 11** (a), but with less variation. In case 30, the max. acc. *Z_{DP}* occurs 2nd-time-step before the max. acc. *Z_{HH}*.

$$acc. Z_{DP} = \int_{max.tL+0.5}^4 Z_{DP(h)} dh \quad (3-2)$$

Figure 3. 11 (c) shows the vertical evolution profile of mean *Z_{DR}* (where DR = *Z_{DR}*). The calculation of accumulative *Z_{DR}* is shown in equation (3-3). The max. acc. *Z_{DR}* occurs at the time max. acc. *Z_{HH}* occurs, illustrating larger drop size appeared at the last time step of the storm track. Both *acc. Z_{DP}* and *acc. Z_{DR}* indicate the mean size of rain drop.

$$acc. Z_{DR} = \int_{max.tL+0.5}^4 Z_{DR(h)} dh \quad (3-3)$$

Figure 3. 11 (d) shows the vertical evolution profile of mean *K_{DP}* (where KD = *K_{DP}*). The calculation of accumulative *K_{DP}* is shown in equation (3-4). The max. acc. *K_{DP}* occurs at the same time step as max. acc. *Z_{DP}* (9th step). It shows that the highest liquid water content (LWC) appears earlier than forming numerous larger drop size.

$$acc. K_{DP} = \int_{max.tL+0.5}^4 K_{DP}(h) dh \quad (3-4)$$

In this study, all of the maximum accumulative DPMs were calculated to investigate the relationship between storm development and the characteristic of microphysical process.

A storm in dissipation stage is chosen from May 22th, 2008 (**Figure 3. 12**). The storm case number is 5 and was tracked from 0415 UTC to 0522 UTC. **Figure 3. 12** (a) to (d) shows the same time-height cross section as **Figure 3. 11** (a) to (d), but for the storm in dissipation stage. The acc. Z_{HH} in **Figure 3. 12** (a) shows the max. acc. Z_{HH} at the second time step of the track, and continuous decrease gradually all the way to the end of the storm track. In case 5, the height of the storm (mean reflectivity greater than 20 dBZ) decreased as the strength of storm decreasing.

Last example is chosen from May 22th, 2008 (**Figure 3. 13**), the storm case number is 4 and was tracked from 0345 UTC to 0507 UTC. **Figure 3. 13** (a) to (d) shows the same way of presenting time-height cross section as **Figure 3. 11** (a) to (d), but for storm evolution from development stage to dissipation stage. As shown in **Figure 3. 13** (a), the max. acc. Z_{HH} occurs at the 7th time step, with the increasing acc. Z_{HH} signal start from the initiation of the storm track to the max. acc. Z_{HH} , then follow by the decreasing acc. Z_{HH} signal to the end of the storm track. Showing the evolution of intensity in different storm stage. In this case, time step from 1 to 6 are define as the storm in developing stage, with the dissipation stage starting from the 8th time step to the 12th time step.

As discussed in [Hu et al. \(2019\)](#), storm dissipation stage is characterized as the maximum reflectivity reached its maximum height and during which the reflectivity decrease. Base on this concept, vertical slopes of the DPM were calculated (light blue lines in **Figure 3. 13**), from the height of max.tL + 0.5 km to 4-kilometer height. First of all, the maximum value and their corresponding height (marked as light blue hollow triangles in **Figure 3. 13**) need to be obtained at each time step to avoid missing data and clutter. If the height of the

maximum value is higher than $tL + 0.5$ km, the vertical slope will be calculated from $tL + 0.5$ to that level, a positive vertical slope will be derived, indicates that the DPMs increase with increasing altitude. On the contrary, if the height of the maximum value is just above the tL , thus the vertical slope calculated from $tL + 0.5$ km to 4-kilometers height, consequently, a negative vertical slope will be obtained. The positive vertical slope of Z_{DR} represent the larger droplet is floating at a higher altitude; a positive vertical slope of K_{DP} represent a higher liquid water content locates at a higher altitude. It is postulated that positive (negative) vertical slope can be referred the storm in the developing (dissipating) stage ([Hu et al. 2019](#)).

Maximum values of DPMs of each case are shown in **Figure 3. 14**. Time of the max. acc. Z_{HH} are define as $t = 0$. Negative value of t represents the time before max. acc. Z_{HH} , illustrating storm in developing stage. Positive value of t represent the time after max. acc. Z_{HH} , illustrating storm in dissipation stage. Cases were shown in order of their max. acc. Z_{HH} value, the magnitude of the max. acc. Z_{HH} value are shown at the left-hand side of each figure. Cases with higher max. acc. Z_{HH} value are shown at the upper part in each figures and cases with smaller max. acc. Z_{HH} values are shown at the bottom part of the figures. As **Figure 3. 14** (a) to (d) shown, larger value appears at stronger case with the largest value occurs around the max. acc. Z_{HH} .

Vertical slope of DPMs of each case are shown in **Figure 3. 15**. By calculating the vertical slope of different parameters, this study intent to find transition signal from develop to dissipation stage by looking for positive vertical slope to the negative vertical slope. Unfortunately, there is no clear tendency of positive vertical slope transferring to negative vertical slope. The signal of the vertical slope transition will be discussed comprehensively in the following next paragraph.

Figure 3. 16 shows the number density function (NDF) of vertical slope and maximum value with the time relative to the maximum accumulative reflectivity (max. acc. Z_{HH}). **Figure**

3. 16 (a) 、(c) 、(e) and (g) are the NDF of different mean DPMs vertical slope; **Figure 3. 16** (b) 、(d) 、(f) and (h) are the NDF of different mean DPMs maximum value. (a) and (b) for mean reflectivity (DZ); (c) and (d) for mean difference reflectivity (DP); (e) and (f) for mean differential reflectivity (DR); (g) and (h) for mean specific differential phase shift (KD). From **Figure 3. 16** (b), (d), (e), (f), (h), a descending signal after the max. acc. Z_{HH} are shown. **Figure 3. 16** (e) shows that larger rain drops have fallen to surface as the storm passed mature stage (vertical slope of Z_{DR} decreasing as storm passing mature stage). **Figure 3. 16** (b), (d), (f), (h) indicate that the strength of storms weakening after the time of max. acc. Z_{HH} .

To investigate the variety of slope quantitatively, the temporal evolution of vertical slope of DPMs were calculated before and after the max. acc. Z_{HH} . A positive tendency indicates vertical slopes increasing with time. However, if the vertical slopes decrease with time, a negative tendency will be obtained. The positive tendency suggests the ascending hydrometers and negative tendency represents descending hydrometeors. In order to capture the transitional signal from the development, mature to dissipation stage, time for the analysis distinguish by max. acc. Z_{HH} is required. As **Figure 3. 16** shown, most of the data appears around the max. acc. Z_{HH} , with the time aloof, quantity of data decrease.

For more accurate description of DPM characteristic during storm evolution, NDF of DPMs vertical slope and maximum value were distinguished into four groups to represent different storm evolution. Group 1 and 2 can be considered as developing stage of the storm. Group 3 and 4 can be considered as dissipating stage of storm. **Figure 3. 17** display the boxplots of maximum value and the tendency of maximum value in four groups. Group 1 includes the data with $-25 < t < -5$ and group 2 includes the data with $-5 < t < 0$. Group 3 includes the data with $0 < t < 5$ and group 4 includes the data with $5 < t < 25$. Red line in the middle of the blue box represent the median value of the dataset (hereafter Q2); Upper boundary line shows the 75th percentile of the dataset (hereafter Q3) and the bottom boundary line is the 25th percentile

of the dataset (hereafter Q1). From the maximum value (**Figure 3. 17** (a), (c), (e), (f)), it shows a clearly increasing from group 1 to group 2, with the maximum values for all DPMs reach the peak at group 2, subsequently decrease all the way to group 4 for all parameters. As for the tendency of the maximum value, the most positive value also occurs at group 2 in Z_{HH} , Z_{DP} and K_{DP} (**Figure 3. 17** (b), (d), (h)). However, the Z_{DR} value (**Figure 3. 17** (f)) shows a large variation from Q2 to Q3, indicates the noisily of Z_{DR} maximum value. Owing to Z_{DR} is a relative measurement between horizontal and vertical channel, the value is affected by the strength of the precipitation. Heavy precipitation tends to have a larger Z_{DR} compare to shallow precipitation.

To further examine the result, values of vertical slope and maximum are divided into 4 groups as well. The vertical slope and the tendency of vertical slope are shown as boxplot in **Figure 3. 18**. From values of vertical slope in **Figure 3. 18** (a), (c), (e), (g), Q2 shows the highest value at group 2 and then decrease at group 3. As for the vertical slope tendency (**Figure 3. 18** (b), (d), (f), (h)), most of the data of Z_{DR} (**Figure 3. 18** (f)) in group 3 are in negative also K_{DP} and Z_{DP} (**Figure 3. 18** (d) and (h)) have more negative value at group 4. Showing that the vertical slope decreases sharply of Z_{DR} first and then K_{DP} and Z_{DP} . Illustrate the larger drop size will falls earlier than smaller drop size.

To understand the characteristic of maximum accumulative time between different dual-polarimetric parameters, distribution of maximum accumulative DPMs relative to max. acc. Z_{HH} time of all 38 cases is shown in **Figure 3. 19** (a). However, peaks of all parameters show a highly overlap with max. acc. Z_{HH} . To further reveal with the DPM features, all of the cases were separated into strong and weak groups. As the max. acc. Z_{HH} exceeds 500 dBZ, it will be classified as a strong case. On the contrary, the max. acc. Z_{HH} is below 500 dBZ, will be classified as a weak case. There were 21 strong cases and 17 weak cases for examination. From the strong cases (**Figure 3. 19** (b)) most of the data shows a time lag with max. acc. K_{DP} appears first, max. acc. Z_{HH} and max. acc. Z_{DR} appear later and max. acc. Z_{DP} occurs at the

last. It is postulated that the larger size of rain drops forms by the collision-coalescence process as it descending to surface during maturing to dissipating stage. Before the collision-collection process, it is necessary to have sufficient LWC, and enhance the K_{DP} value during developing stage. Therefore, the time lag between maximum accumulative K_{DP} and Z_{DR} can be noticed. As discussed in [Hu et al. \(2019\)](#), the high Z_{DR} values occur at low level before the maximum reflectivity reaches the highest level are likely due to the early fallout of the heavier and larger raindrops. The result can also be found in **Figure 3. 19 (b)**, which the max. acc. Z_{DR} (blue square) first appears around $t = -10$. During the end of the dissipation stage ($t \geq 5$), more numerous smaller raindrops are inferred to reach the max. acc. K_{DP} time (red dot). This may likely due to the large raindrops had already fallen out. On the other hand, the weak cases (**Figure 3. 19 (c)**) shows the same result as **Figure 3. 19 (a)**, all the max. acc. DPMs appear at the same time, showing no significant time lag between different max. acc. DPM in weak storms.

To summary from the results of statistical characteristics of vertical profiles, a conceptual model during storm evolution is shown in **Figure 3. 20**. X-axis shows the time series from storm development stage to storm dissipation stage. Left y-axis shows the approximately height and right y-axis shows the relative mean value of DPMs, black solid line for mean Z_{DR} and black dash line for mean K_{DP} .

As the conceptual model shows, mean drop size reaches the maximum value at the time before the storm reaches its mature stage, then decreases from mature to dissipation stage (black solid line). From the mean value of K_{DP} (black dash line), the peak of mean value also occurs at the time before the mature stage of storm, then decrease all the way to the storm dissipation stage. (See **Figure 3. 17**)

As the drop size (blue shape) shows, most of the large drop size are located at the higher altitude in group 2, lead to the positive vertical slope of DPMs. Few of the larger drop size occurs at the near surface at the time right after the mature stage of storm, lead to the negative

vertical slope of DPMs. (see **Figure 3. 18**)

As the shading bar shows in the conceptual model, the orange (blue) bar represents the percentage of max. acc. K_{DP} (max. acc. Z_{DR}) appears during the storm evolution. As the orange bar shows, the peak occurs at group 2, illustrate most of the storm will reach it maximum LWC before the mature stage of storm; On the contrary, the blue bar shows the peak at group 3, illustrate most of the droplet merge to a larger size after the mature stage of storm. (see **Figure 3. 19**)

3.2.2 Horizontal Separation Discussion – 5 Cases

After examining the characteristics of vertical profile of DPM cooperate with cloud microphysical process, the horizontal DPM features associated with kinematic fields will be discussed in this section. Five cases are selected for investigation of the relation of horizontal separation of DPMs to the environment wind profile. Cases are presented from weak to strong intensities. To gain more understanding of the relationship between system motion and the environmental wind field, further discussing the storm propagation, Pingtung airport sounding data were utilized. In this section, the initial time of the storm track is defined as $t = 0$; therefore, the first time-step of the storm track will be defined as $t = 1$, and so on.

Figure 3. 21, **Figure 3. 24**, **Figure 3. 27**, **Figure 3. 30** and **Figure 3. 33** show the horizontal reflectivity of the storm at the lowest level during the storm track, which do not contain any low-level blind zone of the scan strategy. The blue dot line represents the storm path, with the initial period marked as the black dot and the current storm reflectivity weighted centroid marked as the light green cross. Upper left corner in the figures display the storm properties, including storm area (A) in km^2 , storm orientation (θ) in degree, major and minor axis ($R1$ and $R2$) in km. Also, from those figures, two kinds of contour lines are shown, blue dash line and black dot line, which are the enhanced Z_{DR} and K_{DP} region on the basis of the

value greater than 75th percentile (Q3) of the data at the current level. Values of Q3 are shown at the bottom right corner. The enhance Z_{DR} region represent the area of big rain drop; On the contrary, the enhance K_{DP} region represent the area of large liquid water content. Sounding wind speed and the distance between Z_{DR} center and K_{DP} center (separation distance) in kilometer are shown at the bottom left corner of the figures. Figures with a red star symbol are the time period chosen for the further motion analysis.

Figure 3. 22, Figure 3. 25, Figure 3. 28, Figure 3. 31 and Figure 3. 34 show the enhance Z_{DR} and K_{DP} center path at different altitude. Green dash line is the storm tracking result from SMART; Blue and black solid line shows the path of the enhance Z_{DR} center and the enhance K_{DP} center at the current level.

Figure 3. 23, Figure 3. 26, Figure 3. 29, Figure 3. 32 and Figure 3. 35 show the hodograph from surface (0-kilometer height; marked as the blue 0 symbol) to 6 kilometers height (marked as the blue 6 symbol) in figures (a) and 5 vector field from figures (b) to (f), the chosen time are marked as the red star in the horizontal reflectivity figure (e.g. **Figure 3. 21**). Black arrow is the cell motion, calculated from 0 to 6 kilometers mean wind from sounding data; Red arrow is the system motion, calculated by SMART track (subtract the storm ended location by the initiated location). The storm propagation can be obtained by subtracting the system motion by cell motion (system motion – cell motion = storm propagation); Two magenta arrows are the separation vectors, pointing from the Z_{DR} center to the K_{DP} center at the current time, calculations are as follows:

$$\text{Separation Length} = \frac{4000 (m)}{V_D} \times \frac{\text{speed}}{1000} \quad (3-5)$$

$$V_{D,DR} = 8 \text{ m/s} \quad ; \quad V_{D,KD} = 6 \text{ m/s} \quad (3-6)$$

$$V_{D,DR} = 8 \text{ m/s} \quad ; \quad V_{D,KD} = 4 \text{ m/s} \quad (3-7)$$

The Separation Length in equation (3-5) is the distance between Z_{DR} center and K_{DP} center. To calculate the advection speed of the hydrometers, we hypothesis the hydrometers

falls from 4-kilometer height. Also, different terminal velocity of big and small drop size is considered in two situations. The shorter separation vector is calculated by the setting from equation (3-6). On the contrary, the longer separation vector is calculated by the setting from equation (3-7). The numerical assumptions were referenced to [Gunn and Kinzer \(1949\)](#). Light green arrow represents the wind shear between 0 to 6-kilometer height; Dark green arrow shows the storm relative wind shear. Detail descriptions are in the continuous section of each cases.

3.2.2.1 Weak Case 1 (case number 22)

The weakest storm case is selected from June 4, 2008, 0000 UTC to 0122 UTC, with 12 radar scans duration. In terms of sounding data, the closest sounding 00 UTC is selected. **Figure 3. 21** shows the horizontal reflectivity of the storm at 2-kilometer height. In this case, the storm moves from south-west to north-east, almost moves around the center of the radar.

The mean vertical DPM profiles as shown in Appendix A.10, the max. acc. Z_{HH} , max. acc. Z_{DR} and max. acc. K_{DP} appears at the same time step ($t = 10$) except max. acc. Z_{DP} ($t = 11$). Showing almost no significant time lag signal between different parameters. From the vertical slope of different parameters, vertical slope of Z_{HH} decreases to negative value after the max. acc. Z_{HH} . The storm had high reflectivity value locate at the lowest level as the storm dissipated gradually. For the vertical slope of Z_{DP} , high value locate higher than $tL + 0.5$, lead to the positive vertical slope through the entire storm track; From the time height mean Z_{DR} , the values are between 0 to 0.5 below 4-kilometers height, lead to an unstable height of the maximum Z_{DR} value, cause the irregular vertical slope distribution; From the result of K_{DP} , the maximum K_{DP} value shows practically at the level just above the $tL + 0.5$, lead to the negative vertical slopes. From the value of Z_{DR} and K_{DP} , knowing that case 22 is a shallow convective system.

With the higher DPM locate at the near surface, no transitional signal was observed.

Figure 3. 21 shows the horizontal reflectivity of the storm at 2 kilometers height, with the Z_{DR} and K_{DP} enhance region are located at the upwind side of the storm (south-west side). The separation distance of Z_{DR} and K_{DP} from 3-kilometer, 2.5-kilometer to 2-kilometer height above ground are familiar (**Figure 3. 22**), with the longest distance appears at the 4th to the 9th time step, it is corresponding to the development stage of the storm. From the hodograph in **Figure 3. 23**, the wind direction rotates clockwise with height (south to west-southwest). In case 22, the cell motion and the system motion show almost the same direction and speed, lead to a weak storm propagation (1.7 m/s). As the strength of case 22 continue to increase (from **Figure 3. 23** (b) to **Figure 3. 23** (e)), separation vector turns more perpendicular to the storm relative wind shear. In this case, the storm propagates from southwest to northeast, showing a high correlation with the separation vector. Also, due to the similarity of cell motion and system motion, storm propagation is almost zero.

3.2.2.2 Weak Case 2 (case number 20)

The second weak storm case is selected from June 3, 2008, 1945 UTC to 2052 UTC, with 10 radar scans duration. In terms of sounding data, the closest 21 UTC is selected. **Figure 3. 24** shows the horizontal reflectivity of the storm at 1-kilometer height. In this case, the storm moves from west to east, toward the location of the radar.

From Appendix A.8, a well storm life-time from developing stage to dissipating stage has been observed. With the max. acc. Z_{HH} appears first ($t = 4$), then max. acc. Z_{DP} and max. acc. K_{DP} appears after ($t = 5$), finally appears the max. acc. Z_{DR} ($t = 6$). Showing the collision-collection effect is more intensely during the dissipation stage of the storm. From the vertical slope of reflectivity, most of the height of maximum Z_{HH}

after max. acc. Z_{HH} were gradually decreasing with a negative tendency of vertical slope; As for the Z_{DR} value, height of the maximum Z_{DR} are at the high altitude before max. acc. Z_{HH} , and suddenly dropped to a lower level after the max. acc. Z_{HH} , showing the larger drop size were observed at the near surface after the time of max. acc. Z_{HH} ; Also, from the shading of mean K_{DP} , values decrease with height after the max. acc. K_{DP} , illustrate smaller rain drop started to fall, lead to a higher liquid water content at the near surface level, that may cause more heavy precipitation after the time of max. acc. K_{DP} .

From storm path shown in **Figure 3. 24**, the storm moves from the east to the west, almost the same direction of the environmental wind. Also, in most of the time, Z_{DR} center was located at the upwind side of the storm (west side) and K_{DP} center was located at the leeward side of the storm (east side). **Figure 3. 24** (d), (e), (f) are the time storm approaching to the mature stage, showing the enhance Z_{DR} and K_{DP} regions are more concentrated. From **Figure 3. 25**, the enhance K_{DP} center path do not show significant difference between 3-kilometer and 2-kilometer, with both enhance Z_{DR} and K_{DP} center path displayed more similar to the storm track at 1-kilometer height. It can be explained from the hodograph in **Figure 3. 26** (a). The wind speed is very weak from the surface to 1-kilometer height, restrict the influences of size sorting. Due to the similarity of cell motion and system motion, storm propagation is almost non-existent (0.4 m/s). In case 20, motion vectors of the storm from the mature to the dissipation stage are shown from **Figure 3. 26** (b) to (f). The direction of separation vector is more approaching to the direction of environmental wind shear. Moreover, the direction of the separation vector shows highly correlation with the high-level wind field.

3.2.2.3 Moderate Case (case number 34)

A moderate storm case is selected from June 16, 2008, 1852 UTC to 2000 UTC,

with 10 radar scans duration. In terms of sounding data, the closest 18 UTC is selected. **Figure 3. 27** shows the horizontal reflectivity of the storm at 1.5-kilometer height. In this case, the storm moves from south to north, away from the location of the radar.

From Appendix A.13, the max. acc. Z_{DR} and max. acc. Z_{DP} appears at the same time ($t = 6$), with max. acc. Z_{HH} and max. acc. K_{DP} appears 2-time steps after ($t = 8$). Illustrate more larger rain drops formed before the storm reaches its mature stage. As the solid blue line shown in **Figure 3. 27**, the storm moved from south to north, away from the location of the radar. Shading of reflectivity of the storm reached its peak at 1930 UTC to 1945 UTC, with the separation vector pointed from the south to north first and changed to west to east after, showing the same direction with the storm path (from south-north to west-east). From the enhance Z_{DR} and K_{DP} center path in different height (**Figure 3. 28**), an increment of separation distance at the same time in the lower level was observed. Limited by the radar observation, signal below 1.5-kilometer height could not be observed, therefore, longer separation distance could not be observed. From the hodograph in **Figure 3. 29** (a), wind directions in different altitude are nearly consistency, the south-southwest wind. In case 34, although the speed of cell motion and system motion shows similar, their direction are different, lead to a stronger storm propagation (4.3 m/s). From **Figure 3. 29** (b) to (e), a large orientation appears between the separation vectors and the storm relative wind shear, the direction of separation vector shows almost the same as the cell motion or the system motion. However, the direction of the separation vector changed to east-southeast before the turning point of storm track ($t = 8$), which is the same direction of the storm propagation.

3.2.2.4 Strong Case 1 (case number 29)

A strong storm case is selected from June 13, 2008, 1145 UTC to 1330 UTC,

with 15 radar scans duration. In terms of sounding data, the closest 12 UTC is selected. **Figure 3. 30** shows the horizontal reflectivity of the storm at 3 kilometers height. In this case, the storm moves from the south to the north, around the location of the radar.

From Appendix B.12, the max. acc. Z_{HH} and max. acc. K_{DP} appears at the same time ($t = 6$), with max. acc. Z_{DP} and max. acc. Z_{DR} appears 2-time steps behind ($t = 8$), the sequence is exactly opposite with case 34, but similar with case 20. Showing the collision-collection effect is more intensely during the dissipation stage of the storm. The vertical slope of both Z_{HH} and Z_{DP} shows similar pattern, with all the large value located at the high altitude, lead to the positive vertical slope for the entire evolution. As for the vertical slope of K_{DP} , it captures the variety before and after the max. acc. K_{DP} , with the positive vertical slope gradually decrease during the dissipation stage.

From **Figure 3. 30** (g) to (j) are the strongest time period of the storm, with the center of enhance Z_{DR} region identical located at the upwind side accompanied by the center of K_{DP} region at the leeward side of the storm. Due to the location of the storm, the lowest effective radar observation is around 3 kilometers height, which altitude is not low enough for size sorting. Therefore, the path of enhance Z_{DR} center and the path of enhance K_{DP} center in **Figure 3. 31** do not show any significant different between different altitudes. From the hodograph in **Figure 3. 32** (a), wind direction changed from south to southwest from low level to high level, with a slightly changed in wind speed. **Figure 3. 32** (b) to (f) are the 6th to 10th time step of the storm track, also, the time of strongest mean reflectivity. In case 29, the cell motion is much smaller than the system motion, lead to a strong propagation (13.9 m/s) pointed from the south to the north, nearly the opposite of the storm relative wind shear (north to south). As for the separation vector shown in **Figure 3. 32** (c) to (f), all of them are nearly vertical to the storm relative wind shear.

3.2.2.5 Strong Case 2 (case number 30)

The strongest storm case is selected from June 14, 2008, 0000 UTC to 0115 UTC, with 11 radar scans duration. In terms of sounding data, the closest 00 UTC is selected. **Figure 3. 33** shows the horizontal reflectivity of the storm at 1.5 kilometers height. In case 30, the storm moves from the south to the north, away from the location of the radar.

From Appendix B.13, the max. acc. Z_{DP} and max. acc. K_{DP} appears at the same time ($t = 9$) with the max. acc. Z_{HH} and max. acc. Z_{DR} appears two-time step after ($t = 11$). In case 30, SMART only capture the storm from development stage to mature stage. It is attributed to the storm merge at the next time step, cause the termination of the storm track. From the vertical slope of all parameters, including Z_{HH} , Z_{DP} , Z_{DR} and K_{DP} , the height of the maximum value increase with time, indicate the storm is still in the development stage or the mature stage. A clearly separation Z_{DR} and K_{DP} regions are reveals from **Figure 3. 33** (i) to (k), which is the strongest storm intensity within the storm track. From **Figure 3. 34** (a) to (c), the separation distance increases obviously through height. Which is the best case in this study to represent the feature of size sorting effect. From the hodograph in **Figure 3. 35** (a), wind direction changes from south-southeast to southwest, showing almost the same direction of system motion (southwest to northeast). However, due to the difference speed of cell motion and system motion, a parallel direction of storm propagation in 9.3 m/s were calculated. In **Figure 3. 35** (d) to (f), the largest orientation occurs from separation vector to storm relative wind shear, corresponds to the strongest intensity within the storm track.

To summarize the characteristics of the 5 cases, an integration table is shown in **Table**

3. 1.

1. The direction between $Z_{DR} - K_{DP}$ separation vector and the environmental mid-level wind (6 km) of all the cases shows high positive correlation except the strongest cases (case 30), which shows perpendicular direction of the vectors.
2. The relation between storm propagation speed and max. acc. Z_{HH} shows slightly positive correlation. The weaker (stronger) case with lower (higher) max. acc. Z_{HH} has slower (faster) propagation.
3. The direction between storm propagation and storm relative wind shear has no clear correlation to each other. It is postulated that additional factors (e.g., inhomogeneity of instability, surface moisture, topography, etc.) from boundary layer can also modulated the direction storm propagation.

To verify the results above, the reanalysis dataset was utilized for statistical analysis of the 38 cases. The results are shown in the next section.

3.3 Statistical Performance of Motion Vectors

Due to the lack of sounding data, cases for calculating cell motion are limited. The reanalysis data, namely the ERA-Interim dataset, were applied to replace sounding data. All of the 38 cases thus can be included to the further analysis. As discussed in [Loeffler and Kumjian \(2018\)](#), the separation vector pointing from K_{DP} center to Z_{DR} center tends to be more orthogonal when the nonsupercell tornado occurs. The result can allow forecasters to use polarimetric radar measurements to gain a better prediction. Base on the idea, this study intends to find the relationship between DPM separation and the environment wind field.

Figure 3. 36 shows the relation between max. acc. Z_{HH} and storm propagation of each storm. The storm propagation at the y-axis is calculated by cell motion from reanalysis data and system motion from the SMART. The value of correlation coefficient is shown at the upper left

corner ($r = 0.1881$), illustrate the strength of the storm is not well correlated with the speed of propagation. The storms are further classified into two groups, namely weak and strong storms, for further investigation.

Figure 3. 37 shows the statistical results of different motion vectors. **Figure 3. 37 (a)** is the cell motion, calculated by reanalysis dataset; It shows that there is no significant difference in environmental wind speed between weak and strong storms. Due to the similarity of the reanalysis dataset between weak and strong cases, the storm propagation will only be determined by the following two factors:

1. Speed of system motion.
2. Orientation between cell motion and system motion.

Figure 3. 37 (b) shows the system motion, calculated by storm tracking result from SMART; It shows that the storms with faster speed are strong cases, indicating that the strong storm shows high probability in faster moving speed. In addition, the system motions of strong cases have more variability than weak cases. Yet, the mean system motions are similar.

The storm propagation as shown in **Figure 3. 37 (c)** larger variability occurs at strong case as well. Nevertheless, the result shows that slightly faster propagation speed in strong cases than in weak cases. High similarity in of both system motion and storm propagation, demonstrate other factors need to be consider to investigate any regularity feature in Taiwan.

Chapter 4 Conclusions and Future Works

4.1 Conclusions

In this research, the entire SoWMEX/TiMREX dual-polarimetric radar data and sounding data were utilized. Based on [Dixon and Wiener \(1993\)](#) storm identification and tracking algorithms, Storm Motion Analysis by Radar Tracking (SMART) is proposed. By giving the reflectivity threshold, area threshold and speed threshold, storm analysis in Lagrangian description can be accomplished. A duration threshold and area threshold within the storm track were applied to preserve single convective storms. Finally, 38 cases were select to study the statistical characteristics of single cell storms and five of them for detailed discussion.

The results are divided into three parts, (A) statistical characteristics, (B) detailed description of horizontal separation and (C) the statistical performance of motion vectors. The results are as below:

A. Statistical Characteristics of 38 Cases

1. A decrease signal can be seen in the distribution of maximum value of all dual-polarization parameters (Z_{HH} , Z_{DP} , Z_{DR} and K_{DP}) divided by the time of maximum accumulative reflectivity. Illustrate the strength of storms do decline after the max. acc. Z_{HH} . (see **Figure 3. 16**)
2. Only the distribution of vertical slope of Z_{DR} appears the decrease signal after the maximum accumulative reflectivity time. Illustrate larger hydrometers shows more pronounced feature of falling behavior from radar data. (see **Figure 3. 16**)

3. After divided the values of vertical slope of DPM into 4 groups, most of the vertical slopes are located at the positive region. This is attributed to the height of the maximum value seldom locates just above the highest low-level bind zone. (see **Figure 3. 18**)
4. Among all the parameters, the tendency of Z_{DR} vertical slope shows pronounced negative value in group3. Illustrating larger size of drop does fall earlier than smaller size of drop. (see **Figure 3. 18**)
5. From all the parameters, the 50th percentile of tendency of maximum value shows the most positive value in group2, and then make a sharp decrease to negative value in group3. Illustrating the strength of most of the storms changed significantly within 30-minutes before and after the max. acc. Z_{HH} . (see **Figure 3. 17**)
6. There is a time lag between maximum accumulative Z_{DR} and K_{DP} relative to max. acc. Z_{HH} in strong cases. The peak acc. K_{DP} appears first before acc. Z_{DR} peak. This feature may potentially identify the transition of mature to dissipate stage of the storm. (see **Figure 3. 19**)

B. Horizontal Separation of 5 Cases

1. The storm propagation seems to increase from weak cases to strong cases. Attributed to the similarity of both speed and direction between cell motion and system motion.
2. In stronger cases, longer time leg between max. acc. Z_{DR} and max. acc. K_{DP} will appears (two-time step difference). While weak cases only show one-time step or non-time step difference.
3. The direction of Z_{DR} and K_{DP} separation shows a high correlation with the direction of environmental mid-level wind (6 km). Indicate without the

sounding data, mid-level wind direction can be extrapolate by the direction of separation vector.

4. The behavior of storm propagation and the storm relative wind shear showing an inconsistent characteristic in different cases. Illustrating more atmospheric boundary conditions need to be considered (e.g. atmospheric stability).

C. Statistical Performance of Motion Vectors

1. A low correlation coefficient between storm max. acc. Z_{HH} and storm propagation illustrate the strength of storm is not the main reason of the speed of propagation. Explaining other factors need to be consider to study storm propagation. (see **Figure 3. 36**)
2. Under the premise of similar cell motion, both speed and direction of system motion is the key to determining the magnitude of storm propagation.

4.2 Future Works

In this research, a preliminary investigation of the microphysics characteristics in both horizontal and vertical terms of storms were revealed. By investigating the various characteristics of structural evolutions, dynamic, microphysics processes, the results had shown the potential of diagnosing the storm development by utilizing dual-polarimetric parameters.

Future works aim for both SMART and storm analysis are as follows:

1. Storm split and merge need to be considered in the tracking algorithm of SMART.
2. Develop a 3-Dimensional tracking algorithm of single radar of SMART.
3. To verify the results, more single cell cases with complete life duration need to be applied.
4. To study storm propagation, atmospheric conditions need to be considered.
5. To study more detail convective storm in Taiwan, thermodynamic and topography need to be considered.

References

- 汪志偉，2009：「利用剖風儀與二維雨滴譜儀對西南氣流實驗SoWMEX/TiMREX不同降水系統的觀測研究」。國立中央大學碩士論文，122頁。
- 邱思翰，2010：「利用WRF模式研究SoWMEX IOP3期間地形效應對於強降水個案之影響」。國立中央大學碩士論文，96頁。
- 吳冠伯，2019：「2005-2015年暖季弱綜觀環境下對流降水系統之特徵統計」。中國文化大學碩士論文，87頁。
- 邵彥銘，2015：「利用局地系集轉換卡爾曼濾波器雷達資料同化系統改善短期定量降水預報：SoWMEX IOP8 個案分析」。國立中央大學碩士論文，95頁。
- 洪晨語，2020：「雙偏極化雷達參數變分法定量降水估計評估：五分山S波段與C波段」。國立中央大學碩士論文，66頁。
- 陳奕如，2009：「SoWMEX實驗期間雨滴粒徑分佈特性之研究」。國立中央大學碩士論文，99頁。
- 陳新淦、黃椿喜、呂國臣、洪景山及張博雄，2016：「利用雷達回波影像辨識及篩選技術發展極短期系集定量降水預報」。大氣科學，44，No. 1，1-31。
- 陳尉豪，2011：「同化多都普勒雷達資料以提升降水預報能力之研究-2008 SoWMEX IOP8 個案分析」。國立中央大學碩士論文，96頁。
- 陳立昕，2017：「利用系及估計與檢驗對流尺度之預報誤差：SoWMEX IOP8 個案分析」。國立中央大學碩士論文，91頁。
- 陳勁宏，2018：「不同微物理方案在雲可解析模式的系集預報分析：SoWMEX IOP8 個案」。國立中央大學碩士論文，99頁。
- 梁晏彰，2019：「分析不同微物理參數化之系及預報誤差：SoWMEX-IOP8 對流個案」。國立中央大學碩士論文，110頁。

- 童崇祺，2009：「西南氣流實驗期間之降水特徵與相關環境型態」。國立台灣大學碩士論文，90頁。
- 廖浩彥，2014：「利用雷達觀測直接反演氣象變數進行資料同化以改進短期定量降水預報-2008 SoWMEX IOP8 個案分析」。國立中央大學碩士論文，104 頁。
- 鄭翔文，2017：「雷達資料同化於多重尺度天氣系統(梅雨)的強降雨預報影響：SoWMEX IOP#8 個案研究」。國立中央大學碩士論文，80 頁。
- 錢伊筠，2010：「WRF 模式 Double-moment 雲微物理參數化法對於 SoWMEX IOP-4 個案降水模擬之敏感度研究」，國立中央大學碩士論文，130 頁。
- 盧可昕，2018：「利用雙偏極化雷達及雨滴譜儀觀測資料分析 2008 年西南氣流期間強降雨事件的雲物理過程」，國立中央大學碩士論文，91 頁。
- 蔡直謙，2009：「SoWMEX/TiMREX 個案中雨滴粒徑分佈之收支分析」。國立中央大學碩士論文，71 頁。
- Dixon, M., and G. Wiener, 1993: TITAN: Thunderstorm Identification, Tracking, Analysis, and Nowcasting — a radar-based methodology. *J. Atmos. Oceanic Technol.*, **10**, 785-797.
- Fridlind, A. M., and Coauthors, 2019: Use of polarimetric radar measurements to constrain simulated convective cell evolution: a pilot study with Lagrangian tracking. *Atmos. Meas. Tech.*, **12**, 2979-3000.
- Gunn, R. and G. D. Kinzer, 1949: The terminal velocity of fall water droplets in stagnant air. *J. Meteor.*, **6**, 243-248.
- Homeyer, C. R., T. N. Sandmæl, C. K. Potvin, and A. M. Murphy, 2020: Distinguishing characteristics of tornadic and nontornadic supercell storms from composite mean analyses of radar observations. *Mon. Wea. Rev.*, **148**, 5015-5040.
- Hu, M-K, 1962: Visual pattern recognition by moment invariants. *IRE Transactions on Information Theory*, **8**, 179-187.

- Hu, J., D. Rosenfeld, D. Zrníc, E. Williams, P. Zhang, J. C. Snyder, A. Ryzhkov, E. Hashimshoni, R. Zhang, and R. Weitz, 2019: Tracking and characterization of convective cells through their maturation into stratiform storm elements using polarimetric radar and lightning detection. *Atmos. Res.*, **226**, 192-207.
- Johnson, J. T., P. L. MacKeen, A. Witt, E. D. W. Mitchell, G. J. Stumpf, M. D. Eilts, and K. W. Thomas, 1998: The storm cell identification and tracking algorithm: An enhanced WSR-88D algorithm. *Wea. Forecasting*, **13**, 263-276.
- Kumjian, M. R., 2013: Principles and applications of dual-polarization weather radar. Part I: Description of the polarimetric radar variables. *J. Operat. Meteor.*, **1**, 226-242.
- Li, L., W. Schmid, and J. Joss, 1995. Nowcasting of motion and growth of precipitation with radar over a complex orography. *J. Appl. Meteor.*, **34**, 1286-1300.
- Loeffler, S. D., and M. R. Kumjian, 2018: Quantifying the separation of enhanced ZDR and KDP regions in nonsupercell tornadic storms. *Wea. Forecasting*, **33**, 1143-1157.
- Loeffler, S. D., M. R. Kumjian, M. Jurewicz, and M. M. French, 2020: Differentiating between tornadic and nontornadic supercells using polarimetric radar signatures of hydrometeor size sorting. *Geophysical Research Letters*, **47**, e2020GL088242.
- Rinehart, R. E., and E. T. Garvey, 1978: Three-dimensional storm motion detection by conventional weather radar. *Nature*, **273**, 287-289.
- Ryzhkov, A. V., and M. R. Kumjian, 2009: Storm-relative helicity revealed from polarimetric radar measurements. *J. Atmos. Sci.*, **66**, 667-685.
- Seliga, T. A., and V. N. Bringi, 1976: Potential use of radar differential reflectivity measurements at orthogonal polarizations for measuring precipitation. *J. Appl. Meteor.*, **15**, 69-76.
- Steiner, M., R. Houze, and S. Yuter, 1995: Climatological characterization of three-dimensional storm structure from operational radar and rain gauge data. *J. Appl. Meteor.*, **34**, 1978-2007.

- Tong, H., V. Chandrasekar, K. Knupp, and J. R. Stalker 1998: Multiparameter radar observations of time evolution of convective storms: Evaluation of water budgets and latent heating rates, *J. Atmos. Oceanic Technol.*, **15(5)**, 1097-1109.
- Vila, D. A., L. A. T. Machado, H. Laurent, and I. Velasco, 2008: Forecast and Tracking the evolution of Cloud Clusters (ForTraCC) using satellite infrared imagery: Methodology and validation. *Wea. Forecasting*, **23**, 233-245.
- Wapler, K., 2021: Mesocyclonic and non-mesocyclonic convective storms in Germany: Storm characteristics and life-cycle. *Atmos. Res.*, **248**.
- Yang, Y., X. Chen, and Y. Qi, 2013: Classification of convective/stratiform echoes in radar reflectivity observations using a fuzzy logic algorithm. *J. Geophys. Res.: Atmos.*, **118**, 1896-1905.
- Yuter S. E., and R. A. Houze Jr., 1995: Three-dimensional kinematic and microphysical evolution of Florida cumulonimbus. Part II : Frequency distributions of vertical velocity, reflectivity, and differential reflectivity. *Mon. Wea. Rev.*, **123**, 1941-1963.

Tables

Table 1.1 List of 47 cases

Month	date	Start time	End time	Case #	Storm id	IOP #
05	19	2115	2252	1	06	1
	20	1254	1437	2	05	1
	21	0422	0552	3	08	1
	22	0345	0507	4	10	none
	22	0415	0522	5	22	none
	22	0540	0645	6	24	none
	22	2122	2307	7	05	none
	26	0609	0722	8	01	none
	28	2115	2237	9	37	2
	28	2215	2352	10	12	2
	29	1837	2037	11	07	2
	30	0515	0622	12	01	3
	30	1545	1700	13	08	3
06	01	1552	1730	14	02	none
	02	0624	0807	15	15	4
	03	0915	1037	16	04	4
	03	0915	1100	17	05	4
	03	1845	2022	18	04	5
	03	1845	2052	19	09	5
	03	1945	2052	20	18	5
	03	2152	2307	21	11	5
	04	0000	0122	22	16	5
	08	0837	1015	23	04	none

Month	date	Start time	End time	Case #	Storm id	IOP #
06	09	0552	0707	24	01	none
	09	0737	0900	25	03	none
	11	0700	0822	26	02	none
	11	0930	1215	27	04	none
	11	2152	2352	28	06	none
	13	1145	1330	29	01	7
	14	0000	0115	30	15	8
	15	1345	1530	31	03	8
	16	1322	1445	32	03	8
	16	1522	1600	33	08	8
	16	1852	2000	34	04	8
	17	0745	0907	35	07	8
	17	0800	0907	36	08	8
	17	0807	0922	37	11	8
	18	0252	0407	38	03	none
	18	2052	2300	39	07	none
	26	0352	0515	40	20	9
	26	1937	2115	41	25	none
	27	0622	0737	42	37	none
	27	1600	1722	43	03	none
	28	0231	0246	44	01	none
	28	0822	0930	45	24	none
	28	0852	1000	46	06	none
	28	0945	1100	47	30	none

Table 3.1 Integration table of storm motions of 5 cases.

		Weak		Moderate	Strong	
		Case 22	Case 20	Case 34	Case 29	Case 30
Direction	$Z_{DR} - K_{DP}$ Separation					
	Environmental mid-level wind (6km)					
Strength	Storm propagation (m/s)	1.7	0.4	4.3	13.9	9.3
	Max. Acc. Z_{HH} (dBZ)	369.69	490.84	424.12	600.90	731.94
Direction	Storm propagation					
	Storm relative wind shear					

Figures

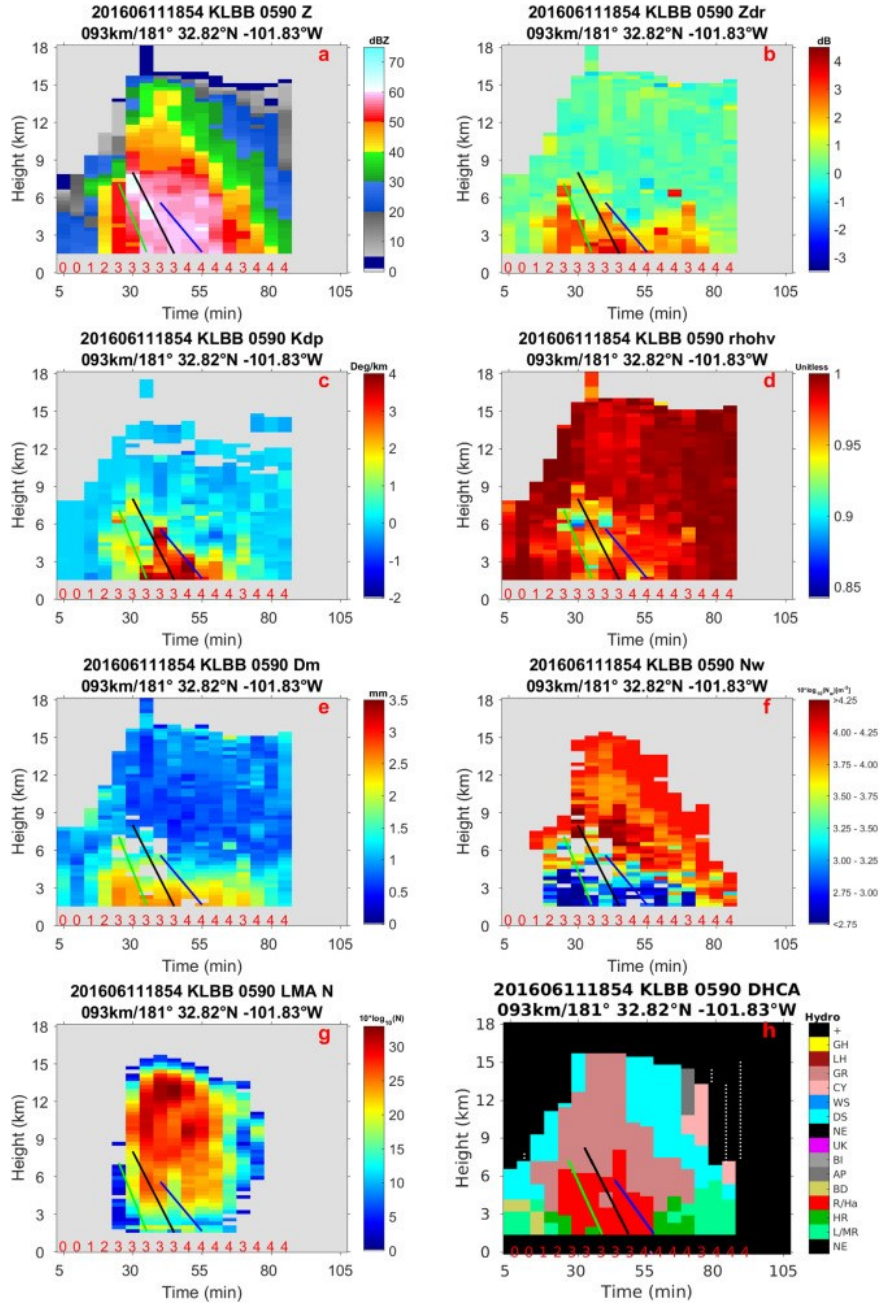


Figure 1. 1 The time-height properties of cell 590 are shown here. **Figure 1. 1** a-h show the time-height evolution of Z , Z_{DR} , K_{DP} , ρ_{hv} , D_m , N_w , LMA_CC and DHCA. For **Figure 1. 1** a-f, each grid box represents the magnitude of the variables at the same location of maximum Z of each time-height dimension for this cell. **Figure 1. 1** g shows the integrated VHF lightning sources for this cell at each time-height dimension. **Figure 1. 1** h shows hydrometeor classifications. Each panel title includes the specific UTC time of the cell shown in the figure when the cell is first detected. For instance, 201,606,111,854 means 18:54, June 11, 2016 and 093 km/181° 32.82°N -101.83°W means this cell is first detected 93 km away from the KLBB radar with an azimuth angle of 181° located at 32.82°N -101.83°W.(Adopted from [Hu et al. 2019](#))

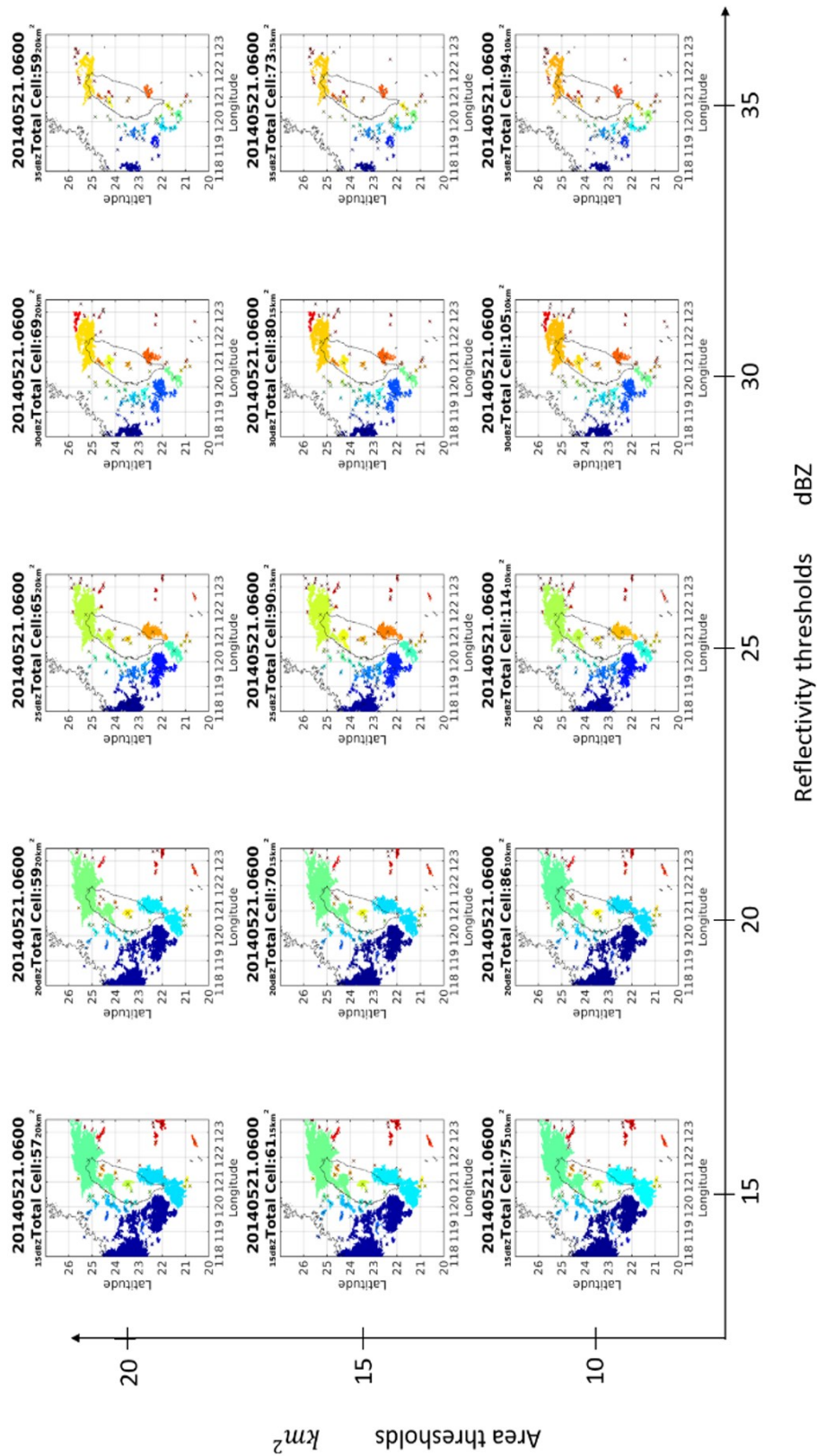


Figure 2.3 A sensitivity test of both reflectivity thresholds and area thresholds in May 21th, 2014 from CWB QPESUMES data. Color shaded represent each storm area. 'x' is the reflectivity weighted centroid of each storm.

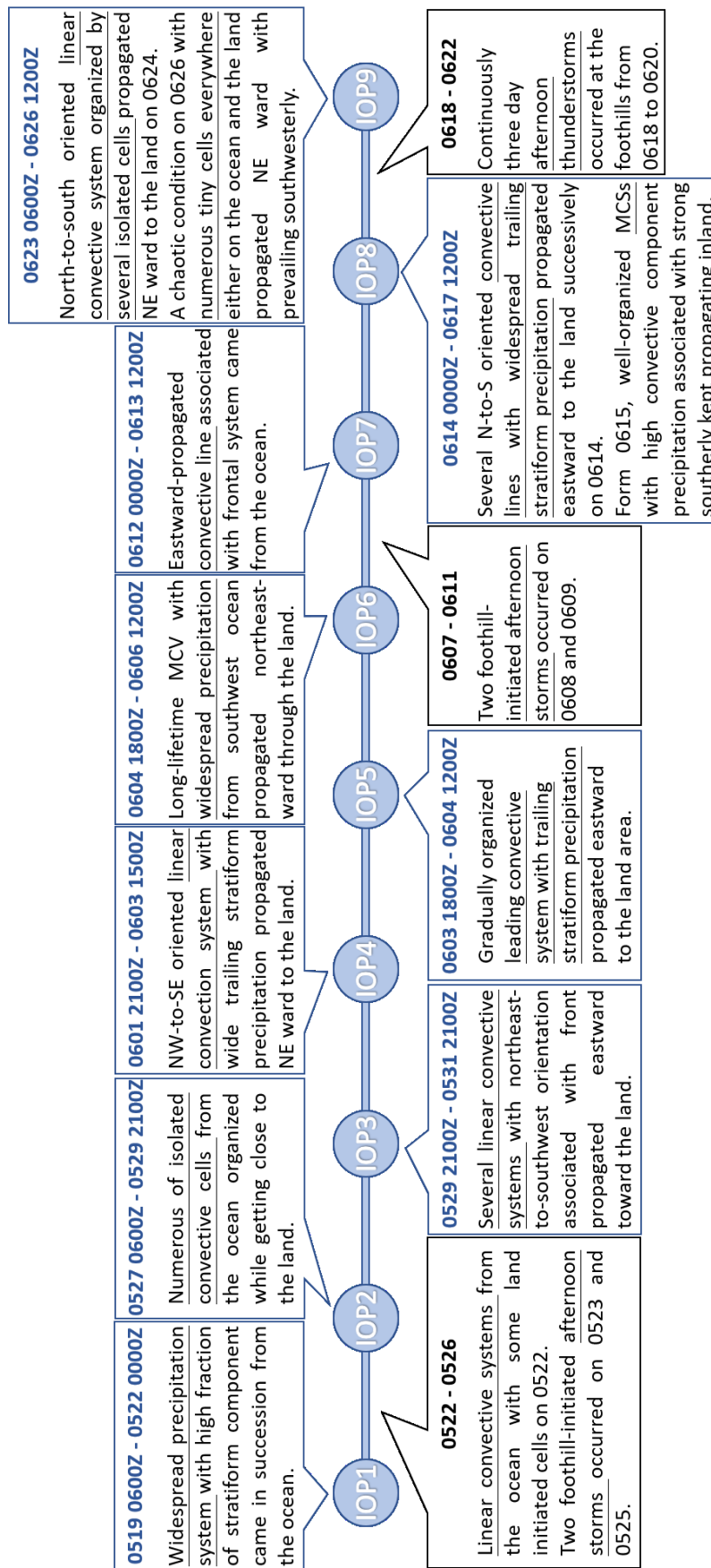


Figure 3. 1 Time chart of IOPs and the corresponding weather conditions during SoWMEX.

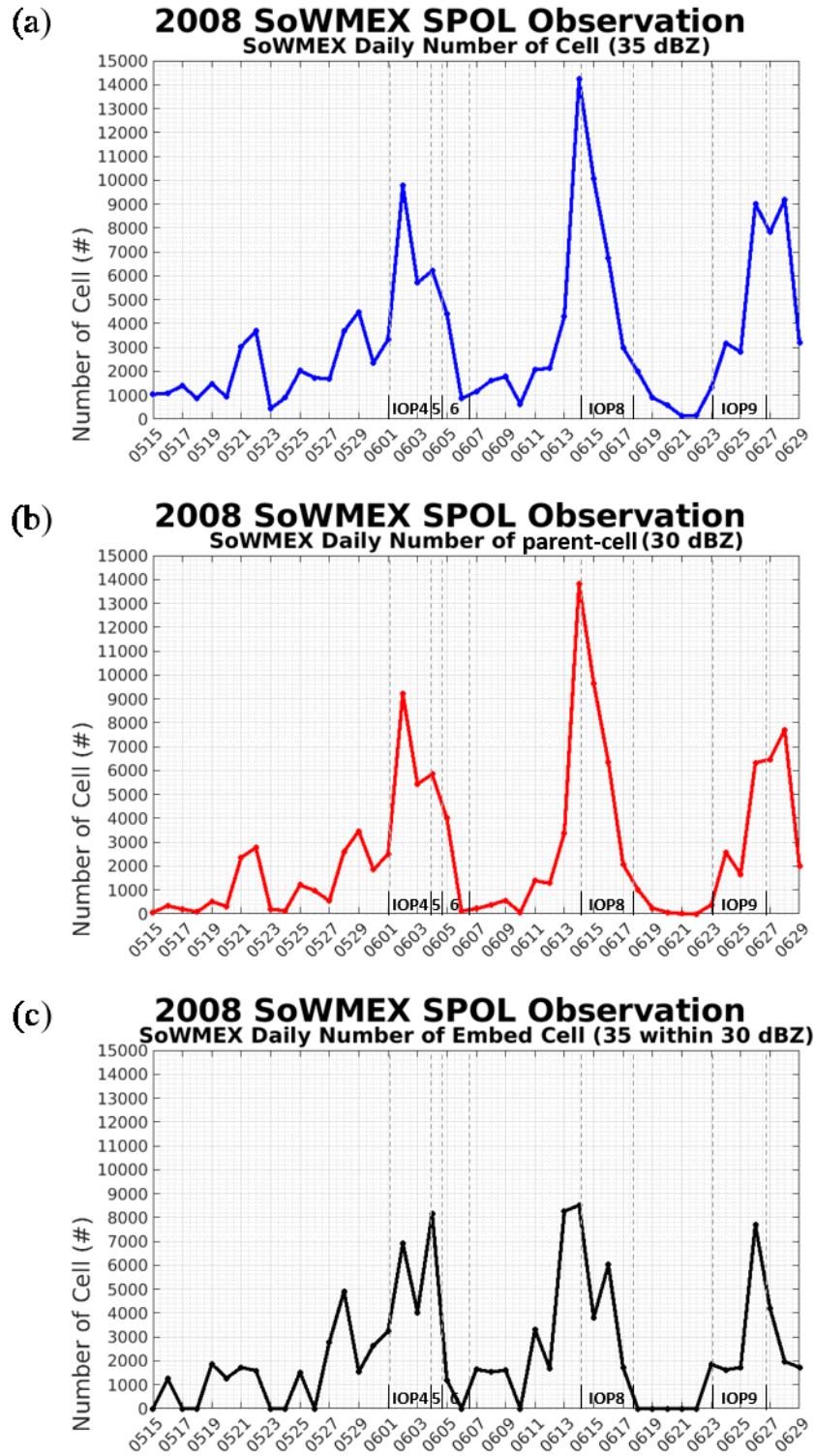


Figure 3. 2 Daily cell number during SoWMEX in different storm types. (a) parent-cell (b) child-cell (c) cell-embed.

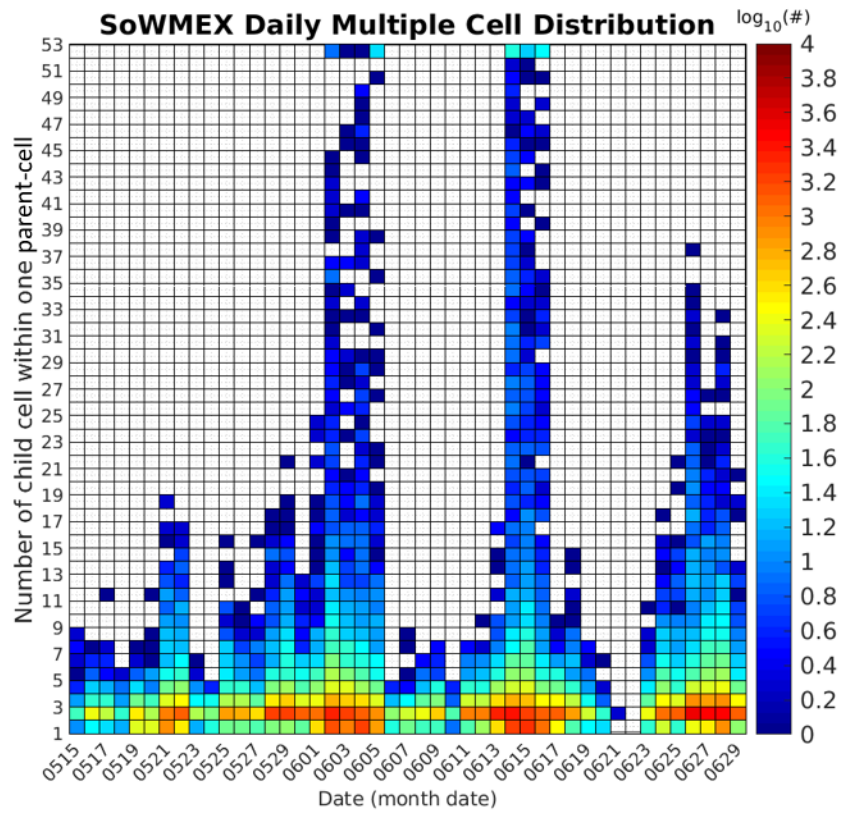


Figure 3.3 Daily multiple cell distribution, numbers in log₁₀ scale.

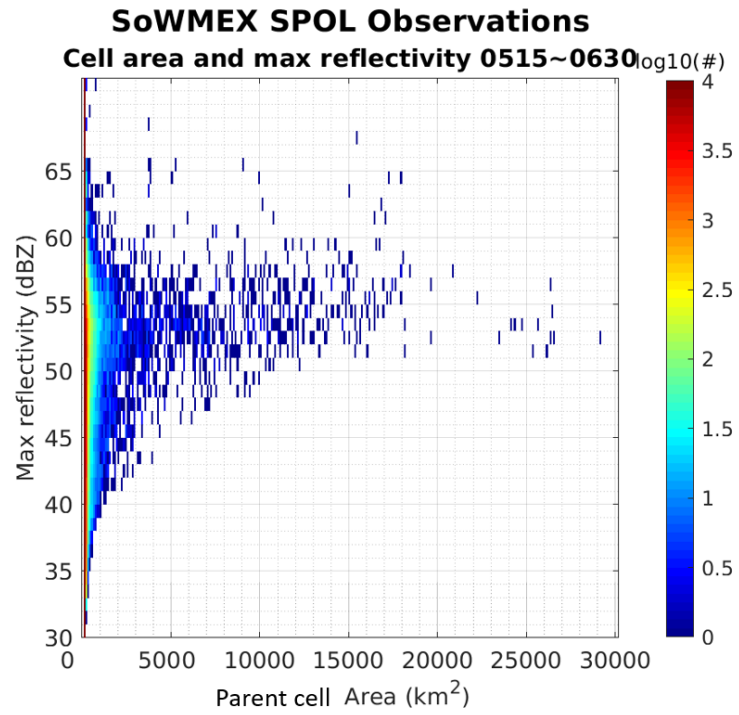


Figure 3.4 Parent-cell area relative to cell max reflectivity.

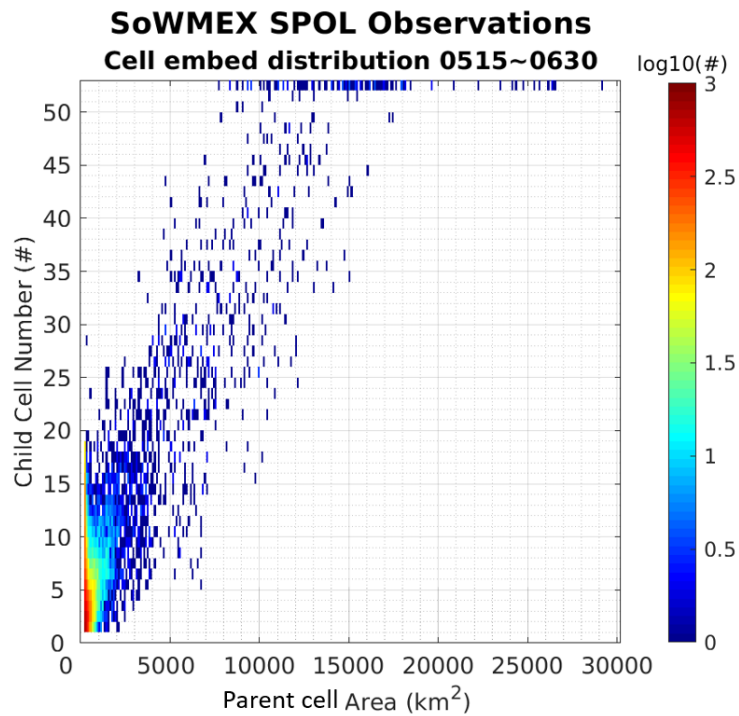


Figure 3.5 Parent-cell area relative to child-cell number embed.

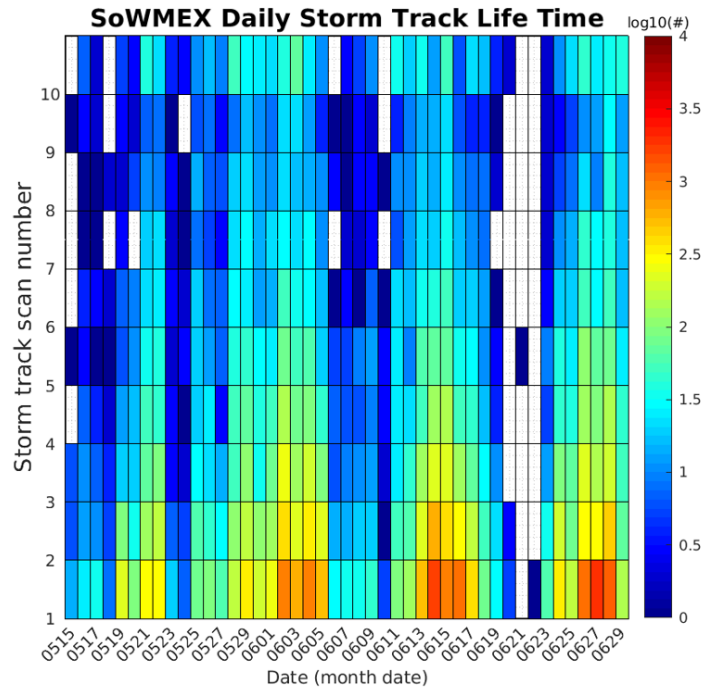


Figure 3. 6 Distribution of daily storm track life time.

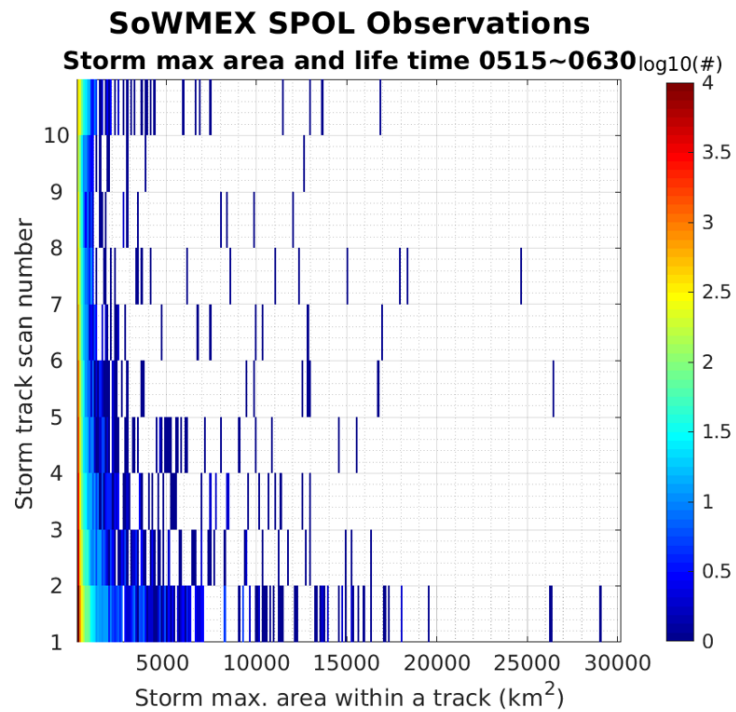


Figure 3. 7 Storm maximum area relative to storm life time.

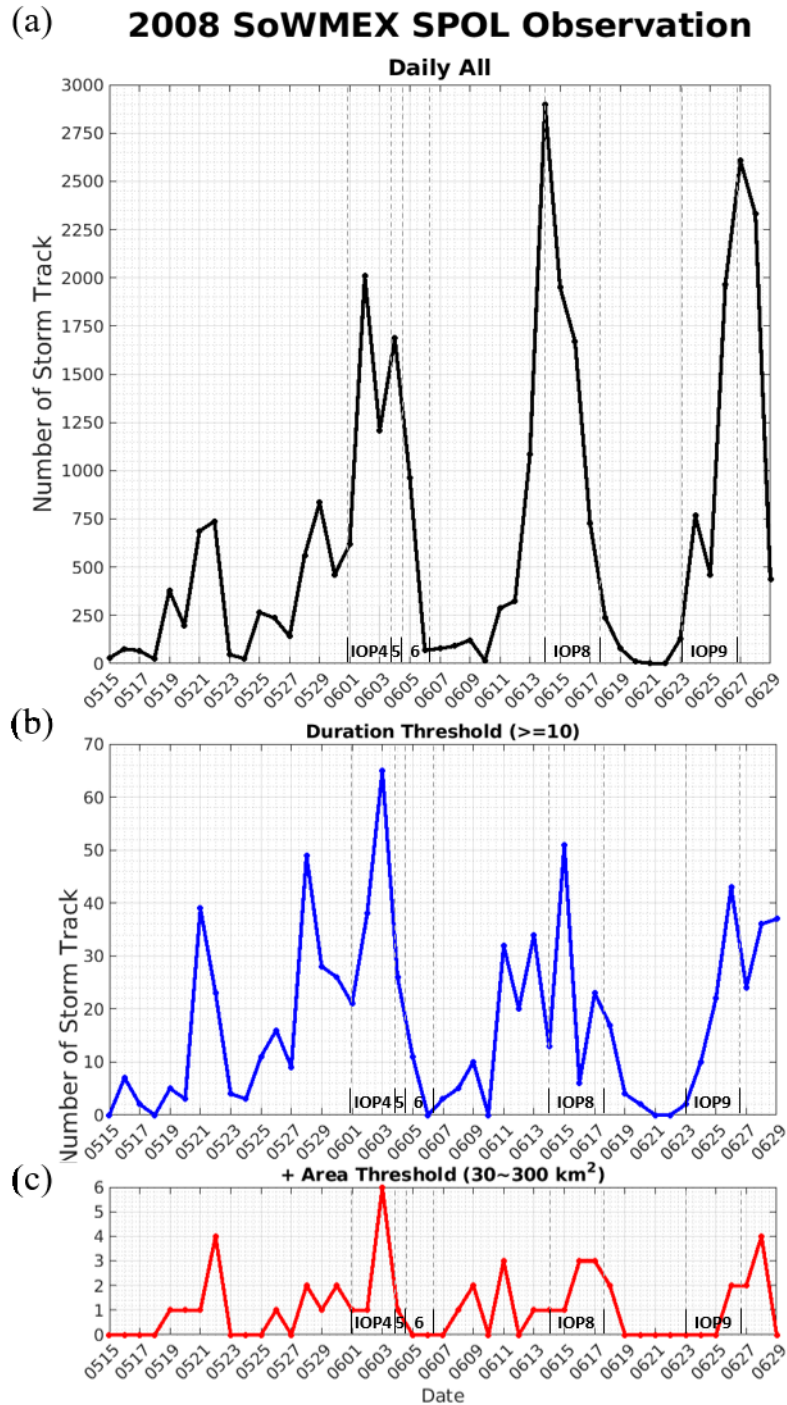


Figure 3.8 2008 SoWMEX daily storm track distributions. (a) Daily number of storm track with 30 dBZ reflectivity threshold. (b) Daily number of storm track with 30 dBZ reflectivity threshold and duration threshold. (c) Daily number of storm track with 30 dBZ reflectivity threshold, duration threshold and area threshold.

SoWMEX SPOL 47 Cases Track Path

Duration : ≥ 10 (scan) Area : 30~300 (km²)

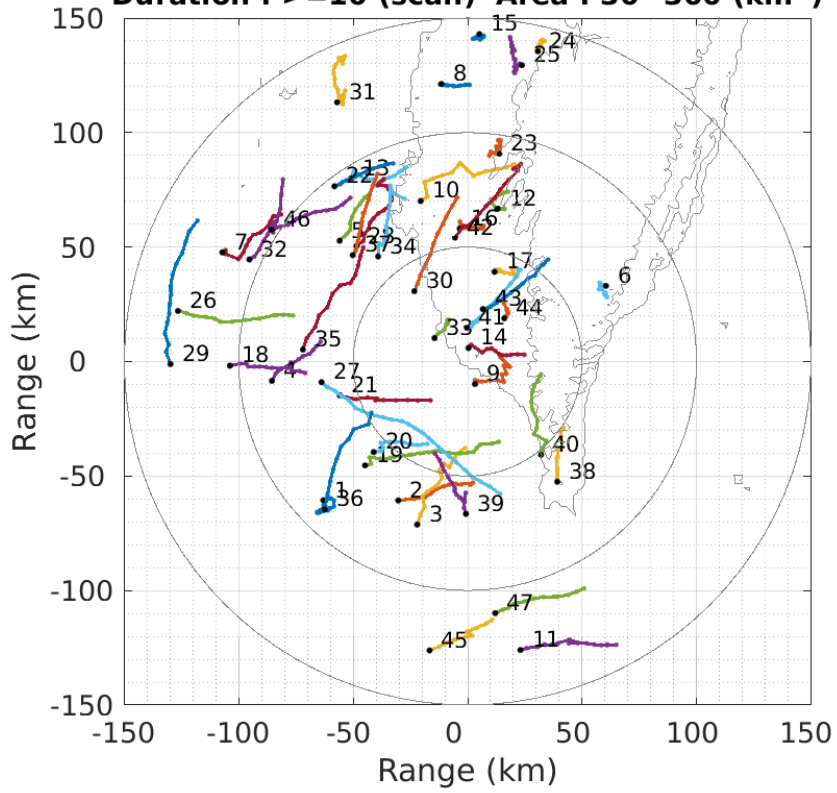


Figure 3. 9 Storm track path of 47 cases. Numbers by the storm path are the case number.

Detail descriptions of each storm are mention in **Table 1. 1**.

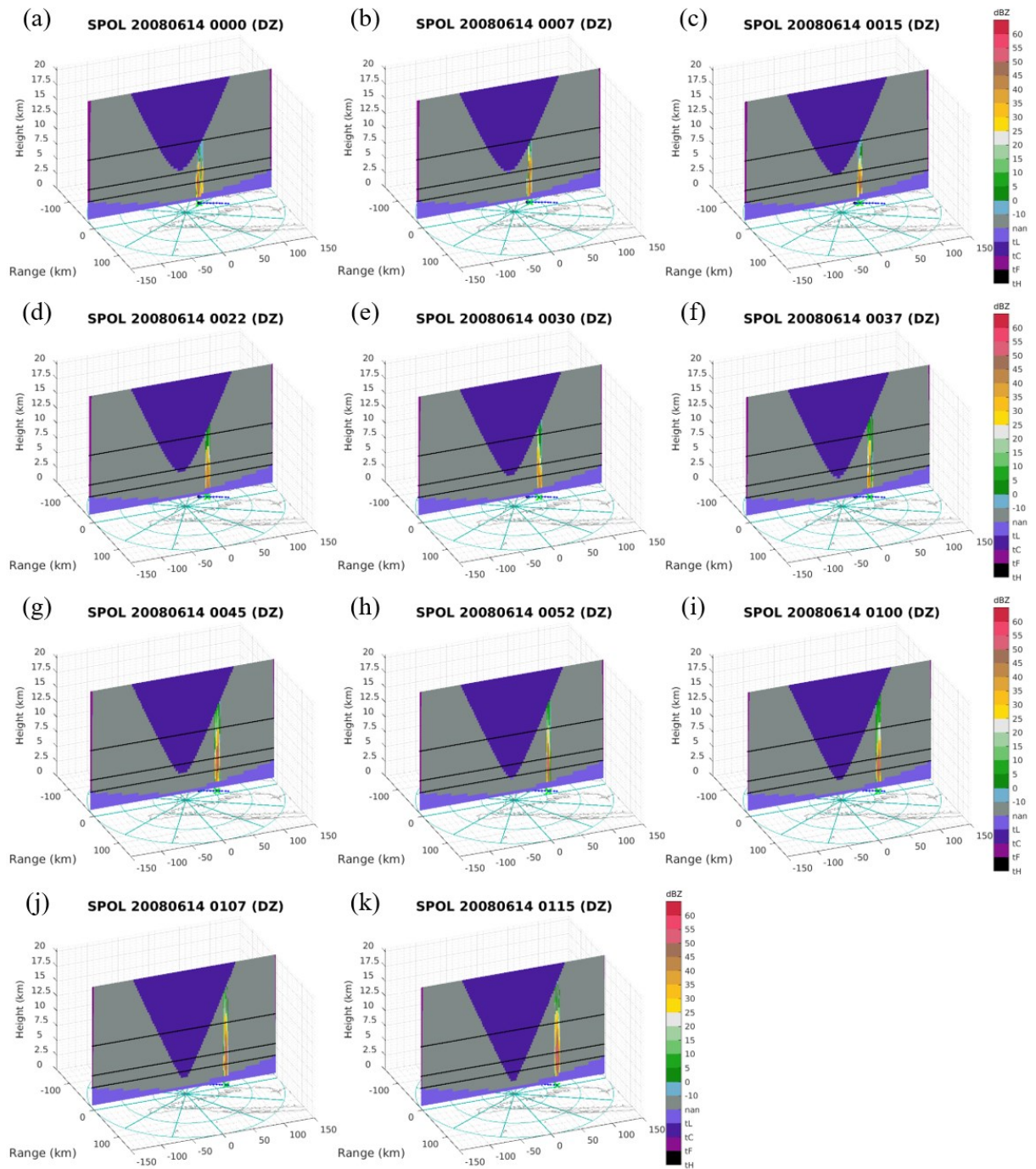


Figure 3.10 Vertical section from the reflectivity weighted center along the x direction of case 30. From (a) to (k) are the different time period of the storm track.

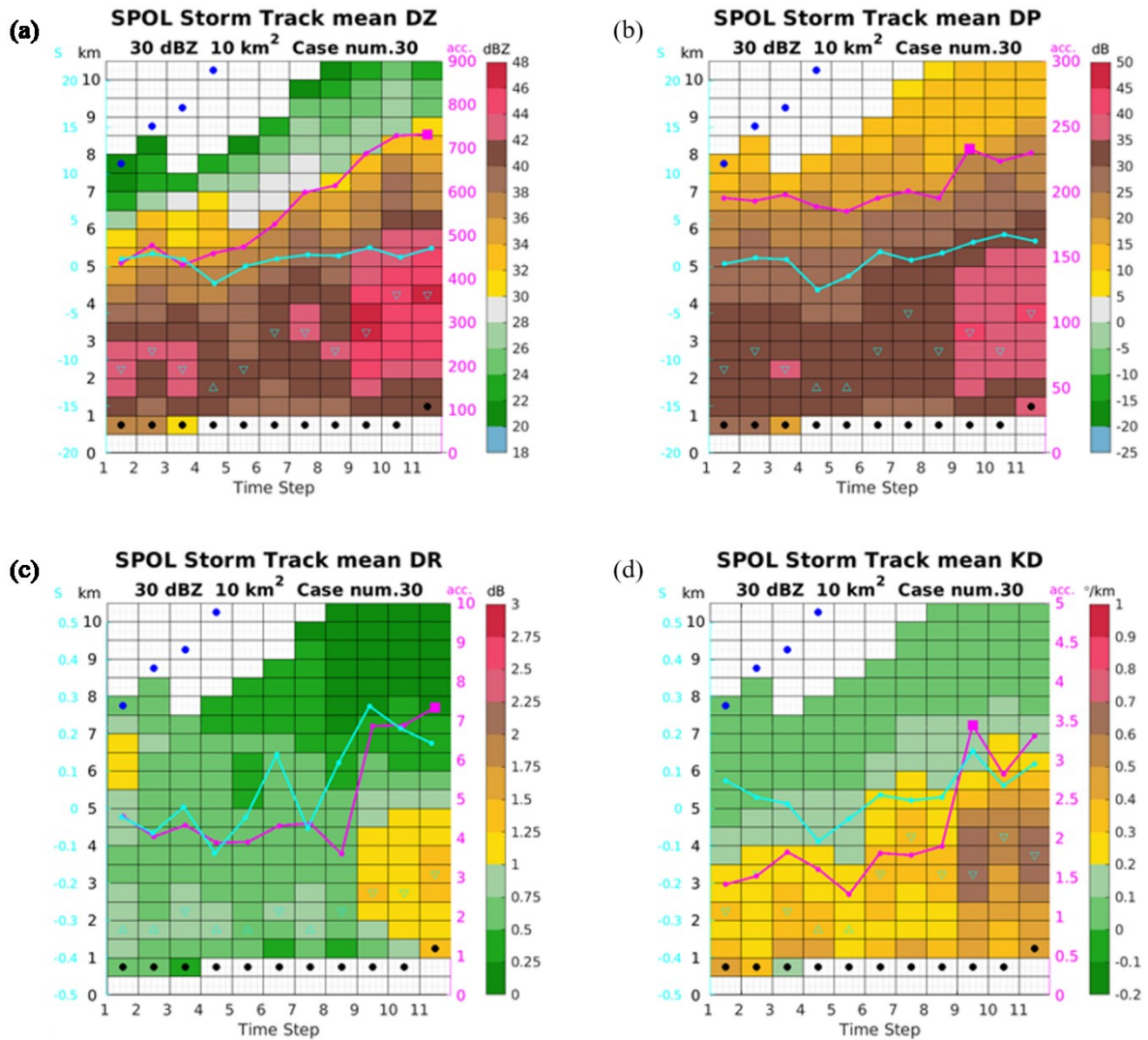


Figure 3. 11 Time series of mean dual-polarimetric parameters with height. An example of developing storm. (a) Z_{HH} (b) Z_{DP} (c) Z_{DR} (d) K_{DP} , shading is the mean value respectively. Height below the black dots represent the blind zone below the lowest elevation and height above the blue dots represents the blind zone above the maximum elevation at each time step. Accumulative values are shown as the pink lines, pink squares are the maximum accumulative time; The calculated vertical slope are shown as the light blue line, with the maximum dual-polarimetric value marked as the hollow triangle.

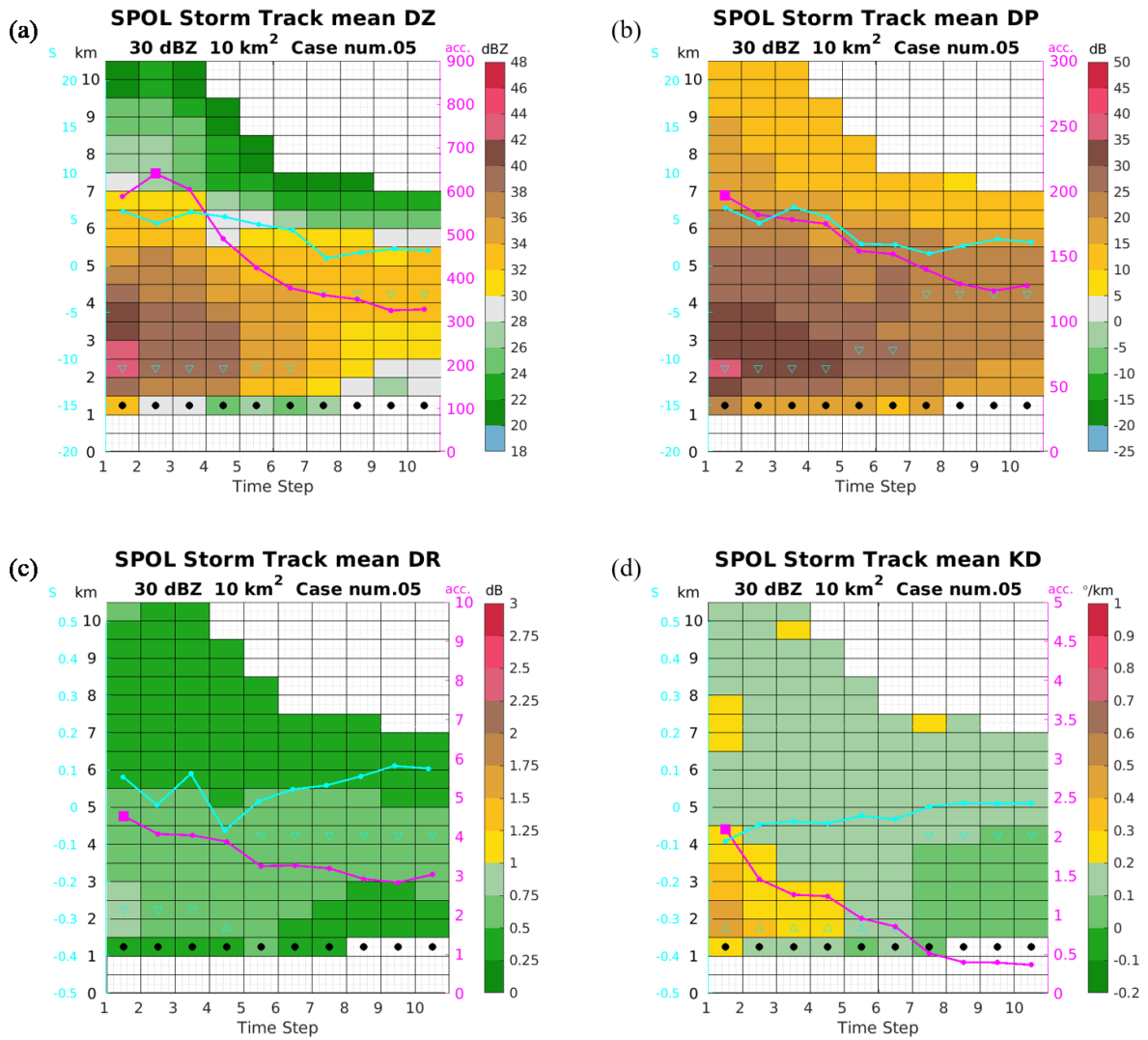


Figure 3.12 Same as Figure 3.11, but for an example of dissipation storm.

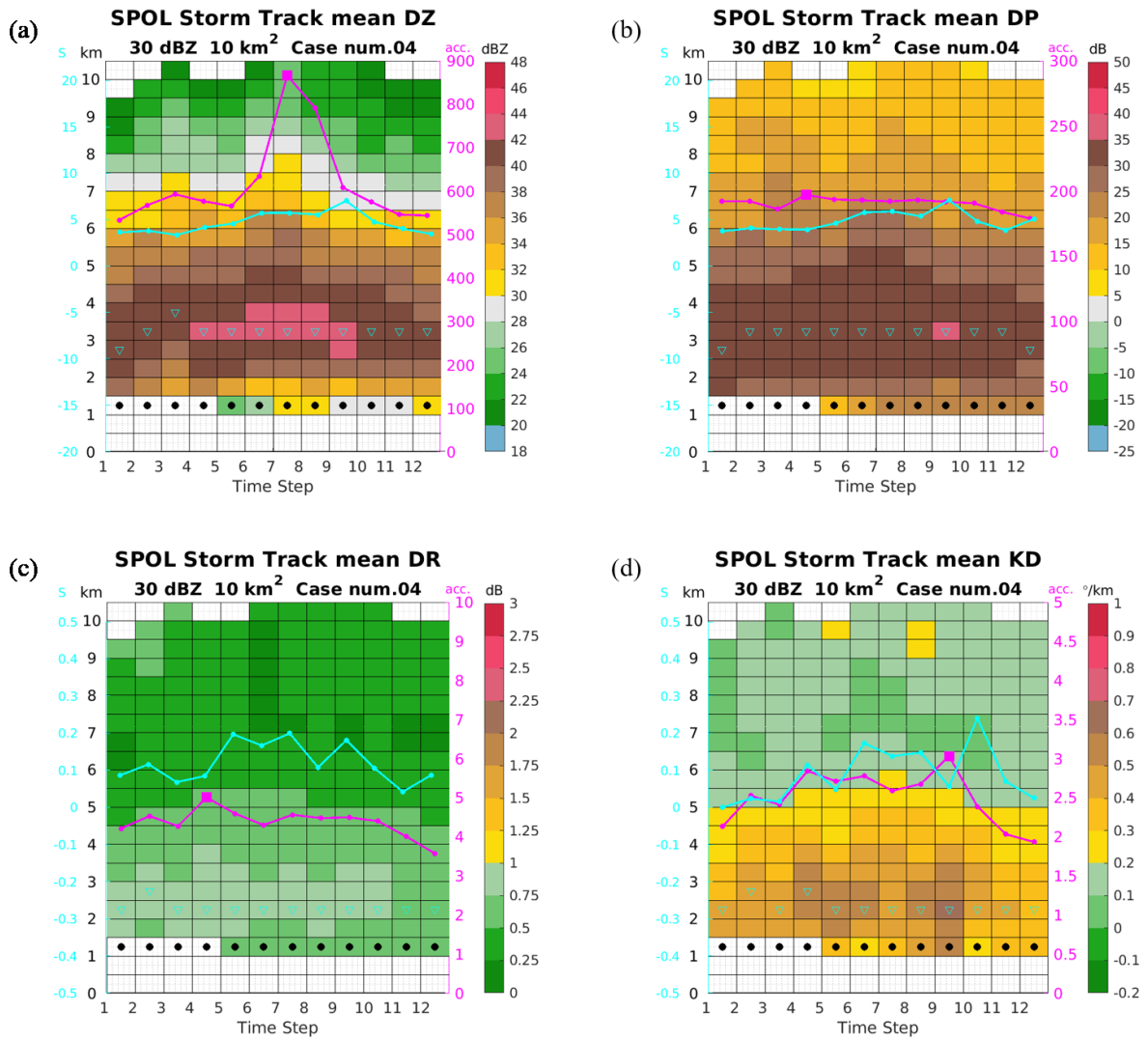


Figure 3.13 Same as **Figure 3.11**, but for an example of storm from developing stage to dissipation stage.

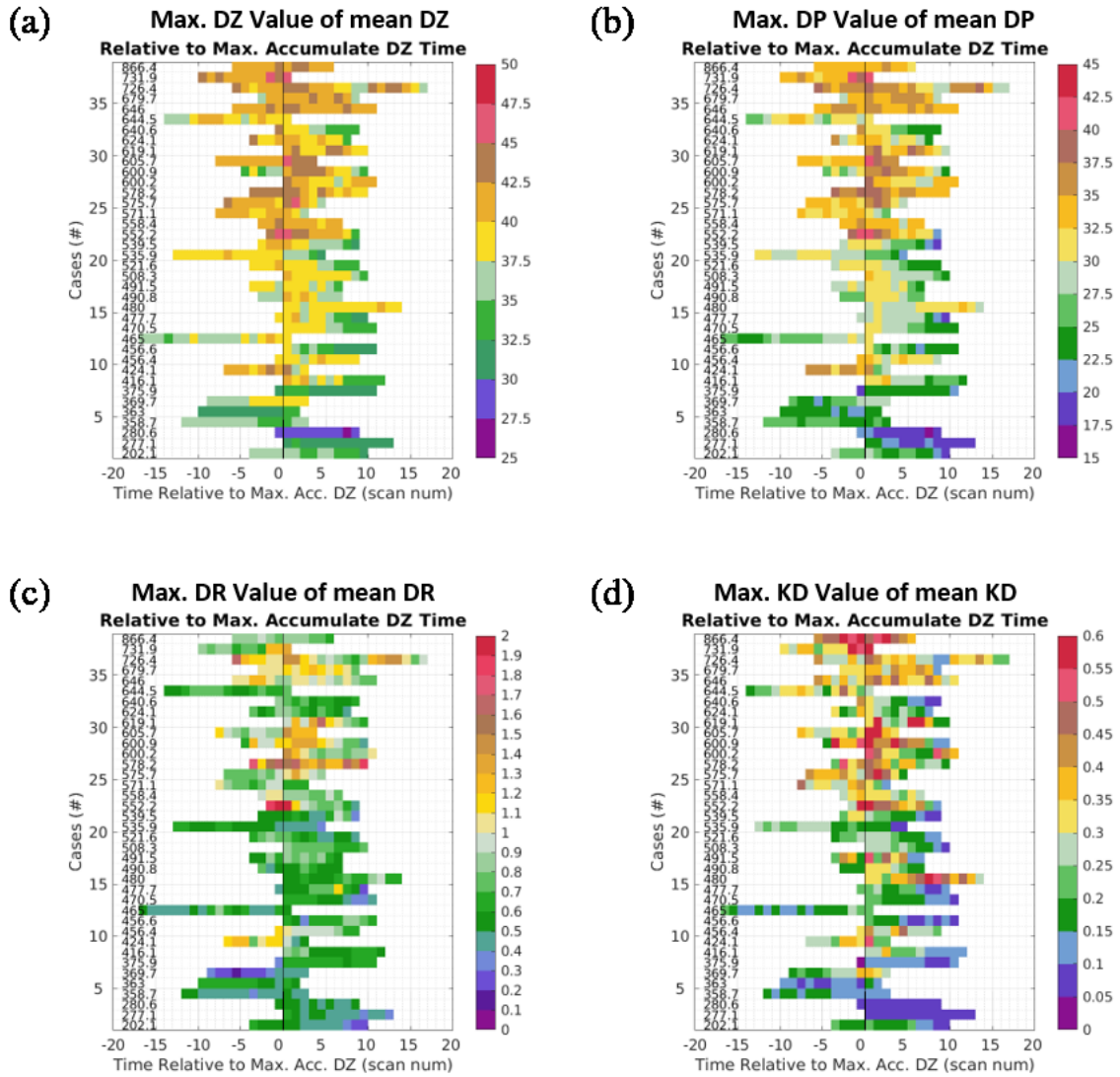


Figure 3.14 Maximum value of mean dual-polarimetric parameters, sort by maximum accumulative reflectivity. Number at the left-hand side in each figure is the value of maximum accumulative reflectivity of each case; x-axis for time, y-axis for cases. (a) Maximum value of mean Z_{HH} (b) Maximum value of mean Z_{DP} (c) Maximum value of mean Z_{DR} (d) Maximum value of mean K_{DP} .

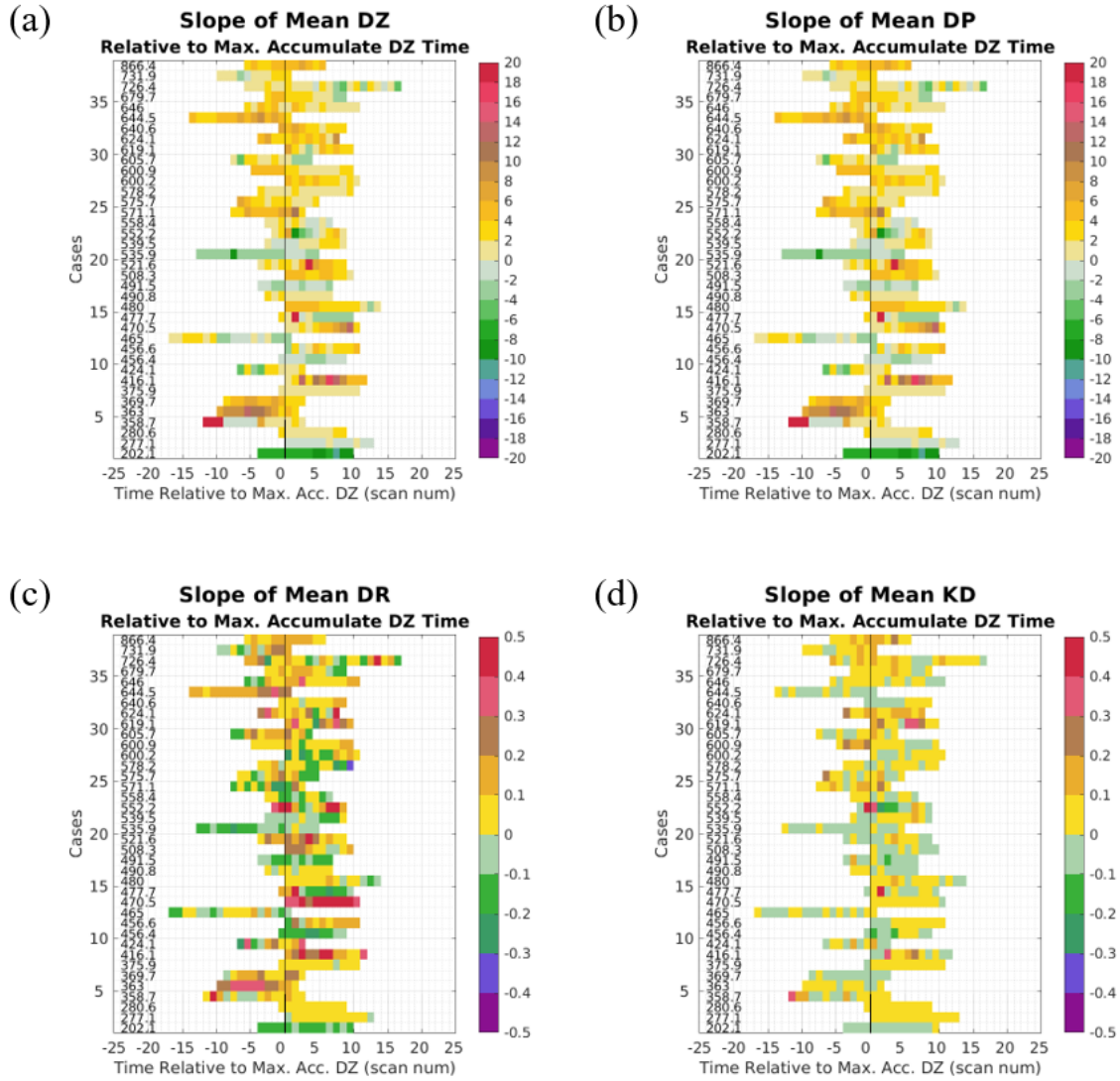


Figure 3.15 Vertical slope of mean dual-polarimetric parameters, sort by maximum accumulative reflectivity. Number at the left-hand side in each figure is the value of maximum accumulative reflectivity of each case; x-axis for time, y-axis for cases. (a) Vertical slope of mean Z_{HH} (b) Vertical slope of mean Z_{DP} (c) Vertical slope of mean Z_{DR} (d) Vertical slope of mean K_{DP} .

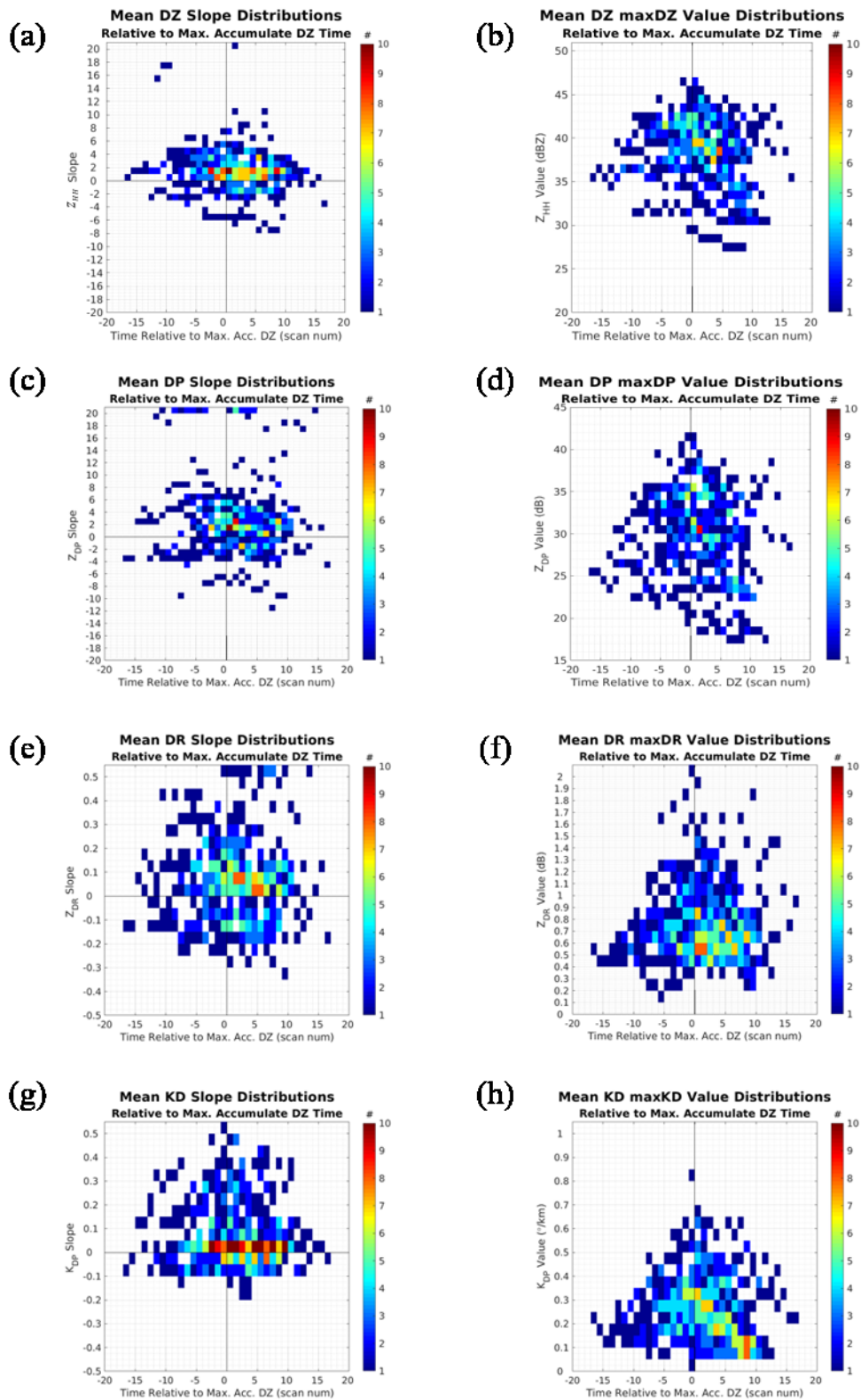


Figure 3.16 Number density distribution of dual-pol parameters vertical slope and maximum value with the time relative to the maximum accumulative reflectivity time. From the top panel to the bottom panel are Z_{HH} , Z_{DP} , Z_{DR} and K_{DP} . Left column for vertical slope and right column for maximum value.

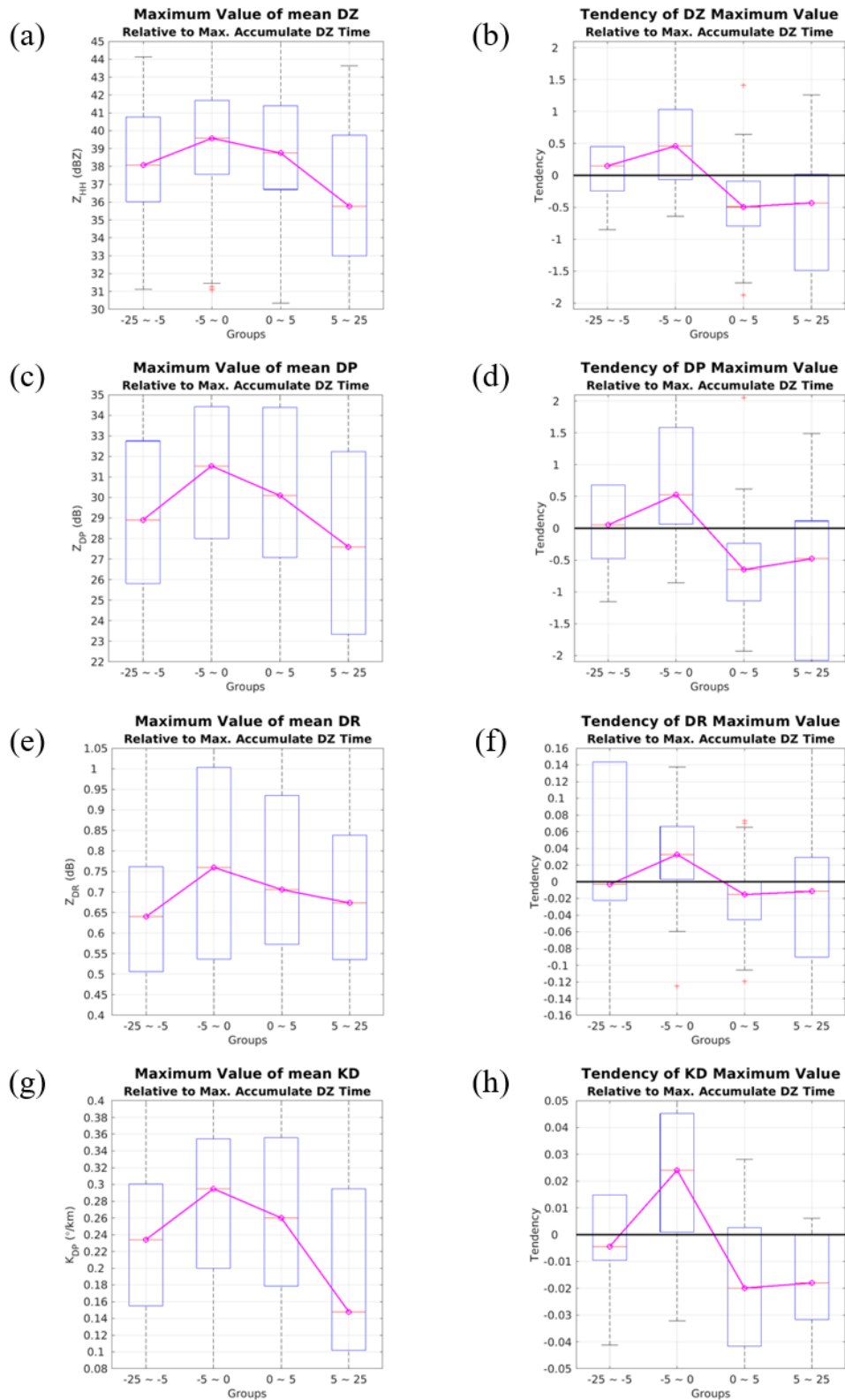


Figure 3.17 Boxplot of maximum value and tendency of maximum value relative to max.

acc. Z_{HH} divided in 4 groups. Left column for maximum value and right column for maximum value tendency. Magenta lines are the connection of Q2. (a), (b) for Z_{HH} . (c), (d) for Z_{DP} . (e), (f) for Z_{DR} . (g), (h) for K_{DP} .

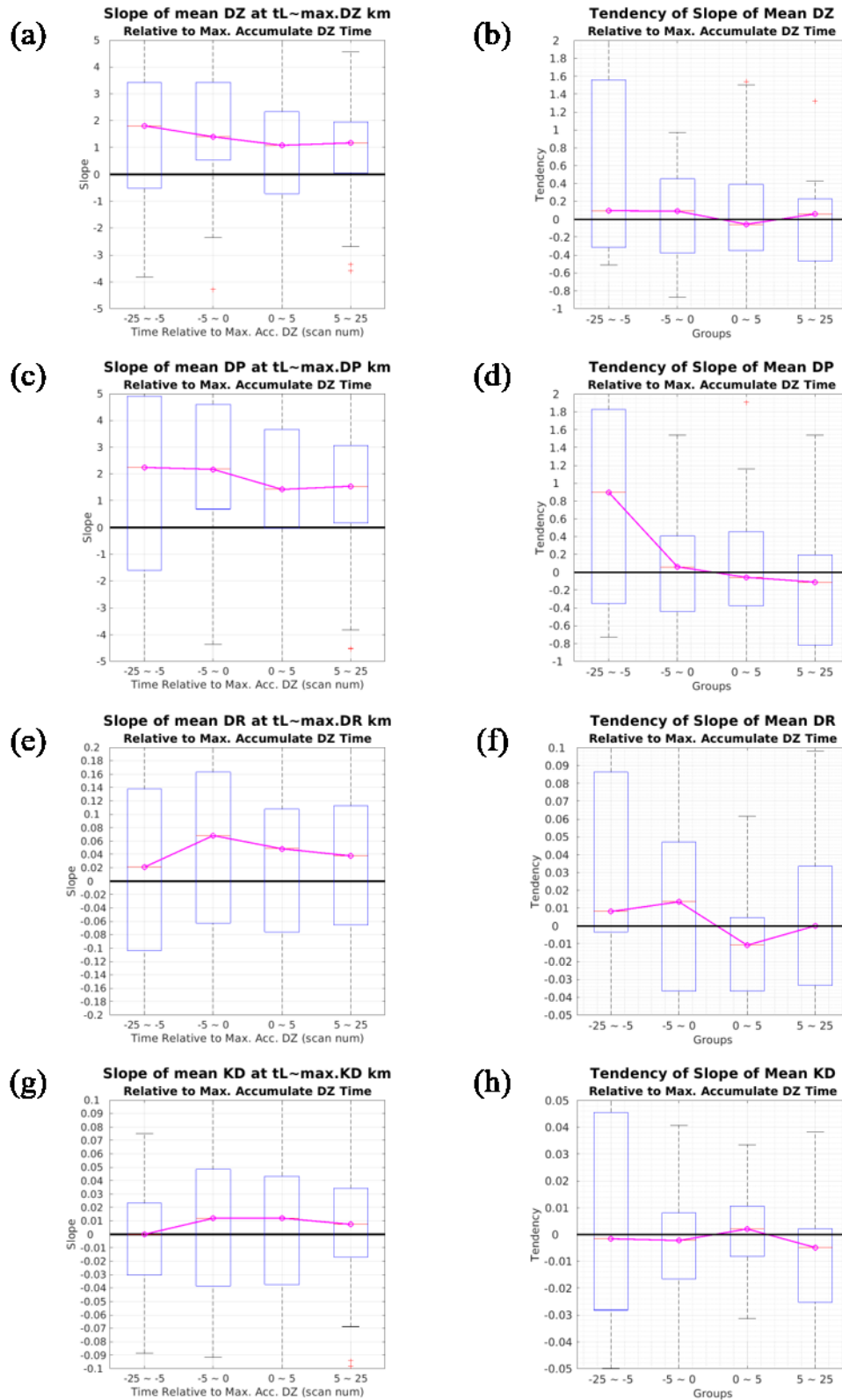


Figure 3. 18 Boxplot of vertical slope and tendency of slope relative to max. acc. Z_{HH} divided in 4 groups. Left column for vertical slope and right column for tendency of slope. Magenta lines are the connection of Q2. (a), (b) for Z_{HH} . (c), (d) for Z_{DP} . (e), (f) for Z_{DR} . (g), (h) for K_{DP} .

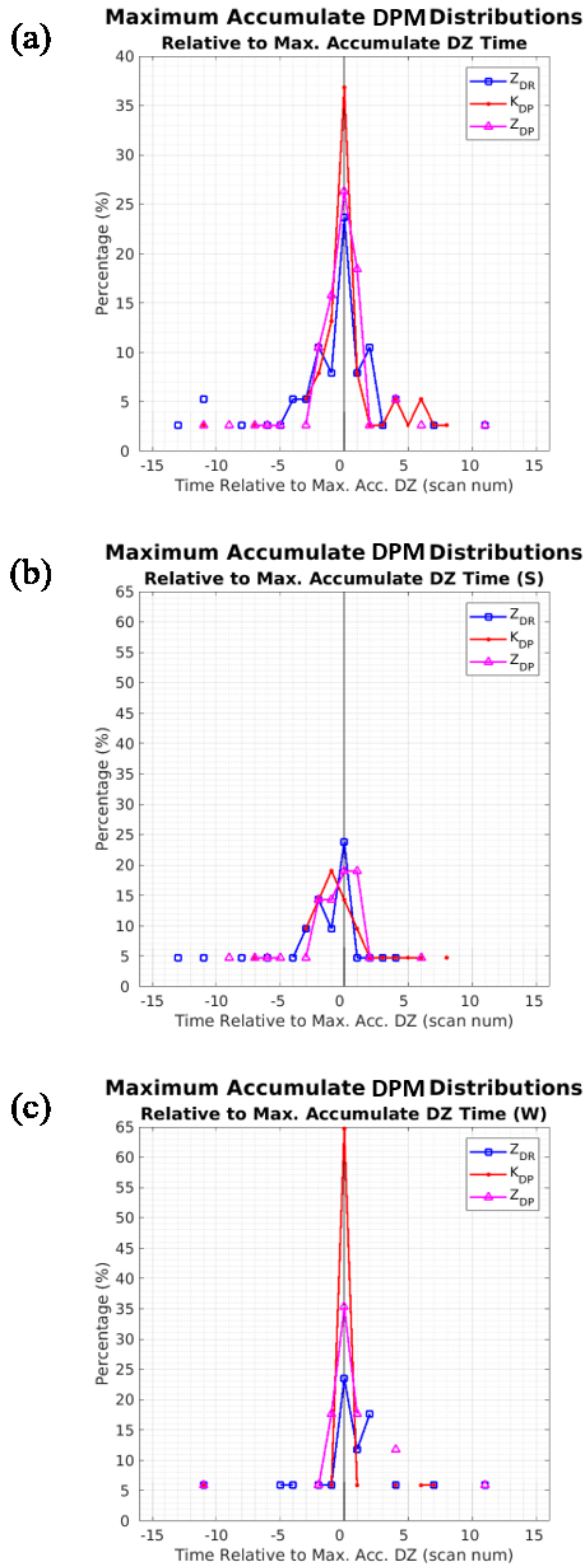


Figure 3. 19 Time distribution of maximum dual-polarimetric parameters relative to max. acc.

Z_{HH} . Blue line for Z_{DR} ; Red line for K_{DP} ; Magenta line for Z_{DP} . (a) All cases. (b)

Strong cases only. (c) Weak cases only.

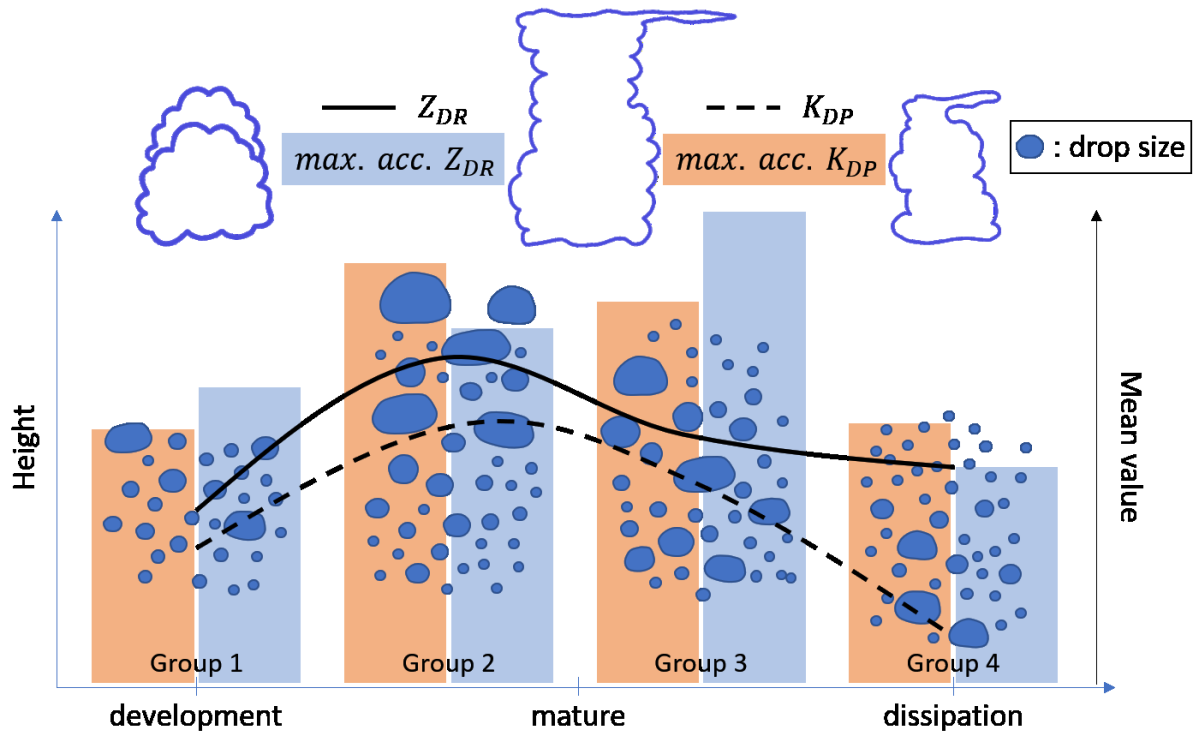


Figure 3. 20 A conceptual model of Z_{DR} and K_{DP} characteristics during storm evolution.

X-axis shows the storm evolution; Left y-axis shows the approximately height and right y-axis shows the relative mean value of DPMs, black solid line for mean Z_{DR} value and black dash line for mean K_{DP} value. Orange (Blue) shading represent the percentage of time distribution of max. acc. K_{DP} (max. acc. Z_{DR}) relative to max. acc. Z_{HH} time.

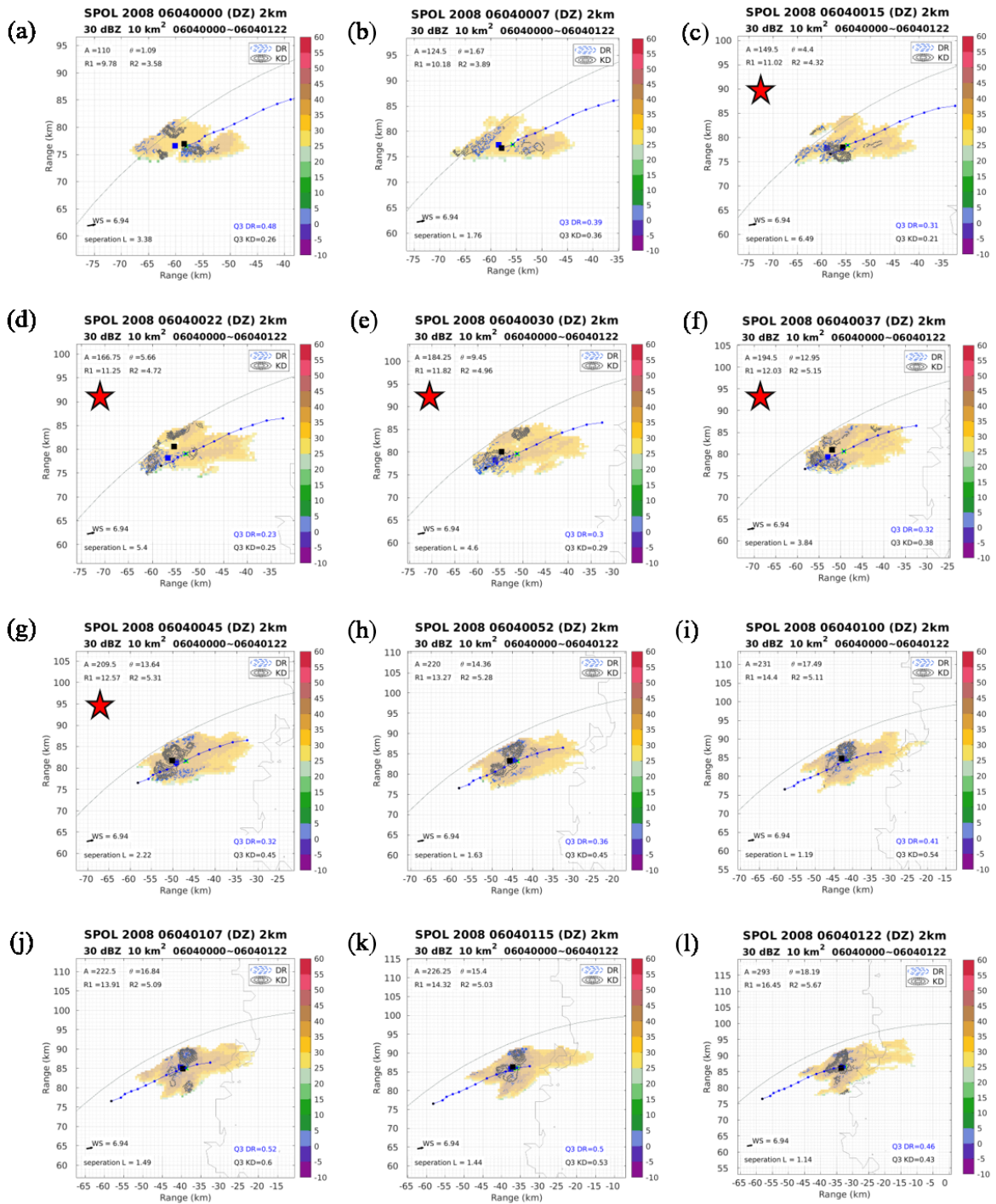


Figure 3. 21 Storm horizontal distribution of reflectivity during the storm track at 2-kilometer height of case 22. Shading represent reflectivity in dBZ. Blue dot line is the storm path. Green cross is the storm reflectivity weighted center. Blue and black contour lines are the enhance Z_{DR} and K_{DP} region, with the center of enhance region shown as blue and black square respectively.

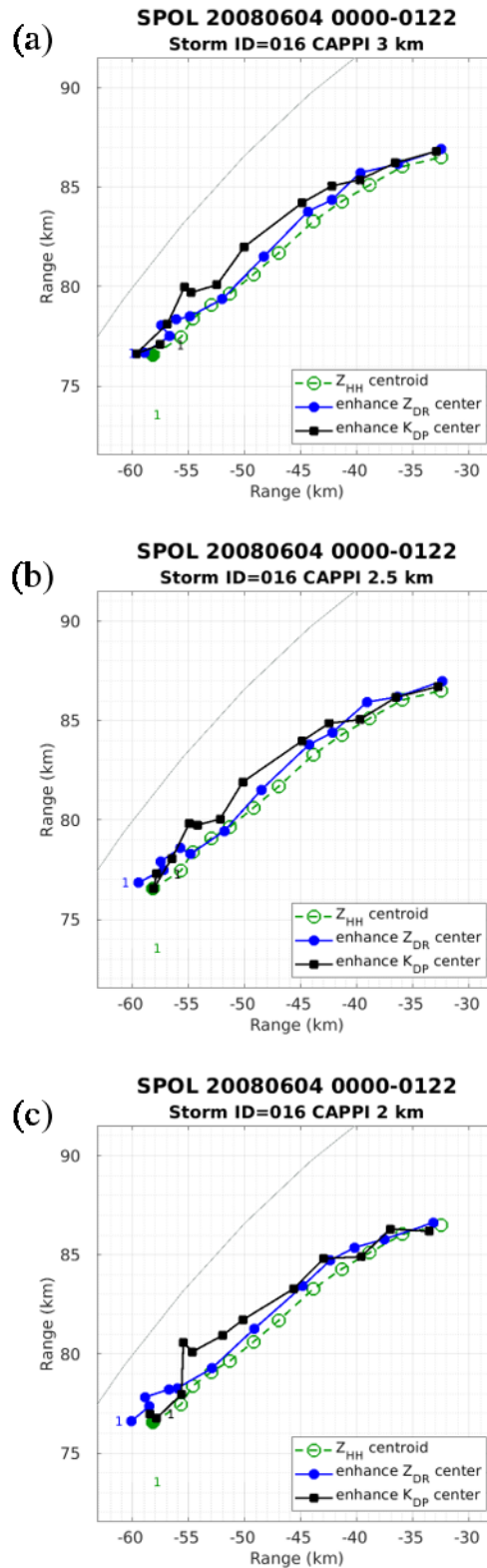


Figure 3. 22 Enhance Z_{DR} and K_{DP} center path at different height of case 22. (a) 3-kilometer height. (b) 2.5-kilometer height. (c) 2-kilometer height.

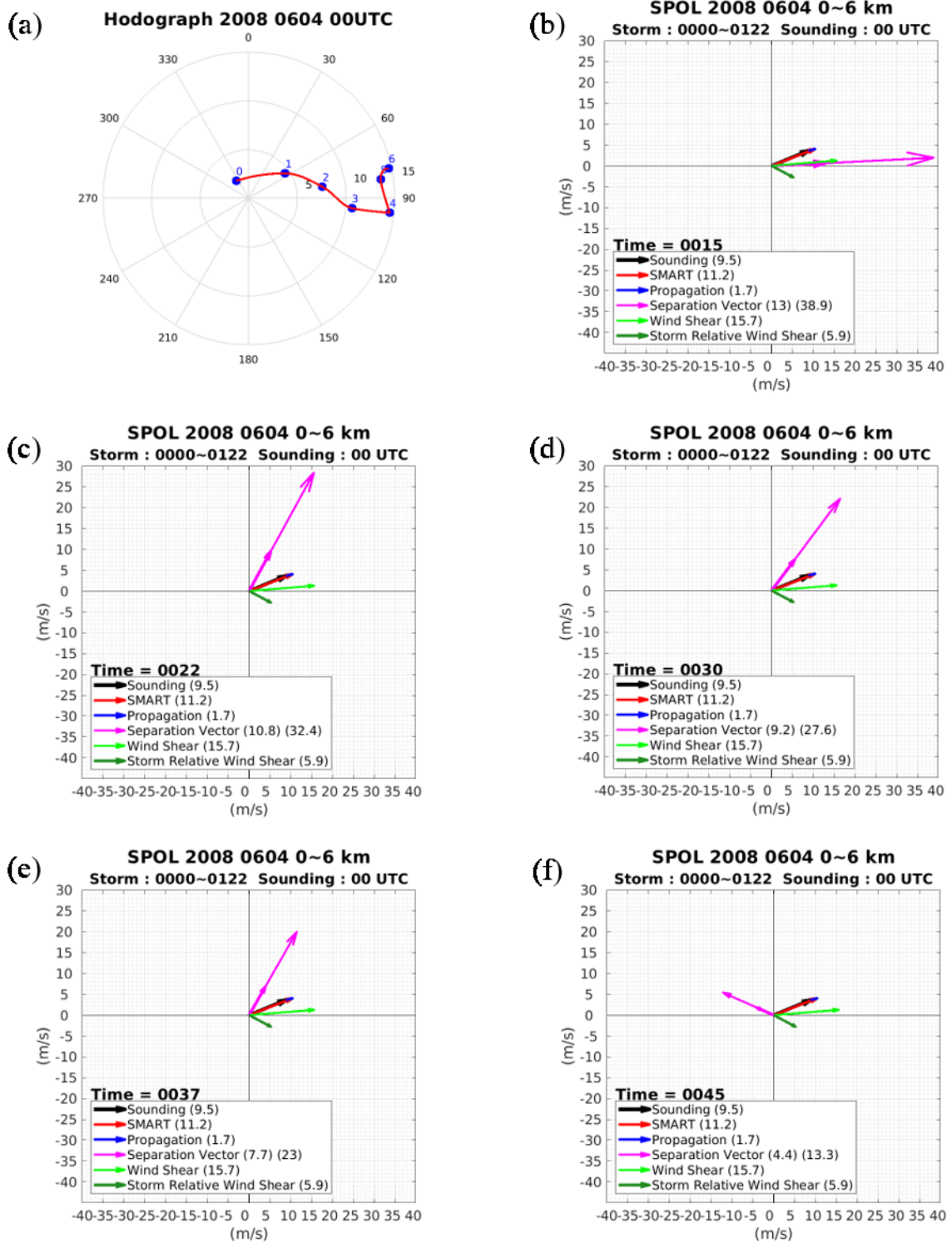


Figure 3.23 Hodograph and vectors of case 22. (a) Hodograph of 00 UTC sounding data.

Meaning of different vectors in (b), (c), (d), (e) and (f) are as below: Black color for cell motion; Red color for system motion; Blue color for storm propagation; Magenta color for separation vector; Light green color for wind shear between 0 to 6 km height; Grass green color for storm relative wind shear. Numbers behind are the speed of each vector.

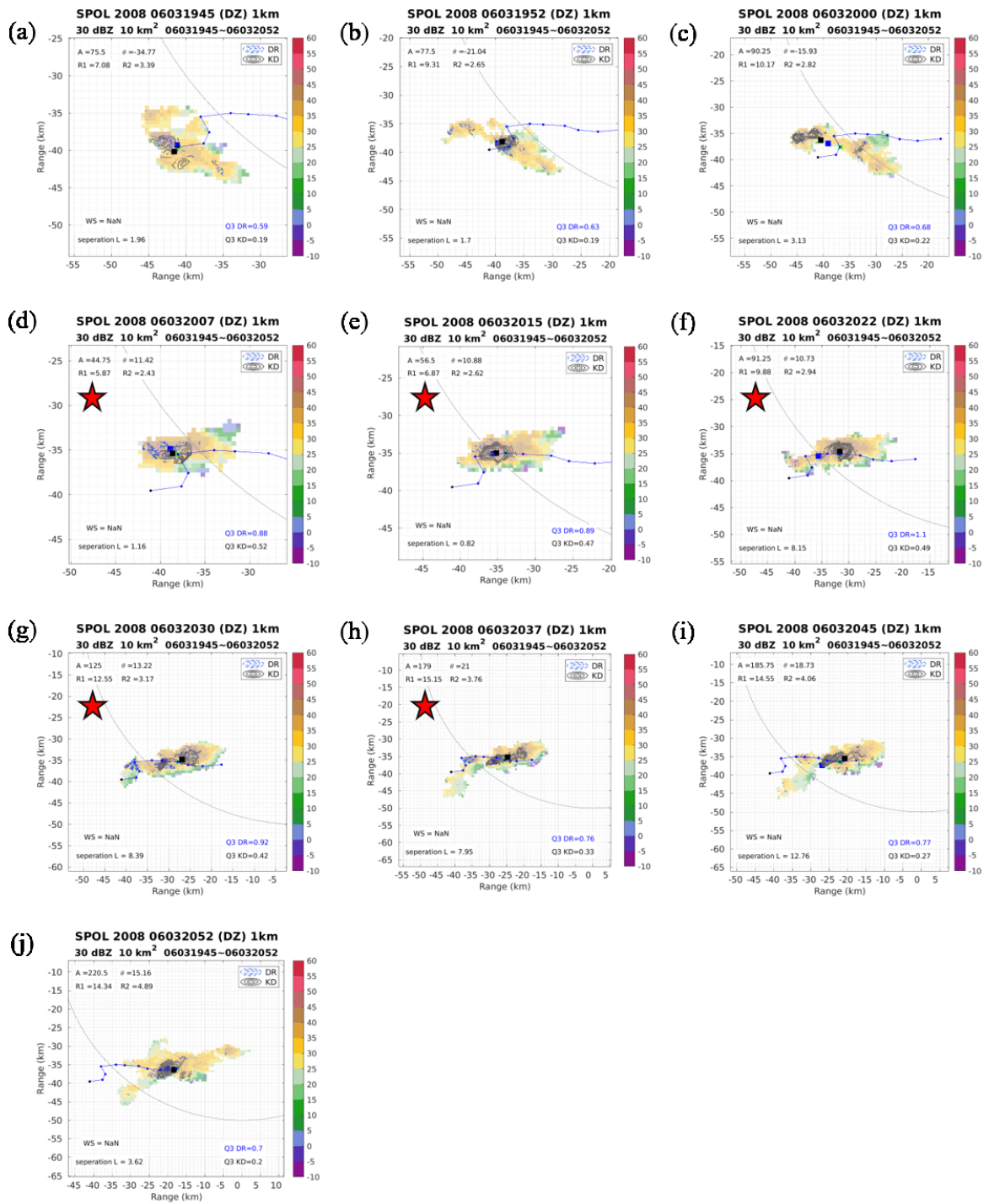


Figure 3.24 Same as Figure 3.21, but for case 20.

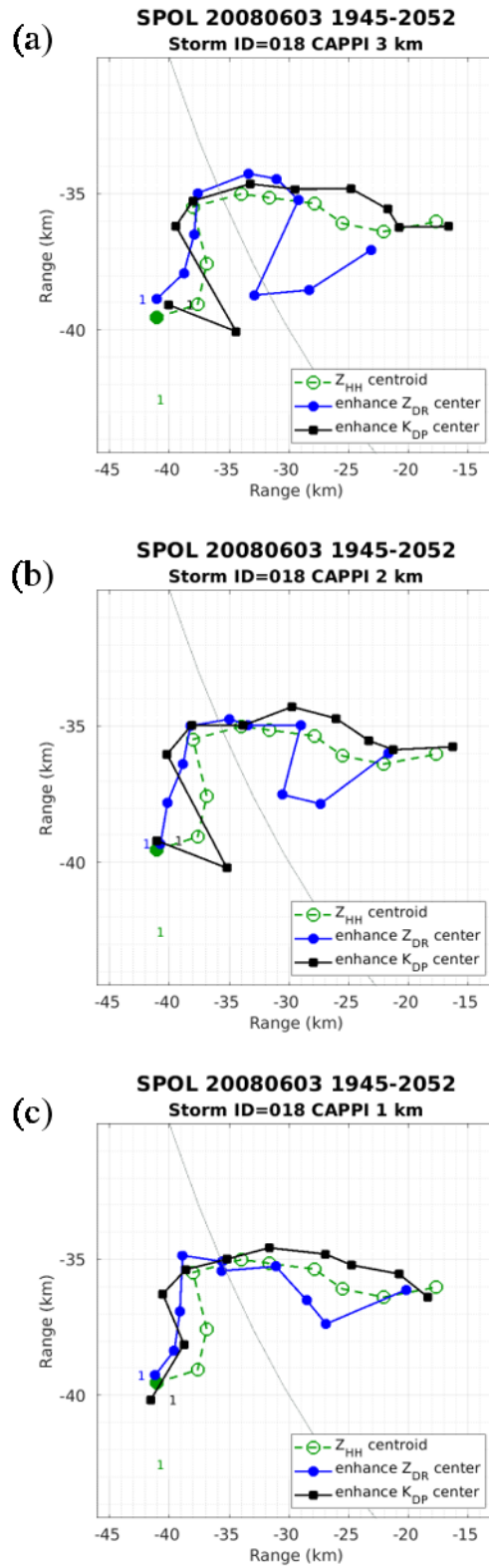


Figure 3. 25 Enhance Z_{DR} and K_{DP} center path at different height of case 20. (a) 3-kilometer height. (b) 2-kilometer height. (c) 1-kilometer height.

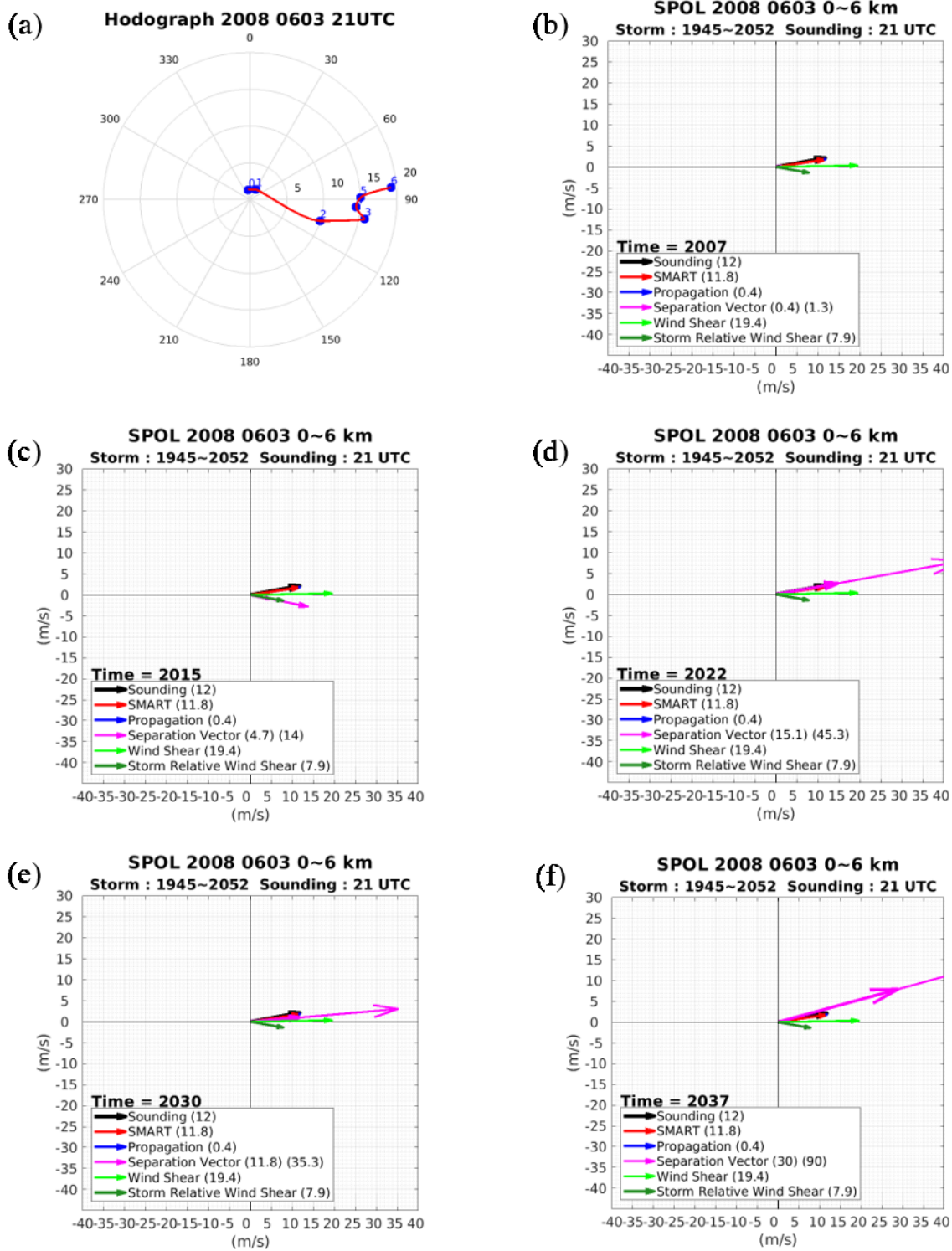


Figure 3.26 Same as Figure 3.23, but for case 20.

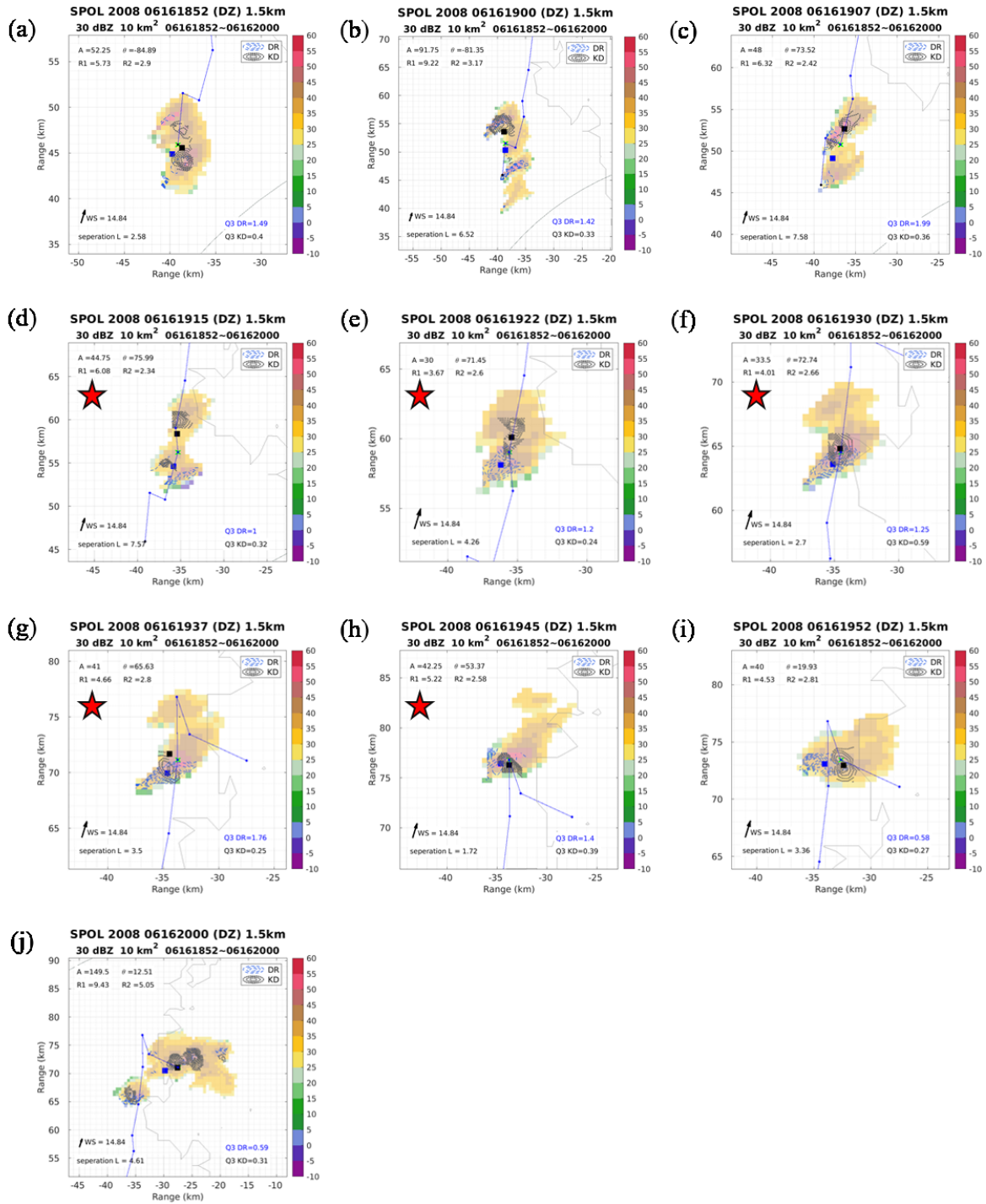


Figure 3.27 Same as Figure 3.21, but for case 34.

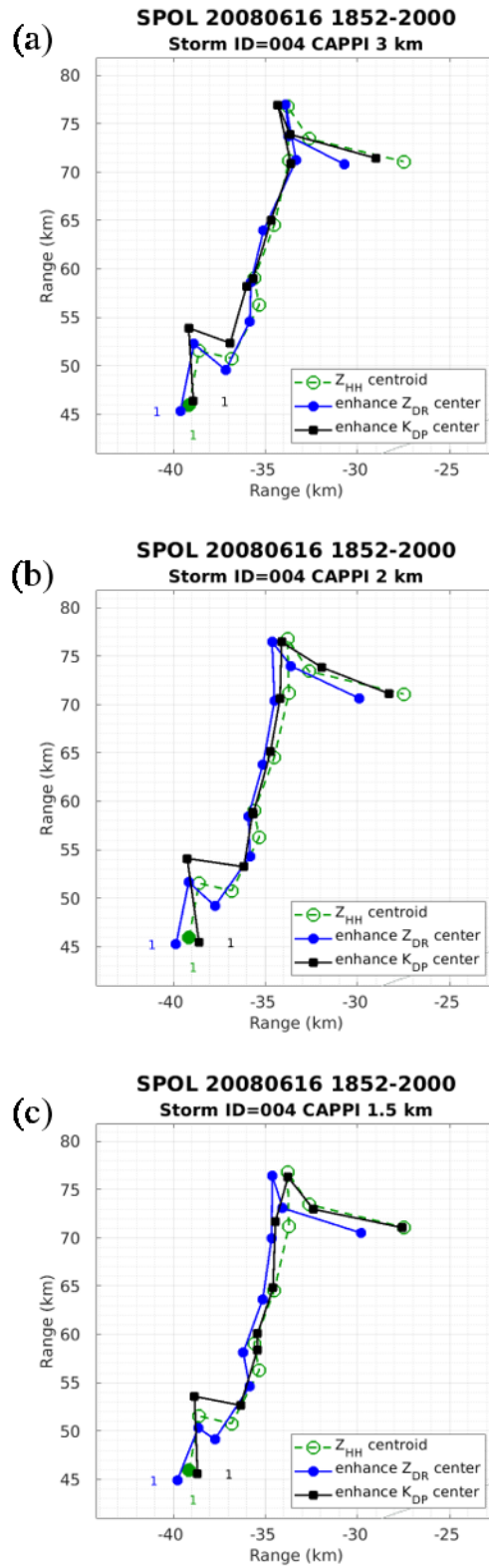


Figure 3. 28 Enhance Z_{DR} and K_{DP} center path at different height of case 34. (a) 3-kilometer height. (b) 2-kilometer height. (c) 1.5-kilometer height.

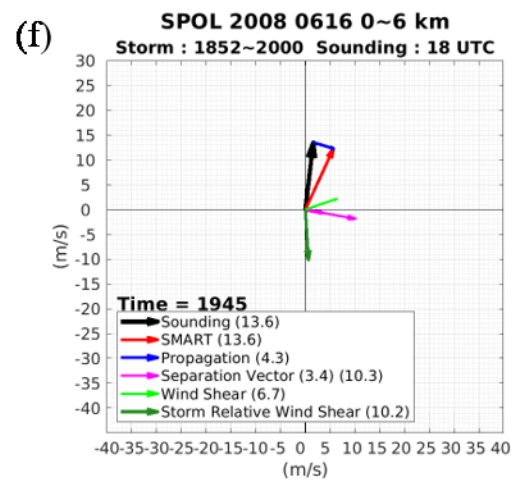
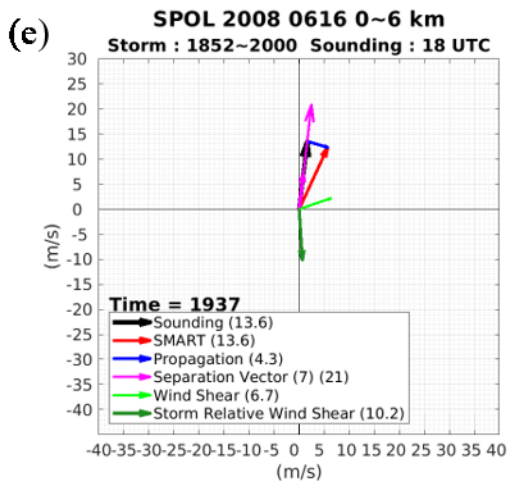
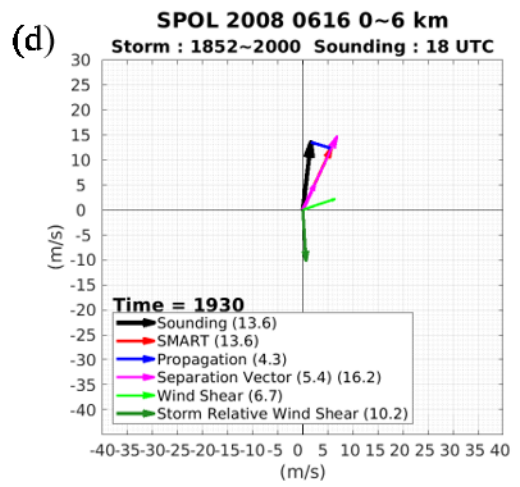
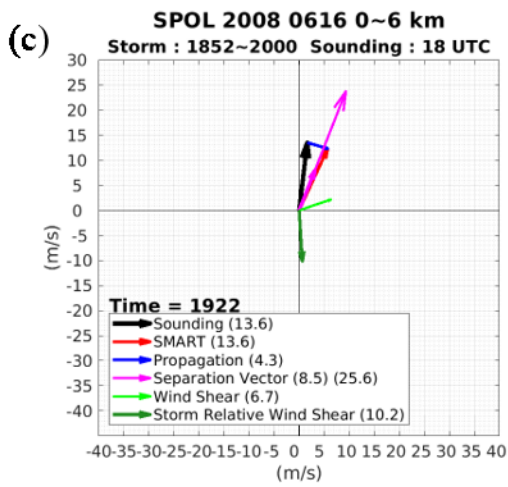
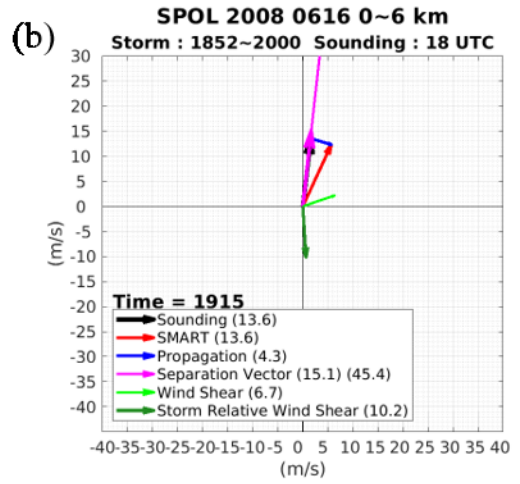
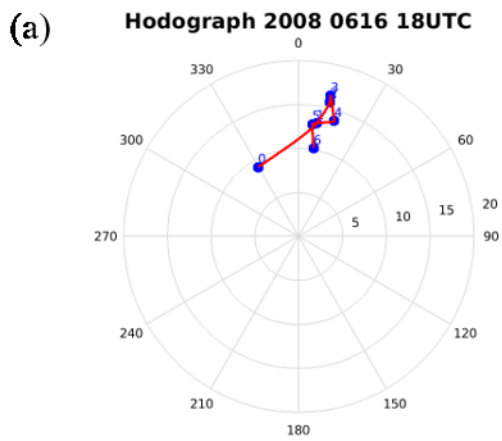


Figure 3. 29 Same as Figure 3. 23, but for case 34.

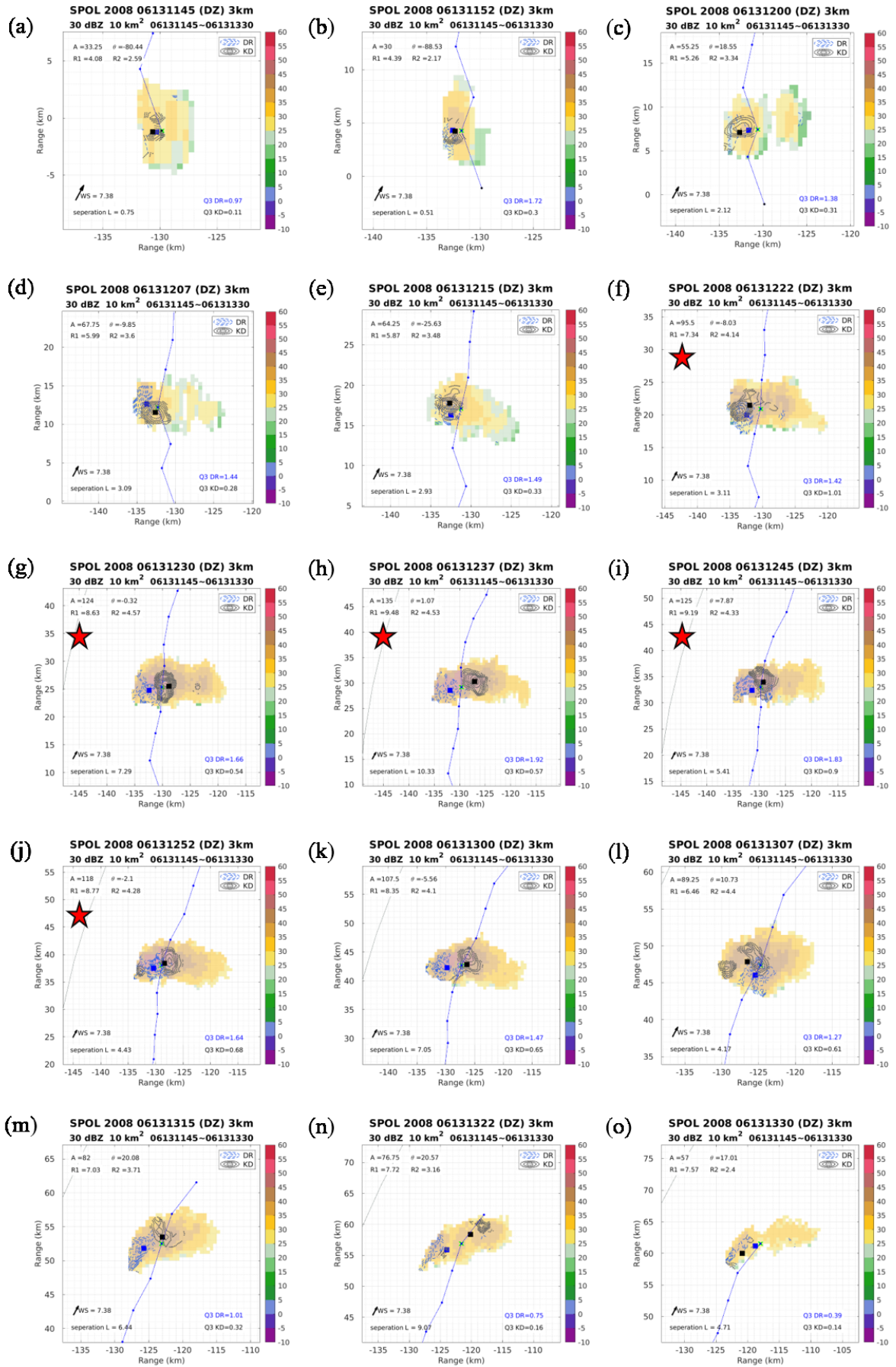


Figure 3.30 Same as Figure 3.21, but for case 29.

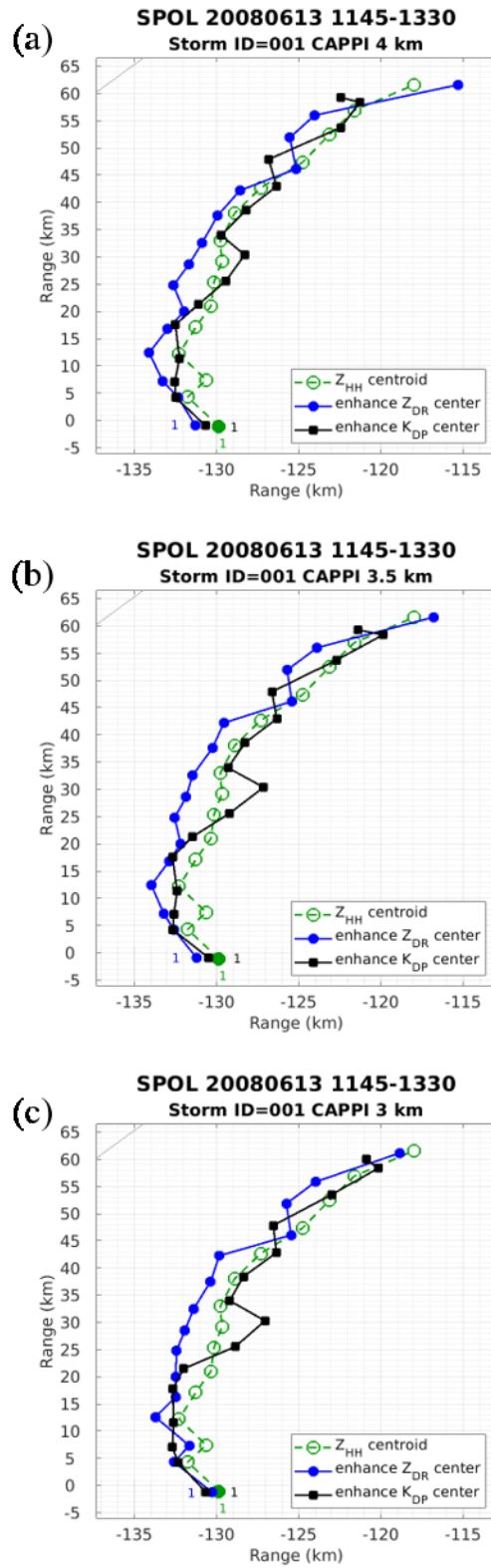


Figure 3. 31 Enhance Z_{DR} and K_{DP} center path at different height of case 29. (a) 4-kilometer height. (b) 3.5-kilometer height. (c) 3-kilometer height.

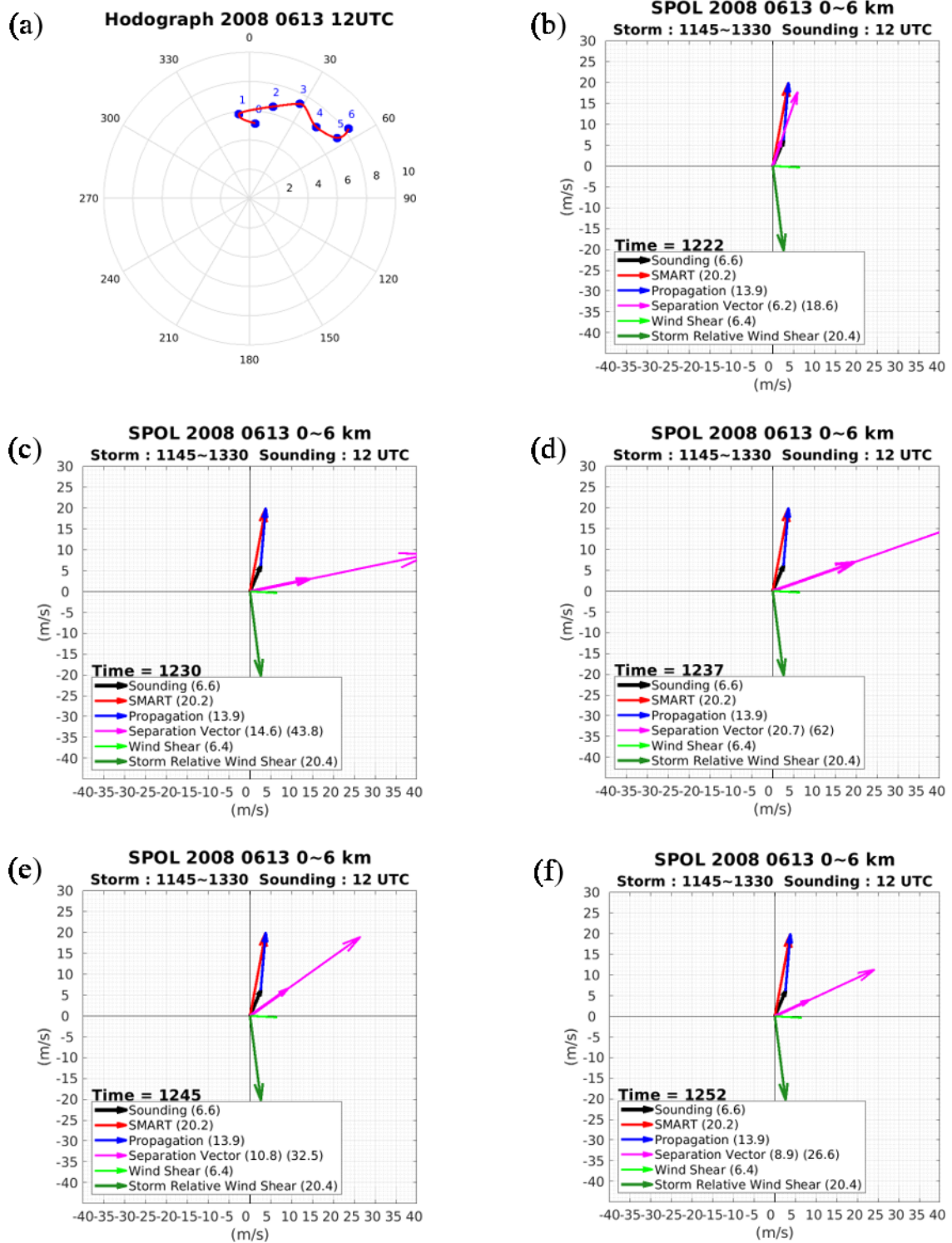


Figure 3.32 Same as Figure 3.23, but for case 29.

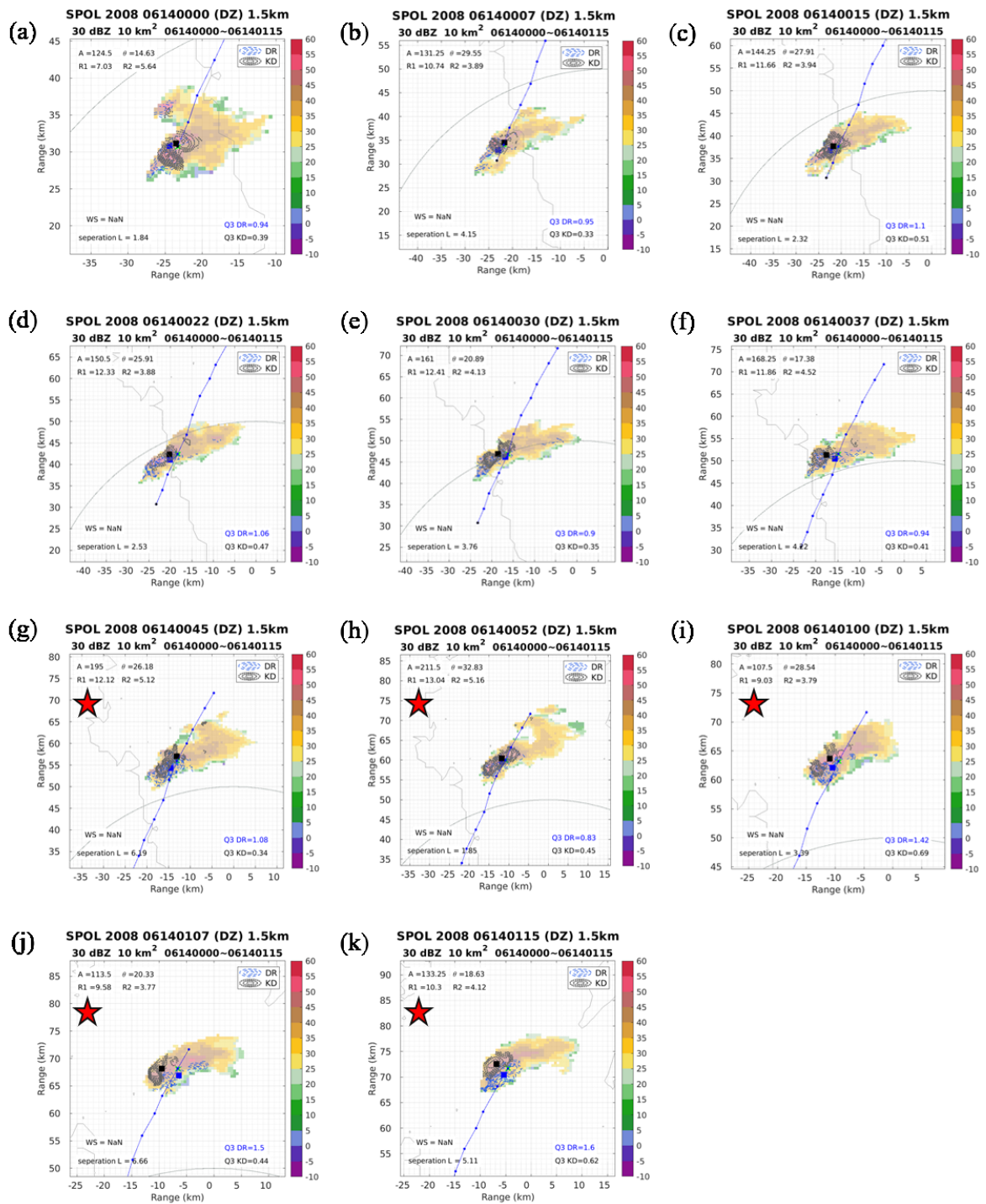


Figure 3.33 Same as Figure 3.21, but for case 30.

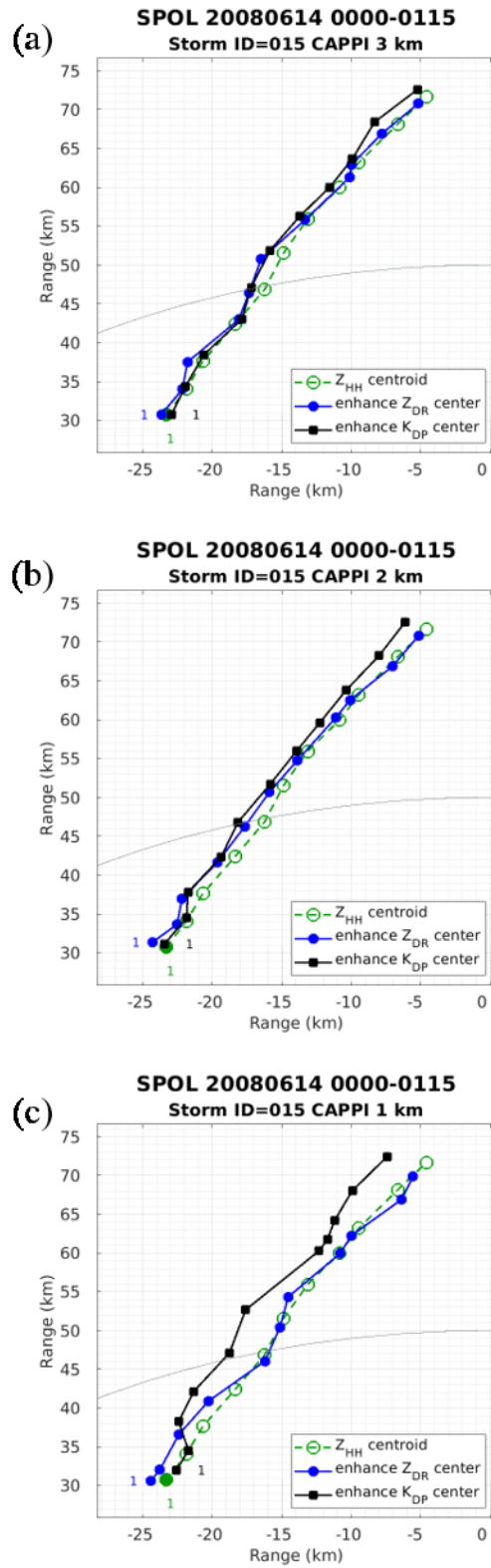


Figure 3. 34 Enhance Z_{DR} and K_{DP} center path at different height of case 30. (a) 3-kilometer height. (b) 2-kilometer height. (c) 1-kilometer height.

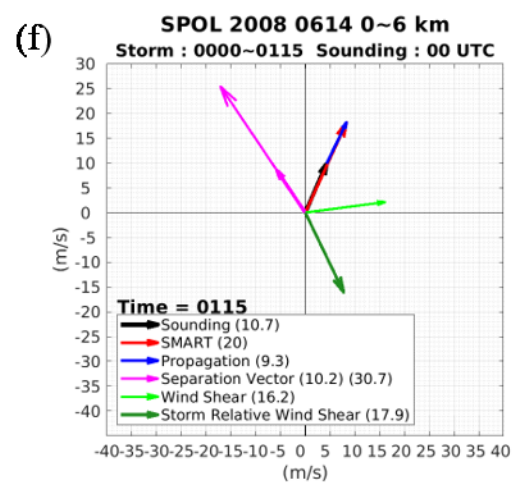
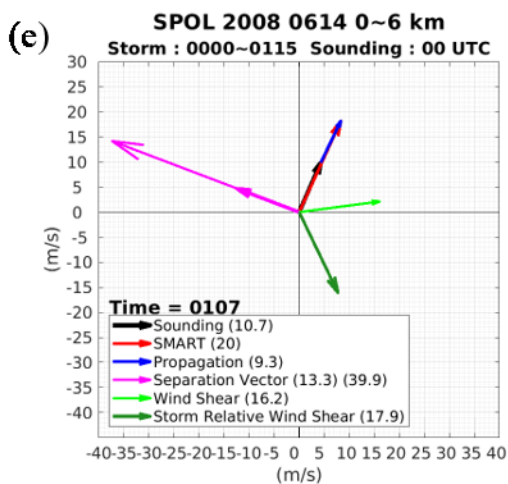
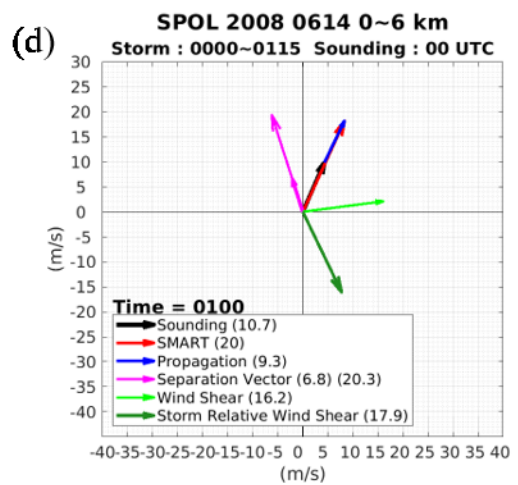
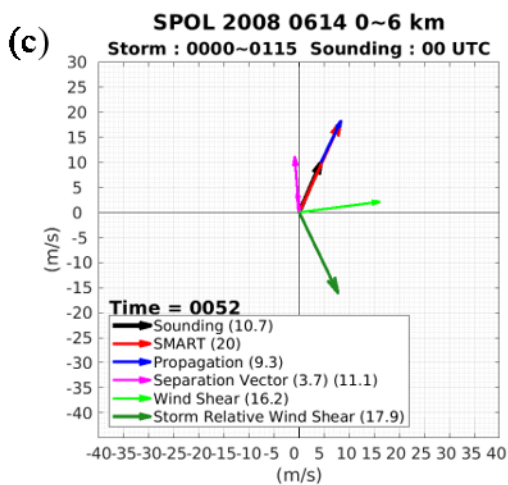
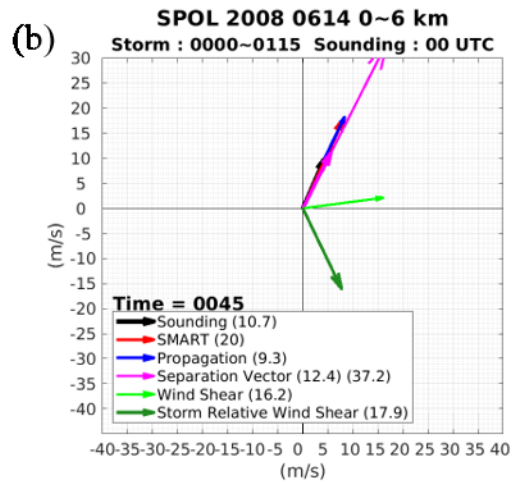
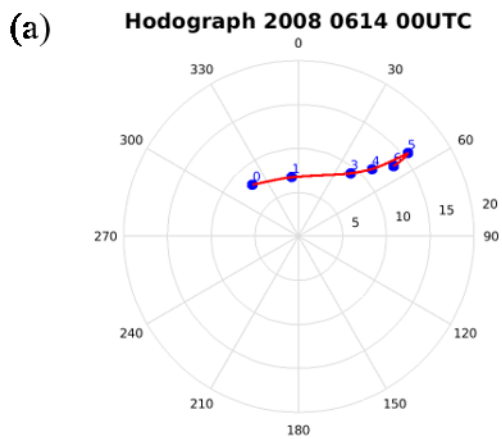


Figure 3.35 Same as Figure 3.23, but for case 30.

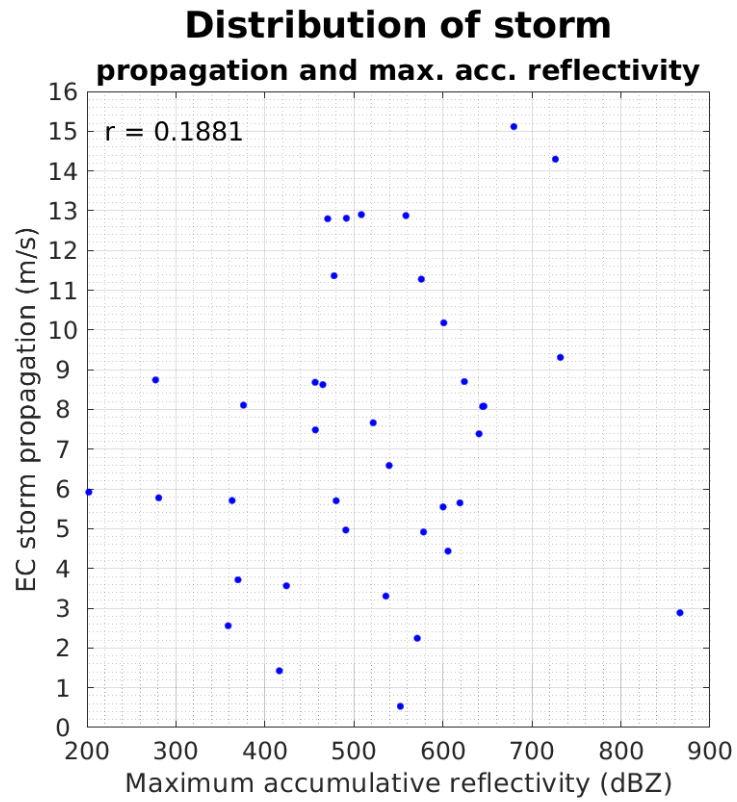


Figure 3.36 Distribution of storm propagation and maximum accumulative reflectivity of 38 cases.

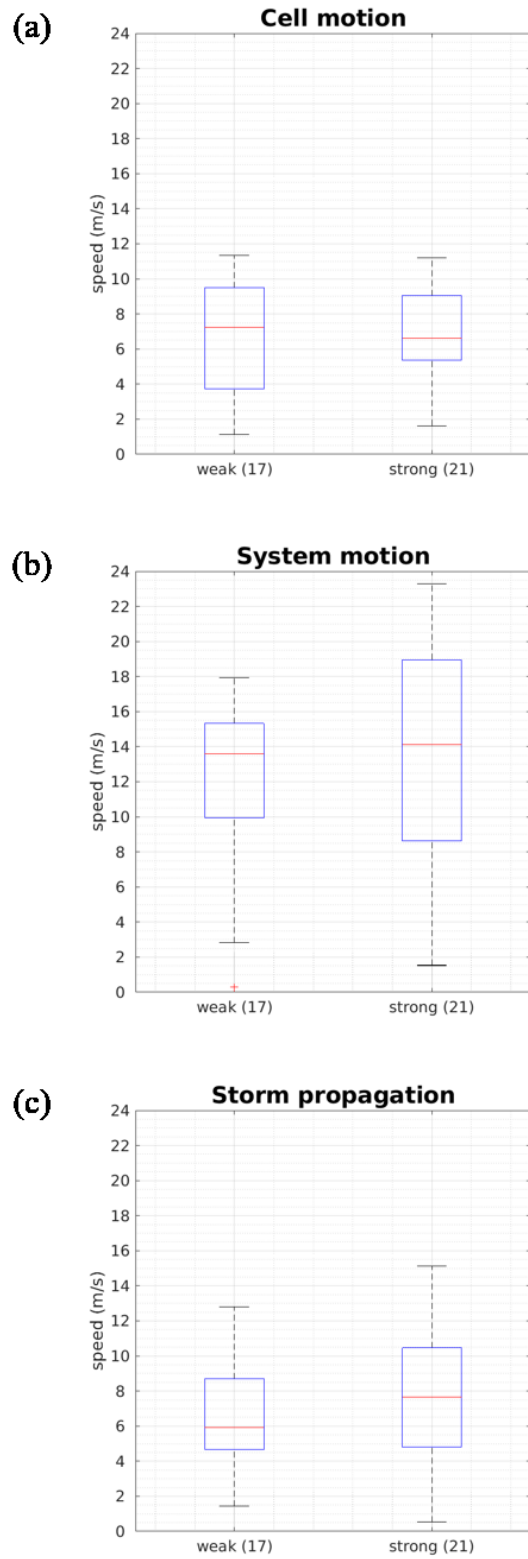
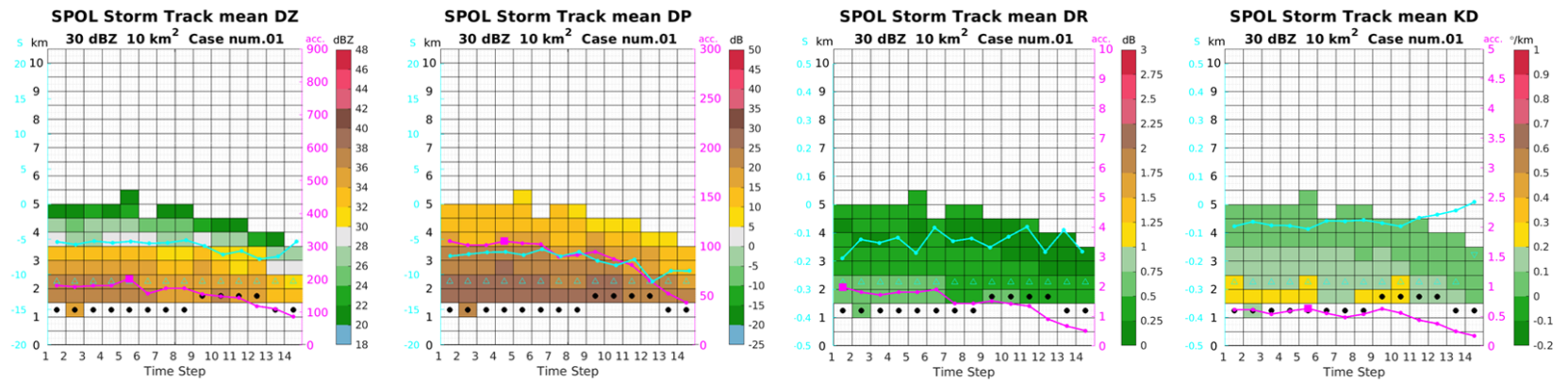


Figure 3.37 Distribution of different vector, separated by storm strength. Parentheses in x-axis present the number of weak and strong cases. (a) Cell motion (b) System motion (c) Storm propagation.

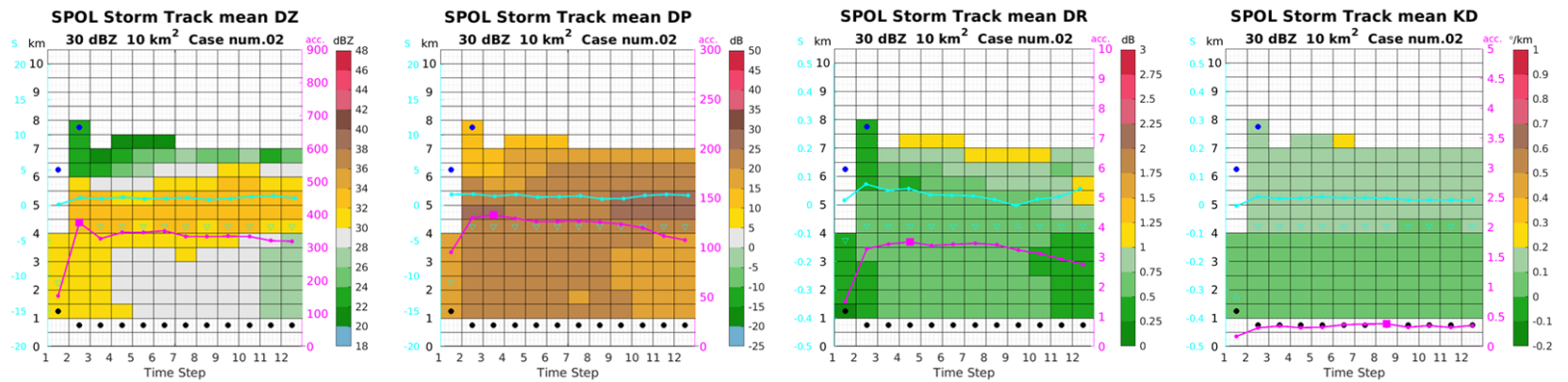
Appendix

A. Time height series of mean dual-polarimetric parameters of 17 weak cases

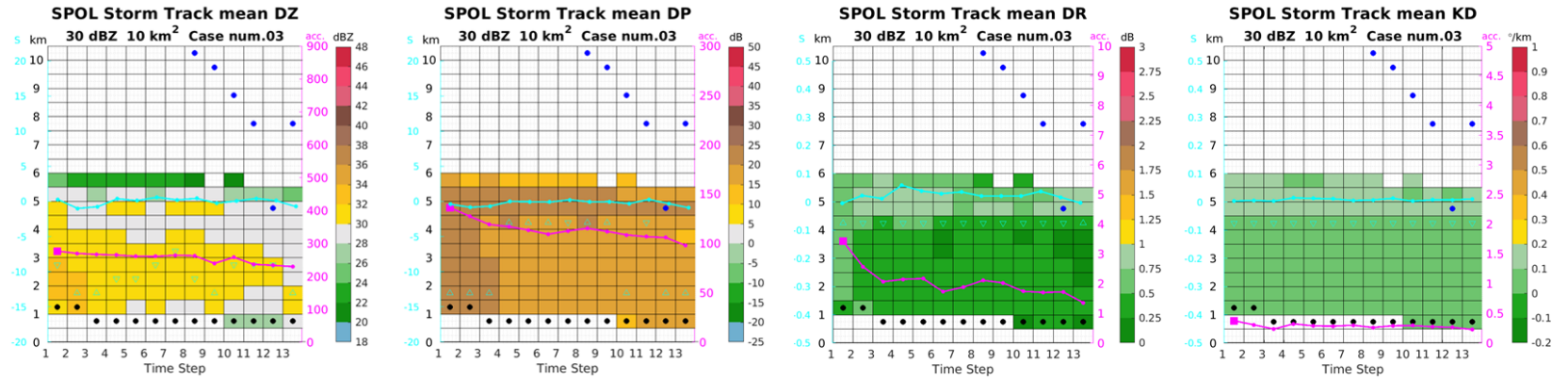
A.1
Case number 1



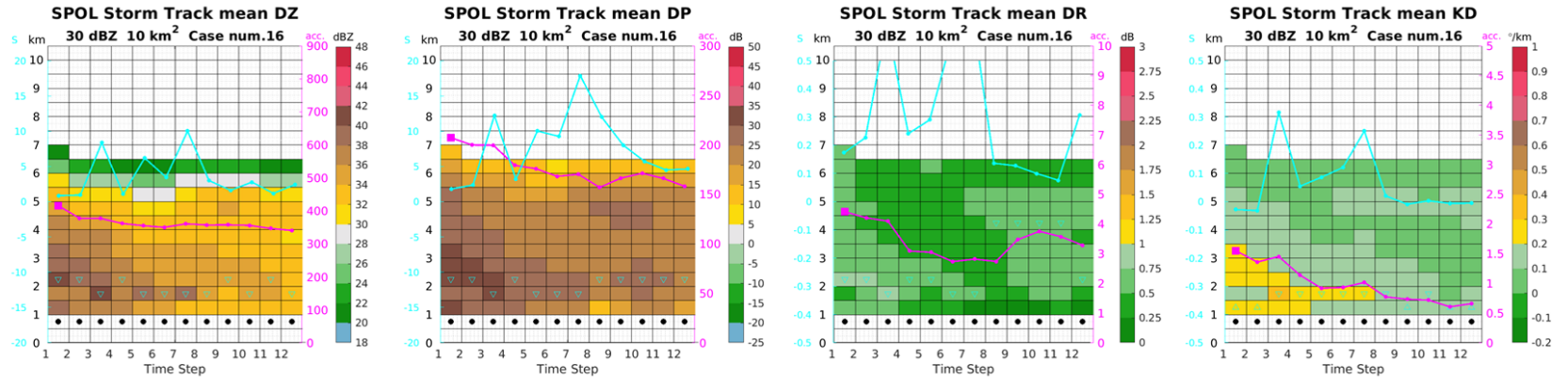
A.2
Case number 2



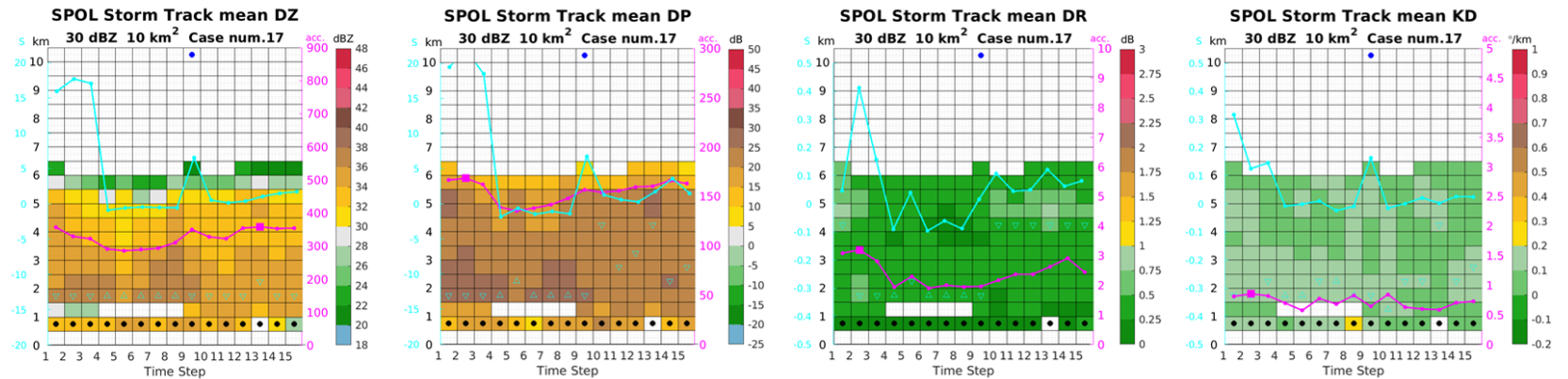
A.3
Case number 3



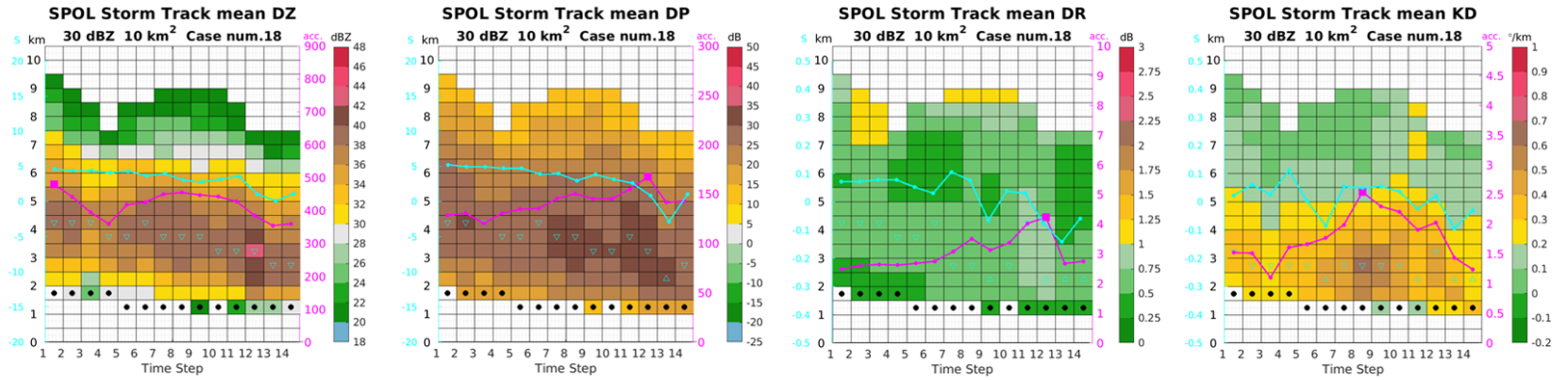
A.4
Case number 16



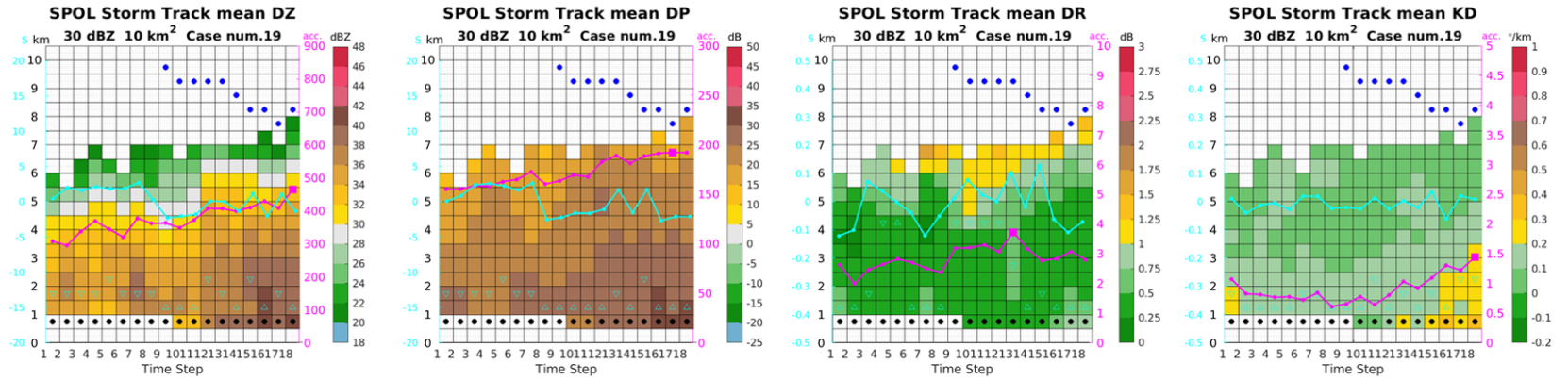
A.5
Case number 17



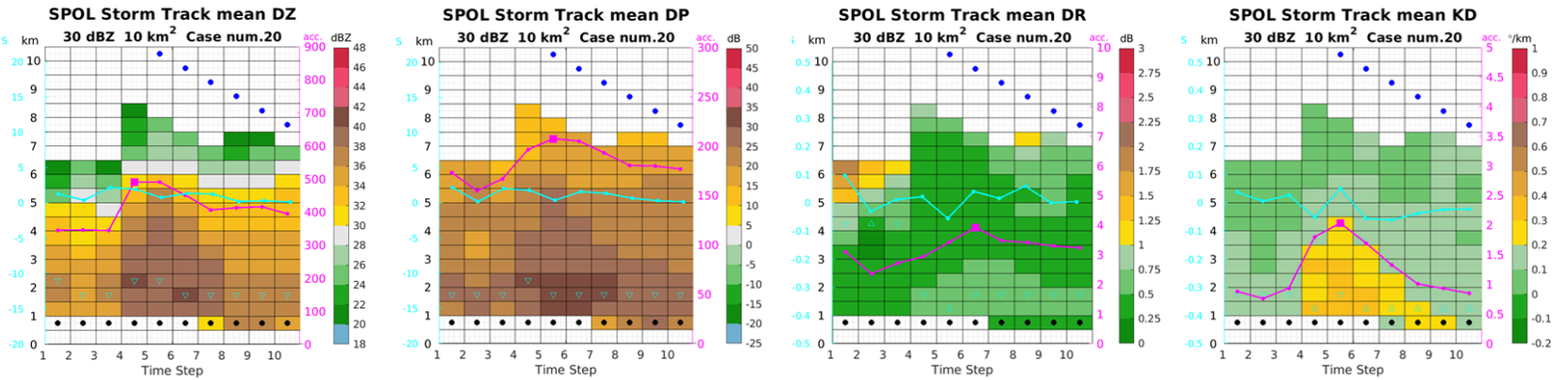
A.6
Case number 18



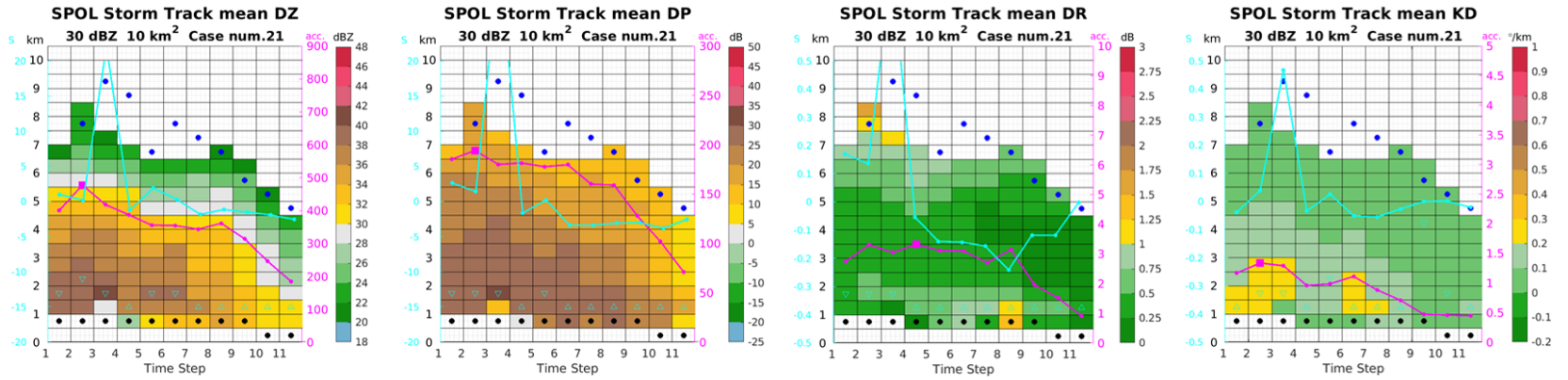
A.7
Case number 19



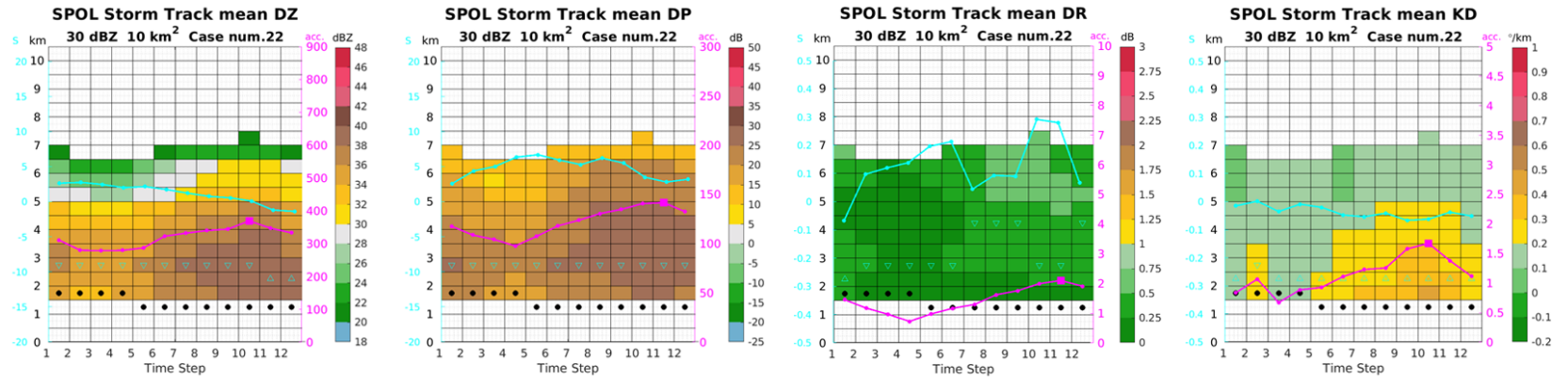
A.8
Case number 20



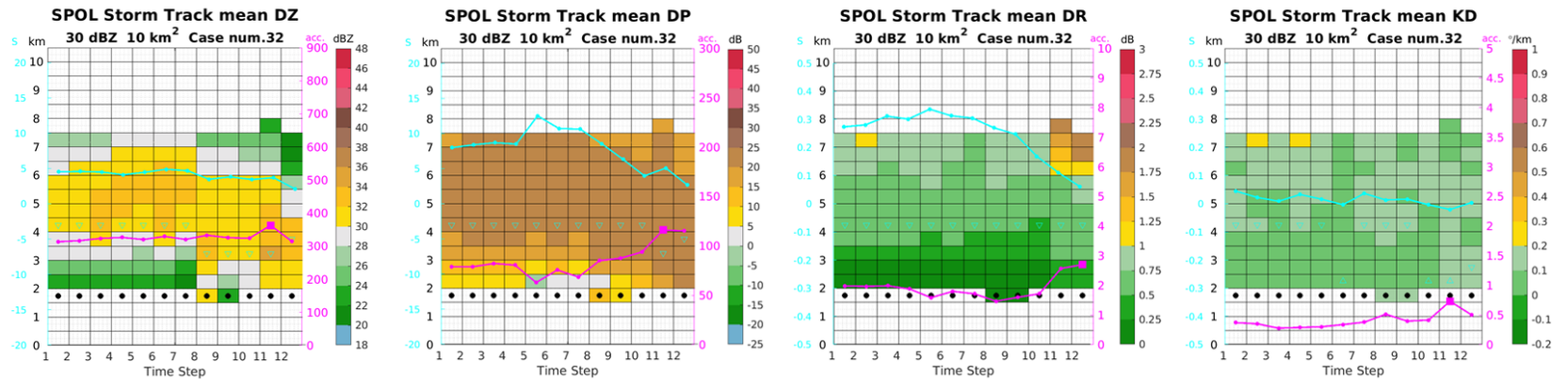
A.9
Case number 21



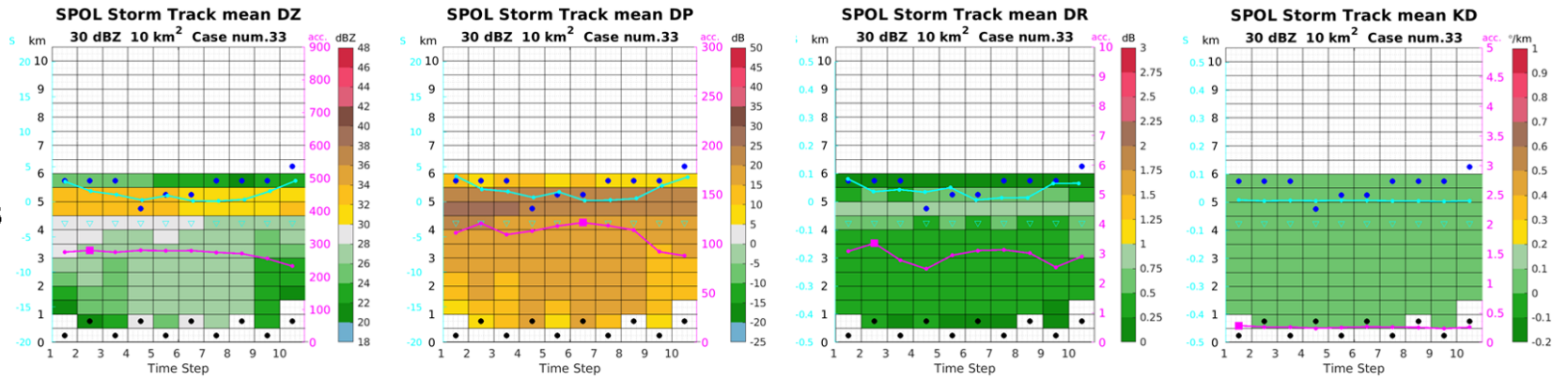
A.10
Case number 22



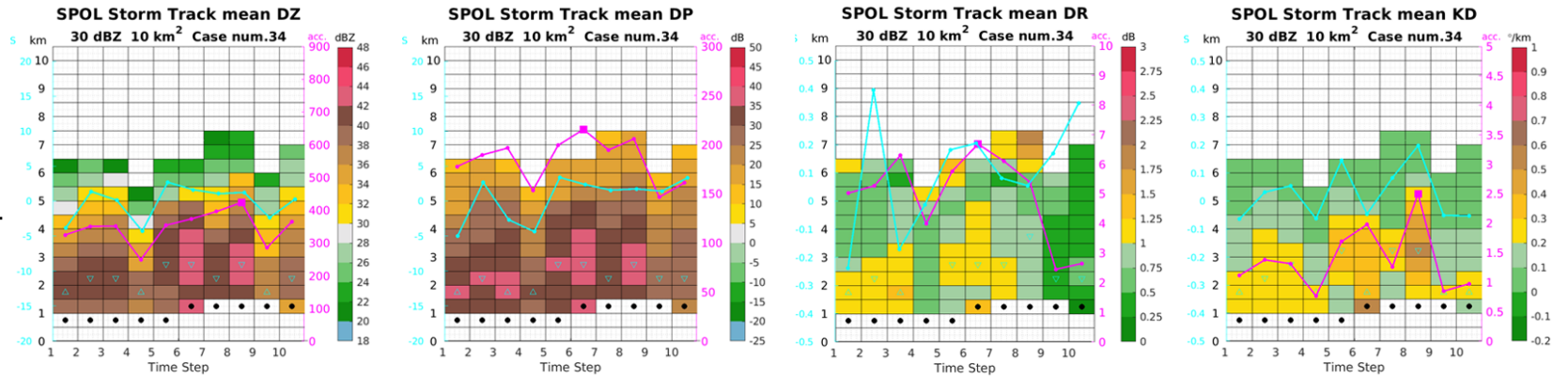
A.11
Case number 32



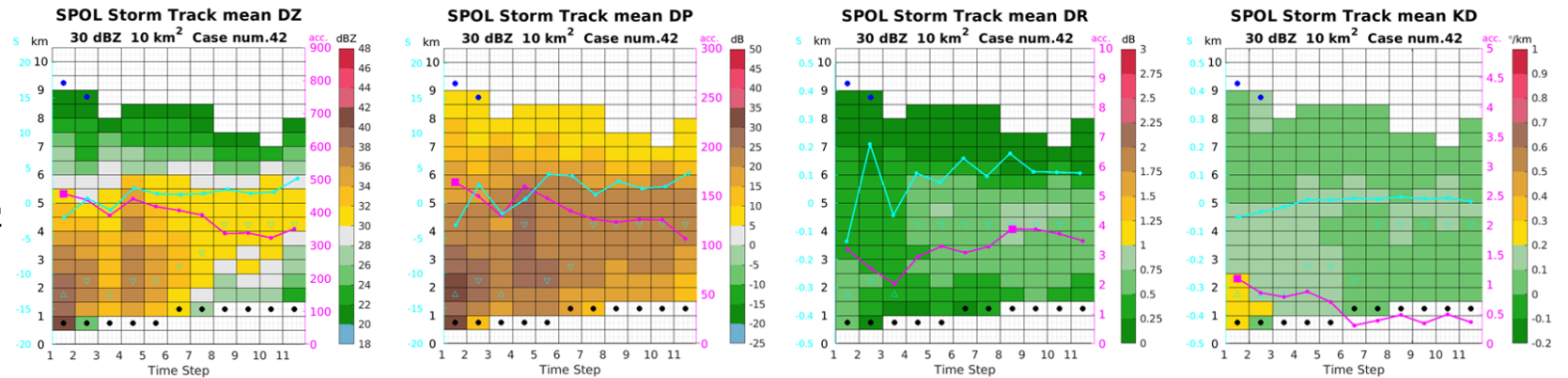
A.12
Case number 33



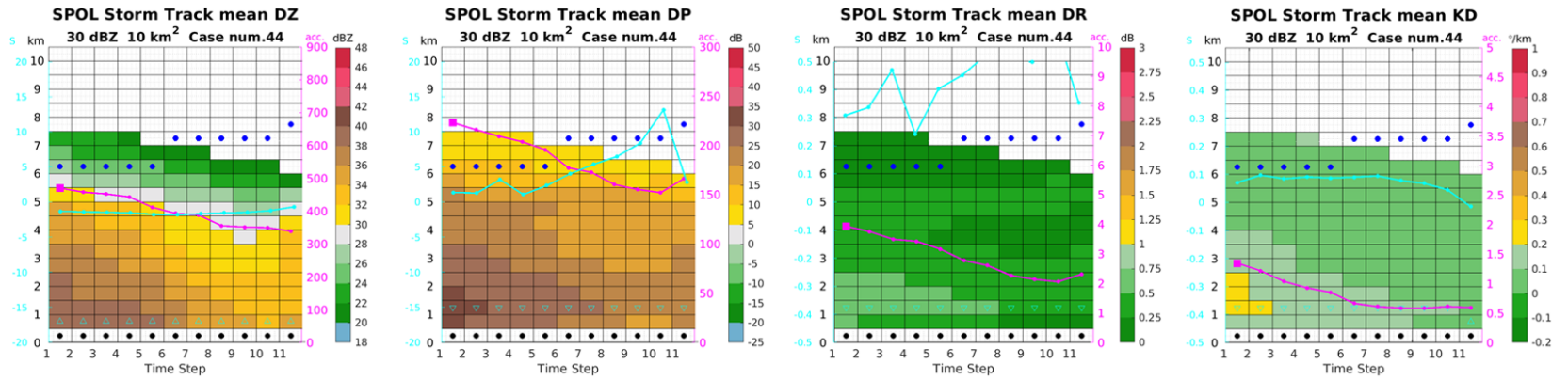
A.13
Case number 34



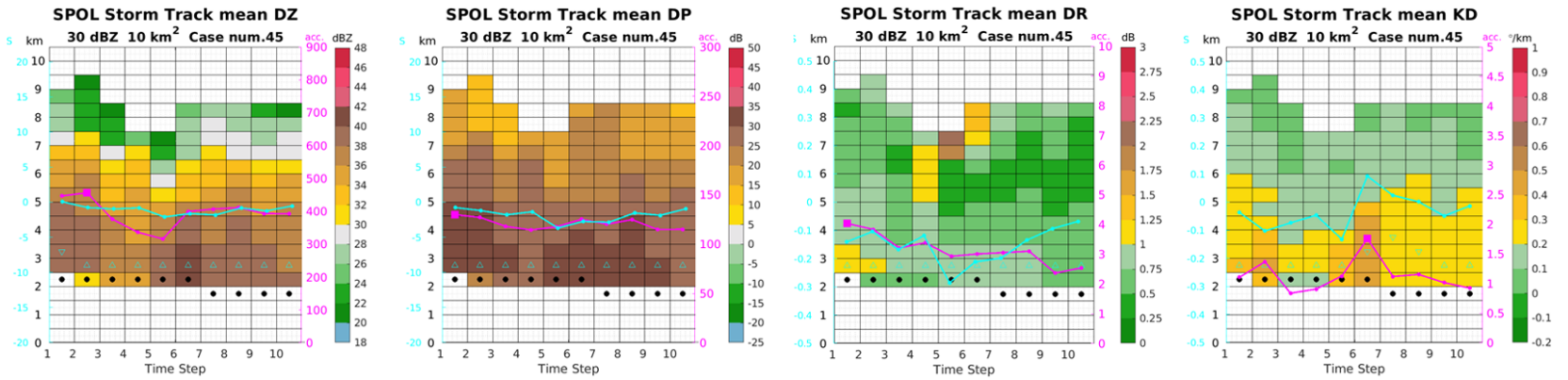
A.14
Case number 42



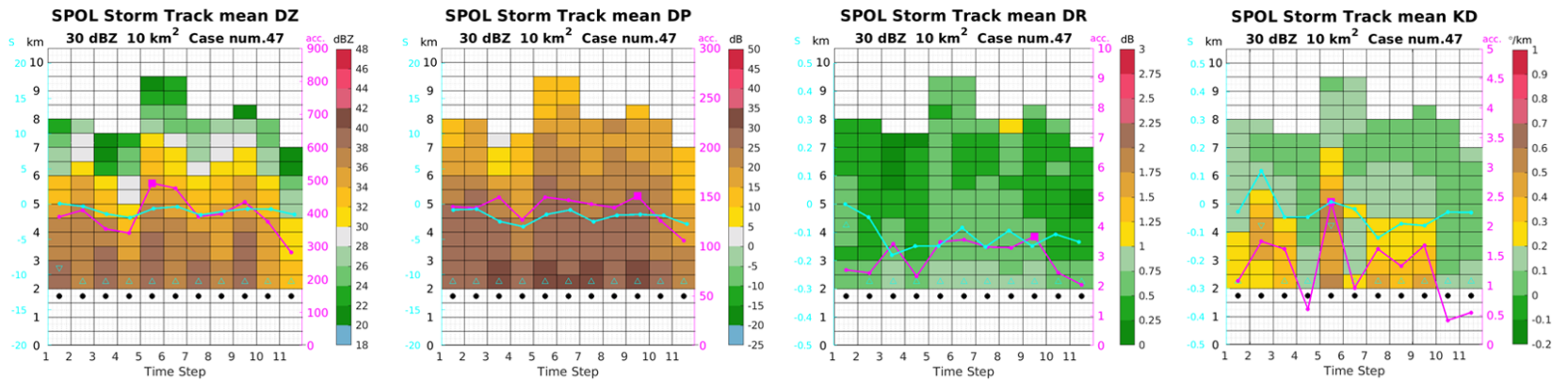
A.15
Case number 44



A.16
Case number 45

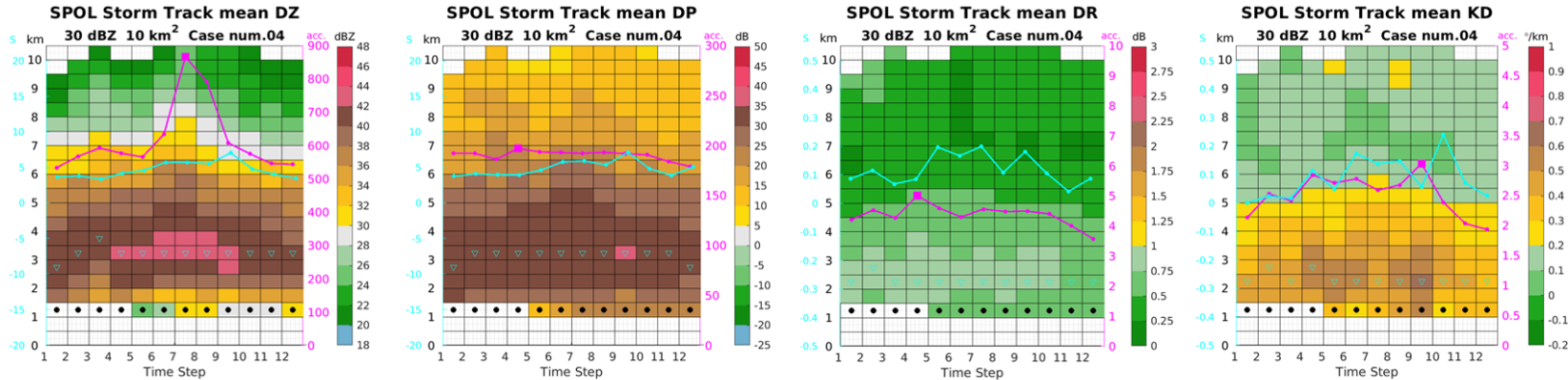


A.17
Case number 47

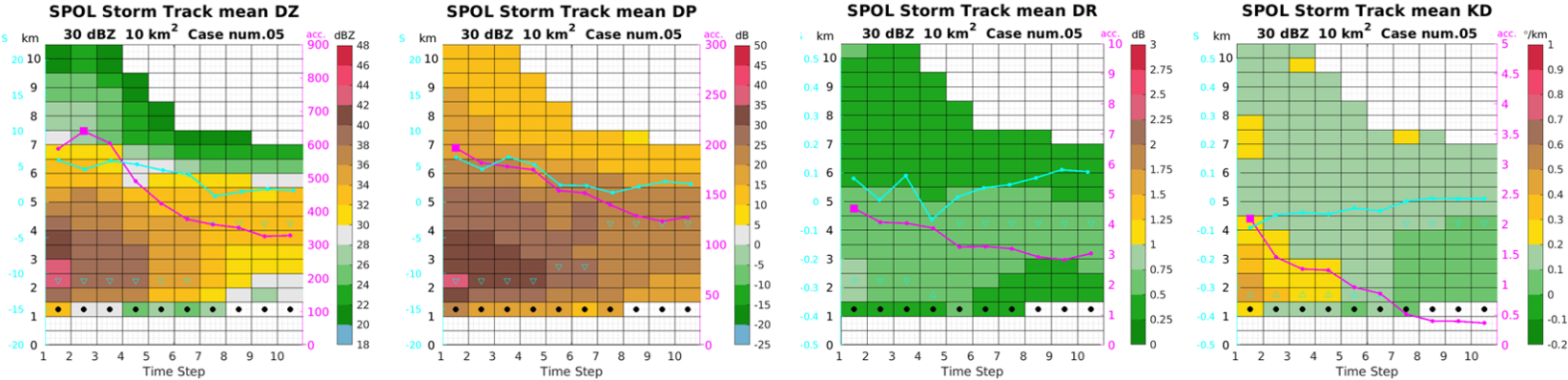


B. Time height series of mean dual-polarimetric parameters of 21 strong cases

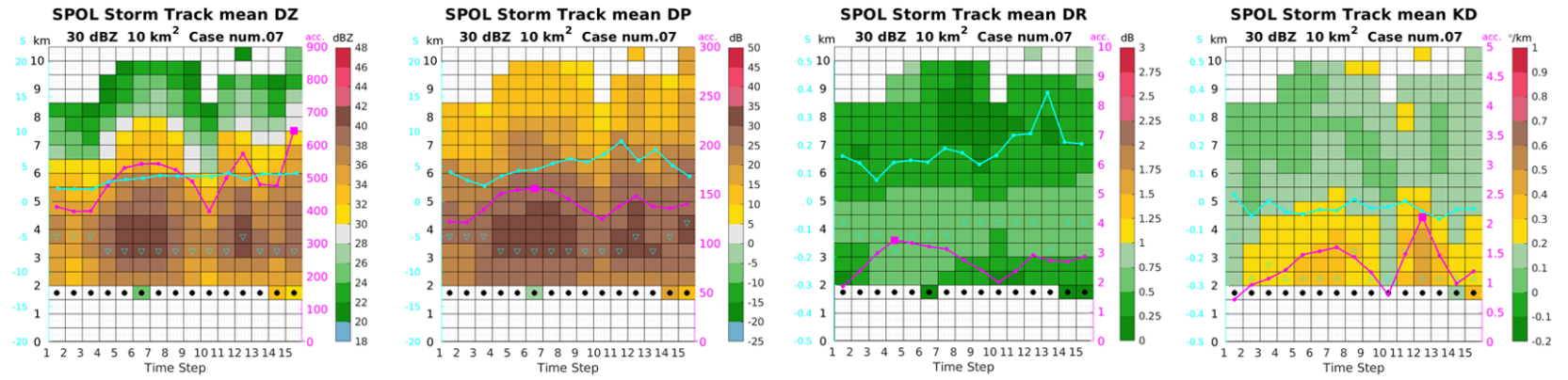
B.1
Case number 4



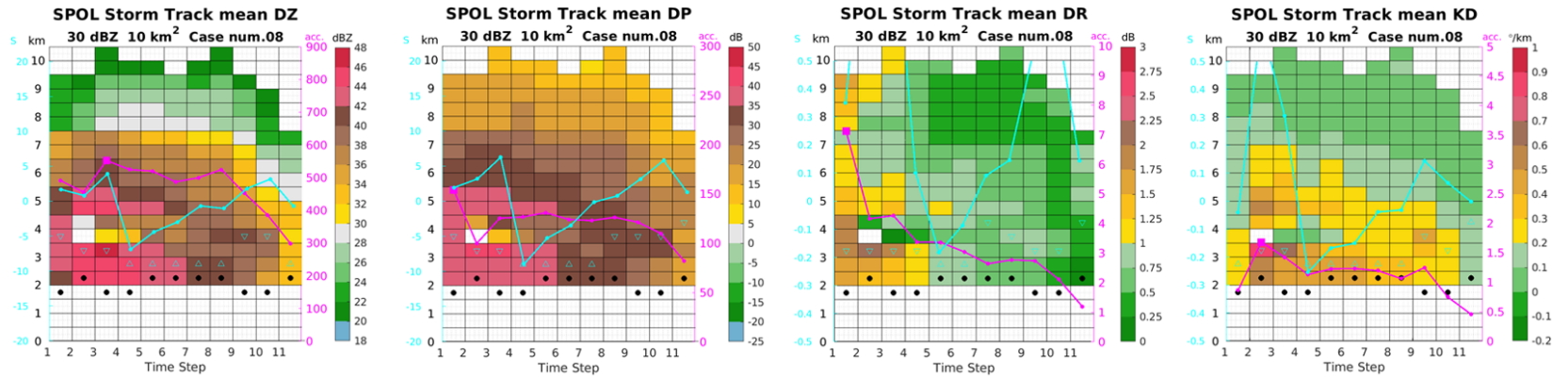
B.2
Case number 5



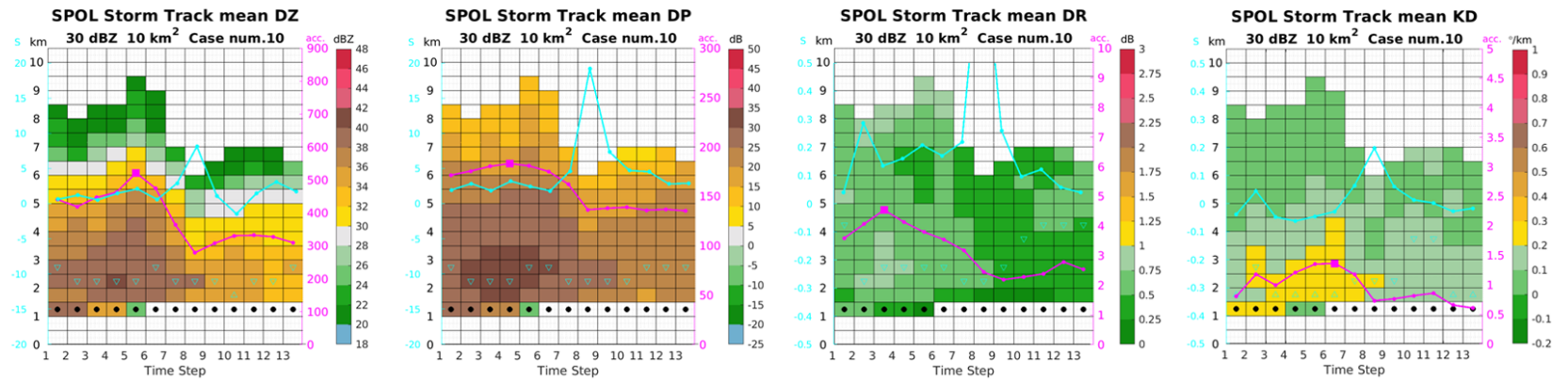
B.3
Case number 7



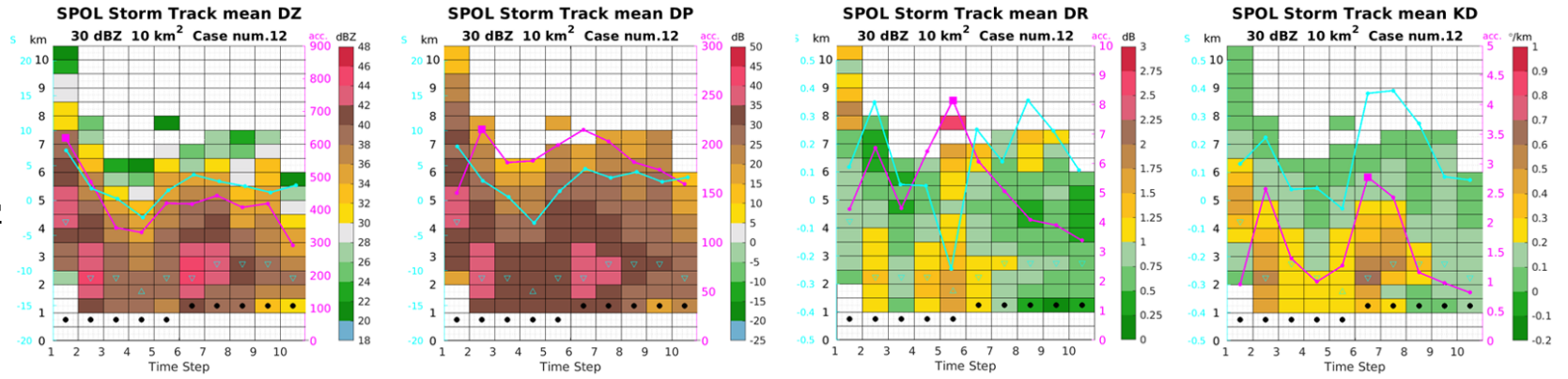
B.4
Case number 8



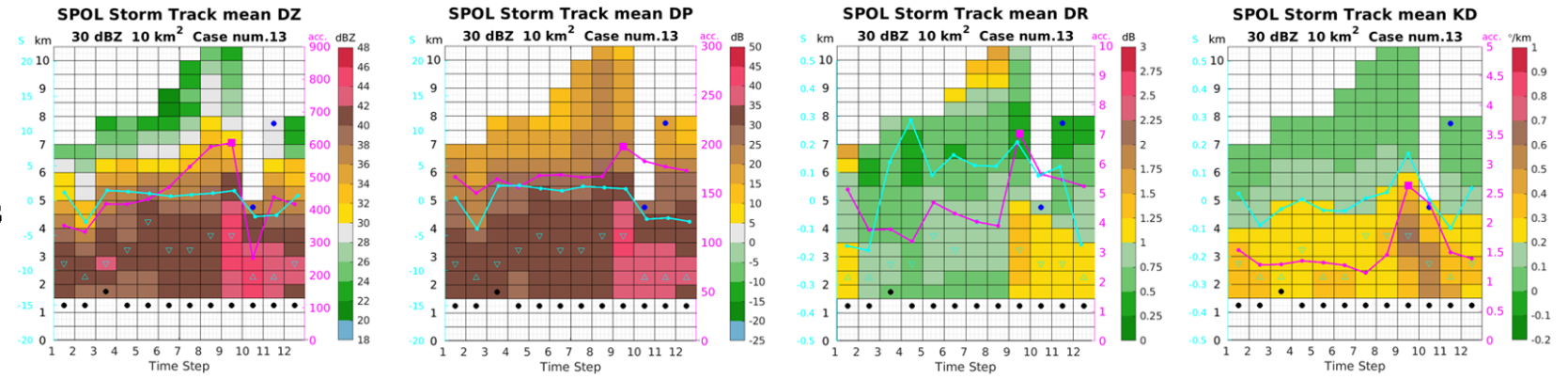
B.5
Case number 10



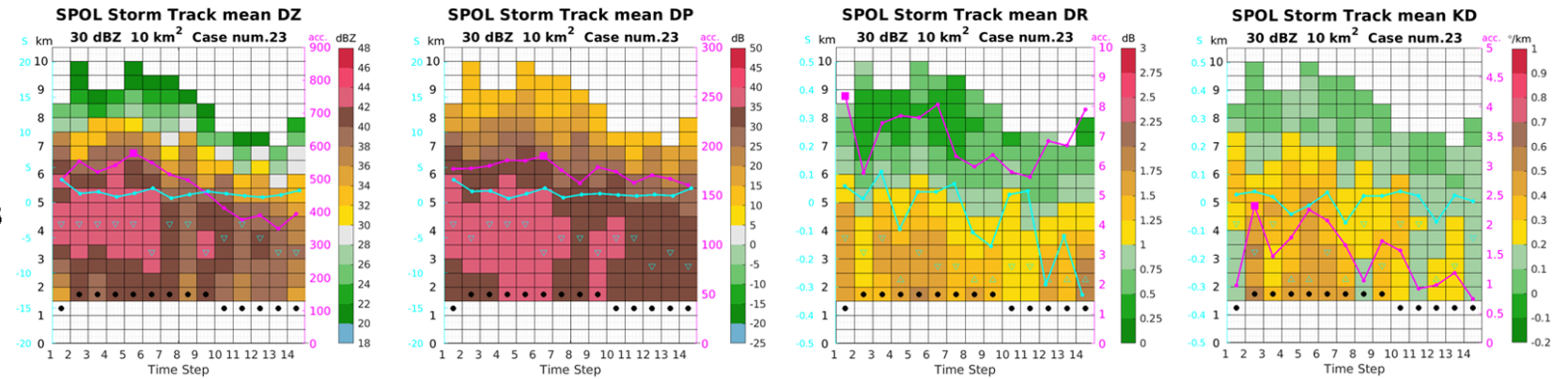
B.6
Case number 12



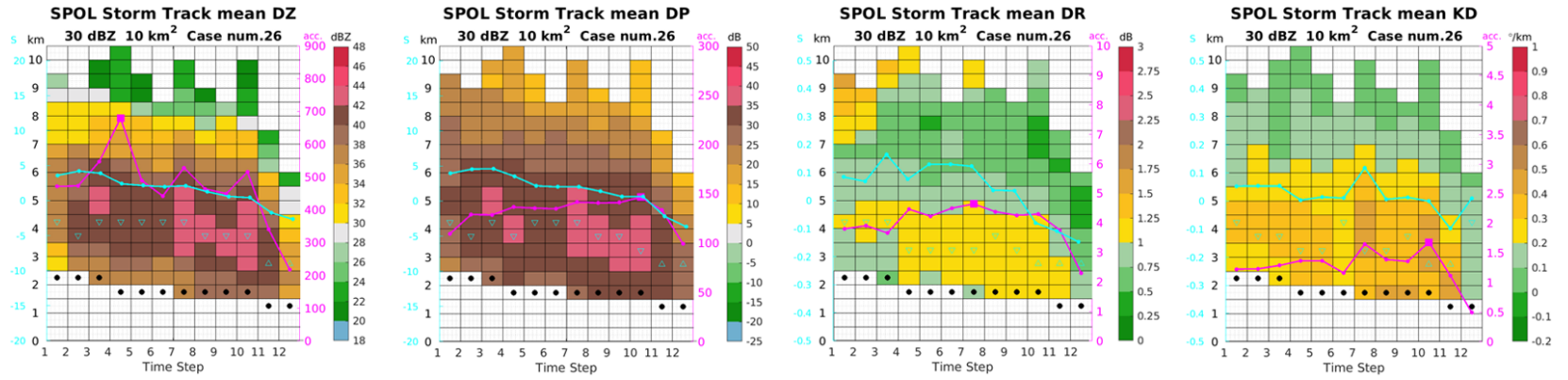
B.7
Case number 13



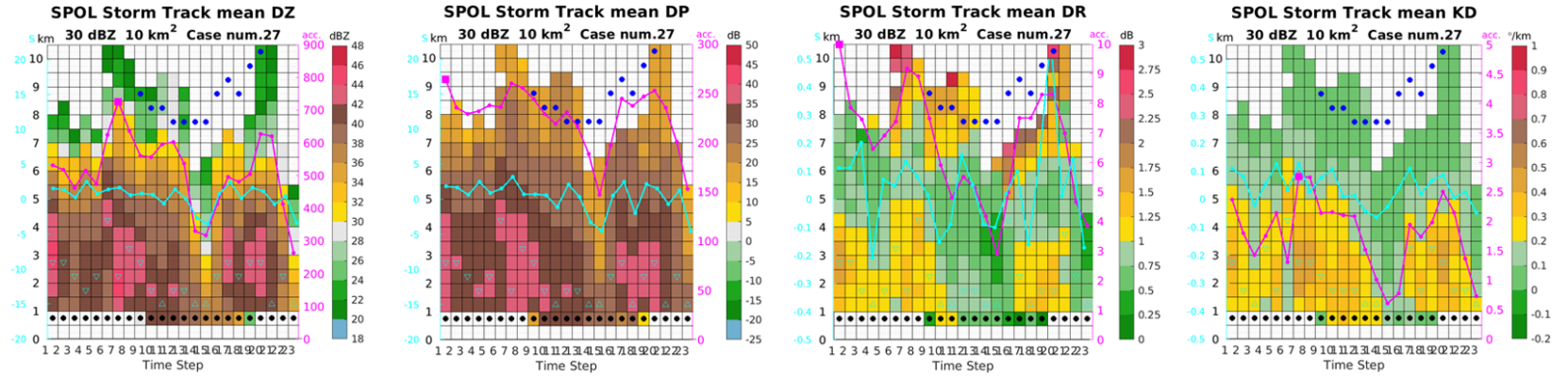
B.8
Case number 23



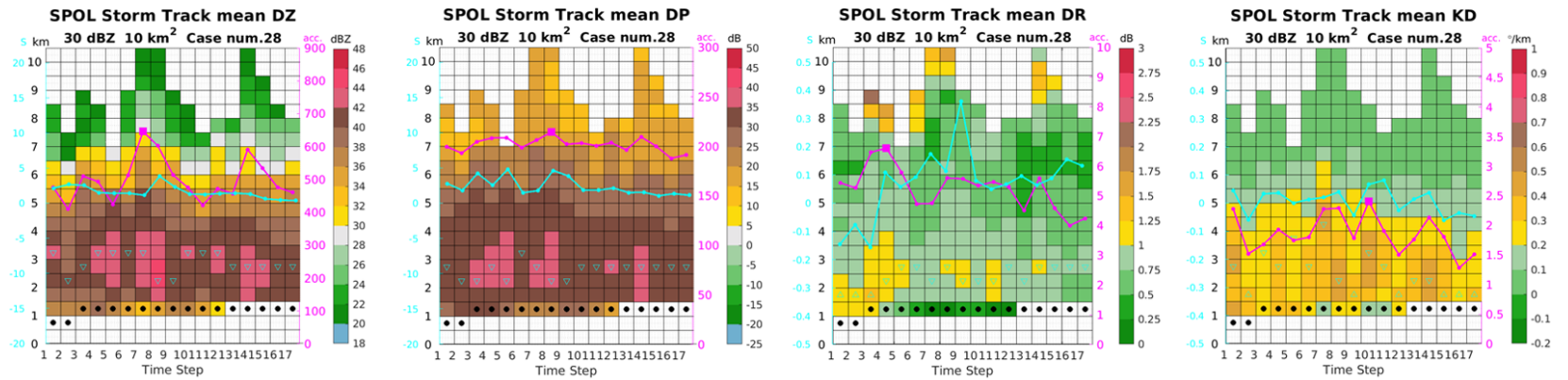
B.9
Case number 26



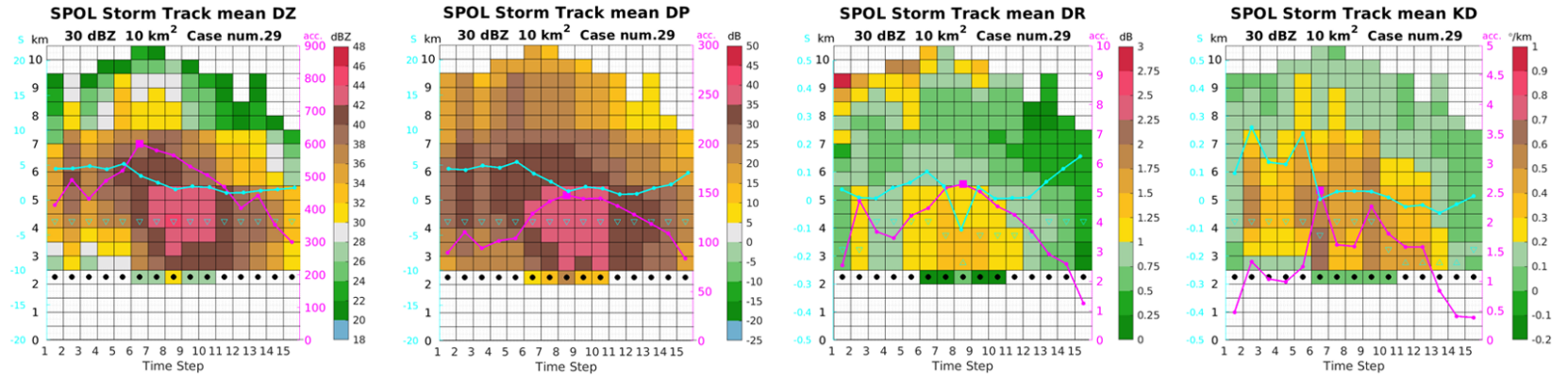
B.10
Case number 27



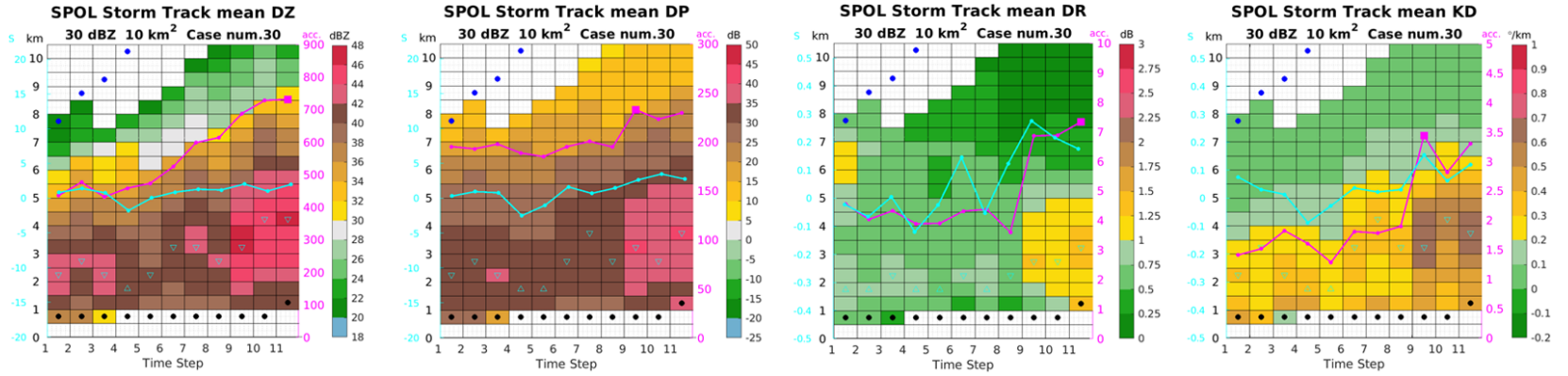
B.11
Case number 28



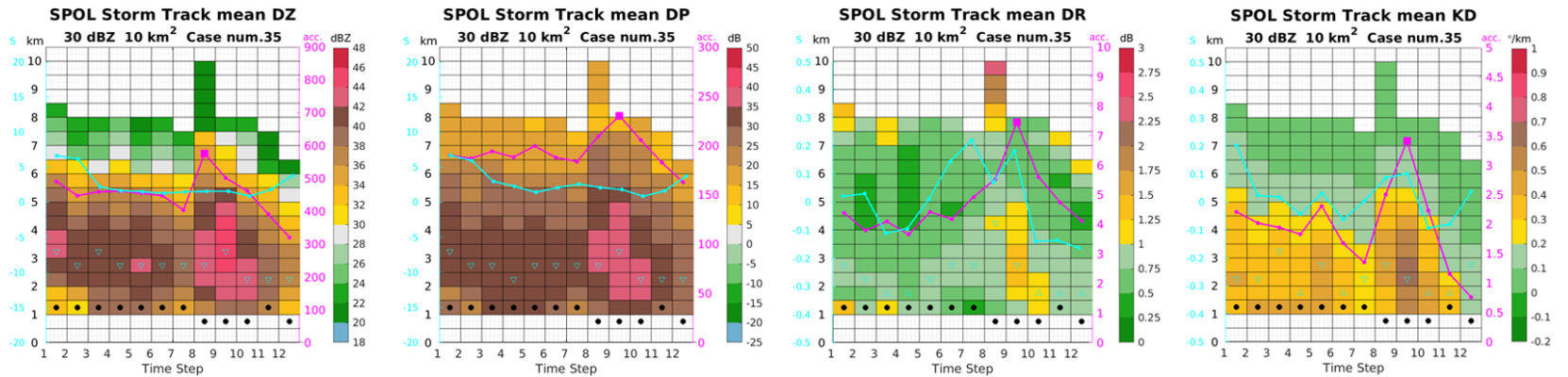
B.12
Case number 29



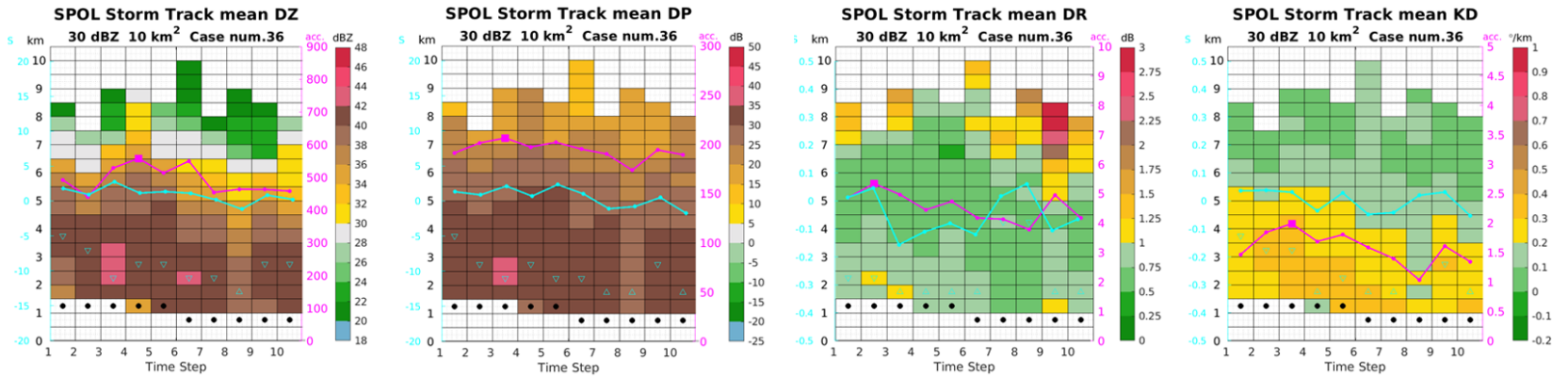
B.13
Case number 30



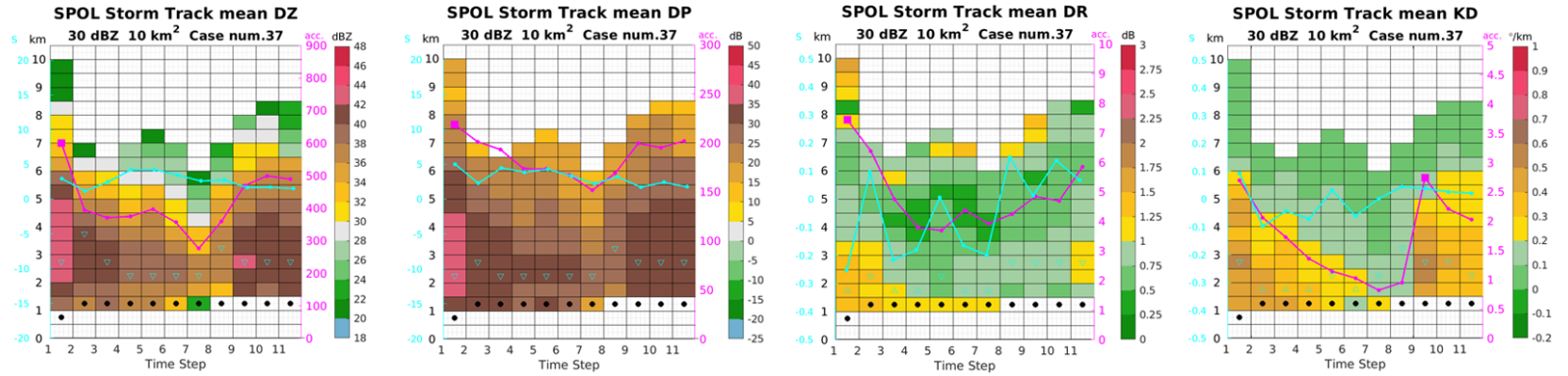
B.14
Case number 35



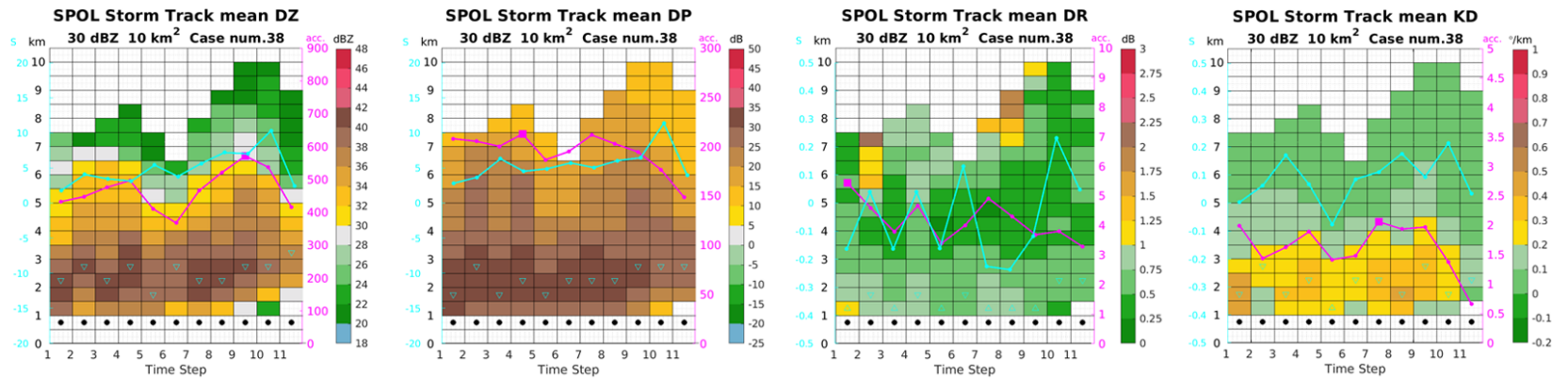
B.15
Case number 36



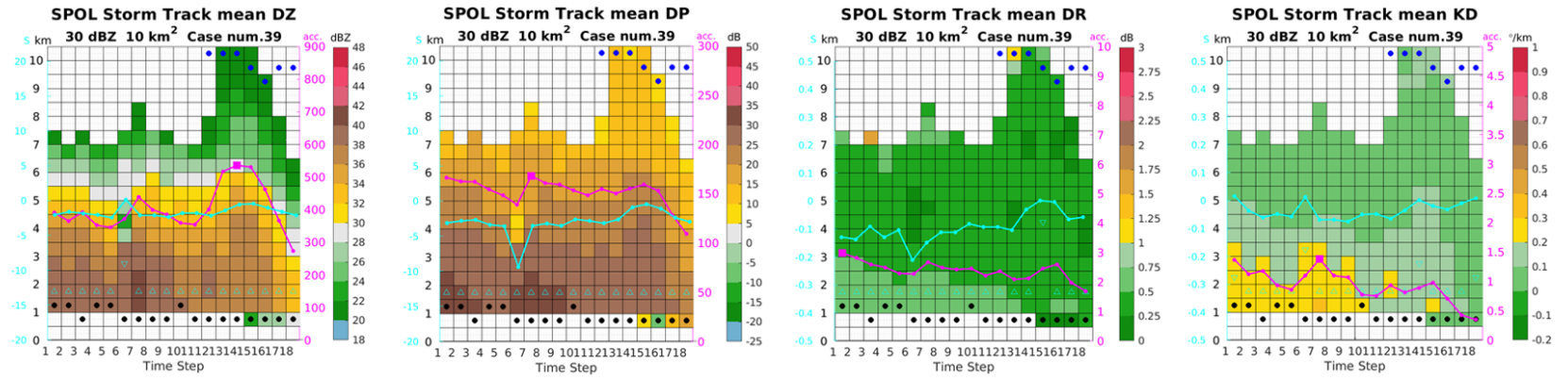
B.16
Case number 37



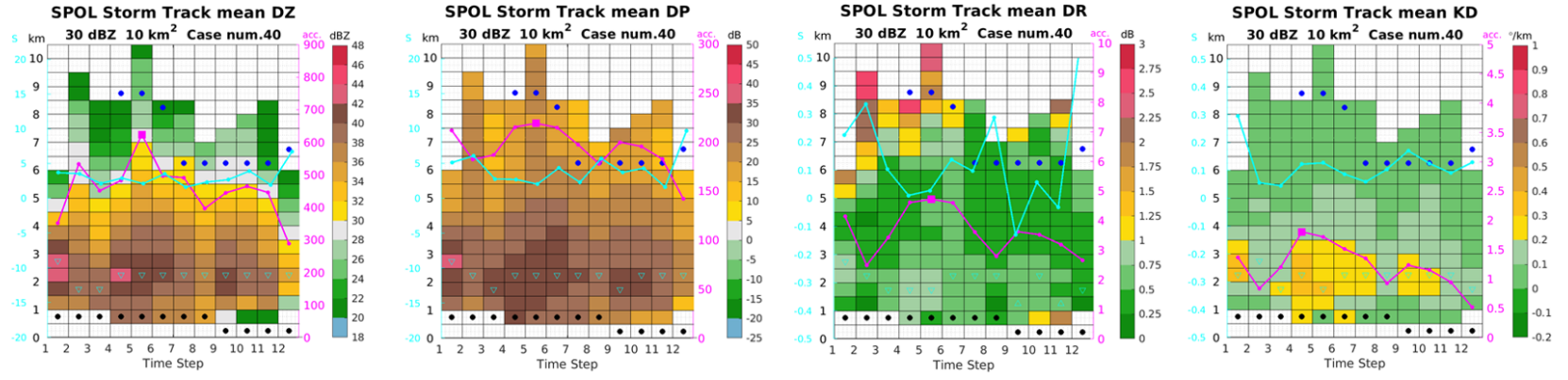
B.17
Case number 38



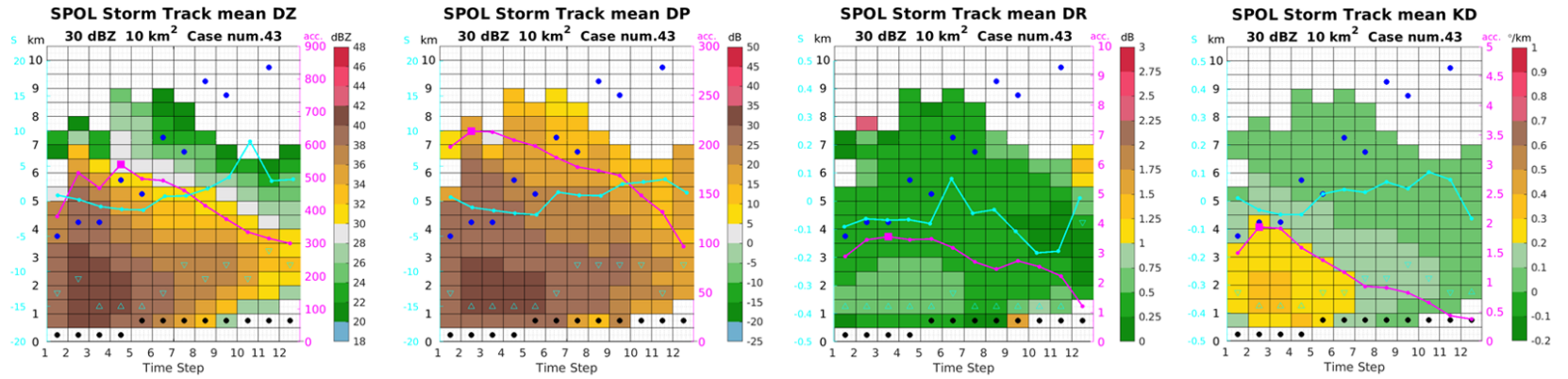
B.18
Case number 39



B.19
Case number 40



B.20
Case number 43



B.21
Case number 46

